

3480
736586
208215

TR 3480

COMPUTATIONAL MODELLING
OF
MASONRY CREEP AND SHRINKAGE

COMPUTATIONAL MODELLING OF MASONRY CREEP AND SHRINKAGE

PROEFSCHRIFT

ter verkrijging van de graad van doctor
aan de Technische Universiteit Delft,
op gezag van de Rector Magnificus Prof. ir. K.F. Wakker,
in het openbaar te verdedigen ten overstaan van een commissie,
door het College voor Promoties aangewezen,
op maandag 6 maart 2000 te 16:00 uur

door

Gideon Pieter Adriaan Greeff VAN ZIJL

Magister in die Ingenieurswese, Universiteit Stellenbosch, Suid-Afrika,
geboren te Port Elizabeth, Zuid-Afrika

Dit proefschrift is goedgekeurd door de promotoren:

Prof.dr.ir. R. de Borst

Prof.dr.ir. J.G. Rots

Samstelling promotiecommissie:

Rector Magnificus,	Voorzitter
Prof.dr.ir. R. de Borst,	Technische Universiteit Delft, promotor
Prof.dr.ir. J.G. Rots,	Technische Universiteit Delft, promotor
Prof.ir. D.R.W. Martens,	Technische Universiteit Eindhoven
Prof.Dr.-Ing. F.-J. Ulm,	Massachusetts Institute of Technology, Boston, USA
Prof.dr.ir. J.G.M. van Mier,	Technische Universiteit Delft
Dr.-Ing. P. Schubert,	Rheinisch-Westfälische Technische Hochschule, Aachen, Duitsland
Dr.ir. A. Vlot,	Technische Universiteit Delft

©1999 by G.P.A.G. van Zijl

All rights reserved. No part of the material protected by this copyright notice may be translated, reproduced or utilised in any form or by any means, electronic or mechanical, including photocopying, recording or by any information storage and retrieval system, without written consent of the copyright owner.

Printed in The Netherlands by Meinema BV, Delft

ISBN 90-9013475-1

Acknowledgments

Several individuals and institutes have contributed to enable the research reported in this thesis. An initial return on their investment is presented here in terms of acknowledgment and an expression of gratitude.

Prof. Jan Rots initiated the research project and subsequently provided guidance and inspiration. Prof. René de Borst, my supervisor for the greater part of this research period, is accredited with the healthy working environment in his group for Computational Mechanics.

In recognition of their invaluable influence, I thank my colleagues in the group for Computational Mechanics, in particular Harm Askes, Miguel Gutiérrez, Otto Heeres, Carla Roovers, Bert Sluijs, Akke Suiker, Harold Thung, Wang Weimin and Garth Wells.

Discussions and interaction with colleagues at other universities and institutions have broadened perspective and filled gaps. Rob van der Pluijm and Harold Brocken from TNO, Leo Pel and At Vermeltfoort of Eindhoven University of Technology, Paulo Lourenço of the University of Minho and Peter Feenstra of the Cornell University are acknowledged in this regard.

The research was performed while employed by the Faculty of Civil Engineering and later by the Faculty of Aerospace Engineering of the Delft University of Technology. It was supported by the Netherlands Technology Foundation (STW) under grant DCT 44.3406. The assistance by the Institute for Structural Engineering (ISI) of the Stellenbosch University, as well as by the Harry Crossley bursary fund during the initial stages is gratefully acknowledged. The models reported in this thesis have been implemented in a pilot version of the DIANA finite element code, which was subsequently employed for the analyses.

The birth of Natali and Berno in this research period has been inspirational. Thank you, Marietjie, for your loving support.

Contents

1	INTRODUCTION	1
1.1	Objectives and scope	1
1.2	Outline	2
2	FEATURES OF MASONRY BEHAVIOUR	5
2.1	Shrinkage	6
2.2	Moisture movement in porous, cementitious media	11
2.3	Creep	12
2.3.1	Introduction	12
2.3.2	Creep stress dependence	15
2.3.3	Creep dependence on moisture content and transport rate	16
2.4	Cracking	18
2.5	Thermal shrinkage and creep	23
3	MATHEMATICAL DESCRIPTION	25
3.1	Moisture migration	25
3.1.1	Initial and boundary conditions	27
3.1.2	Moisture migration in a two-phase medium	28
3.2	Mechanical behaviour	30
3.2.1	Creep	30
3.2.2	Drying and thermal shrinkage	34
3.2.3	Cracking	36
3.2.4	Crack mouth opening rate dependence	38
3.3	Discussion	39
4	NUMERICAL SOLUTION	41

4.1	Moisture migration	41
4.1.1	Weighted residual formulation	41
4.1.2	Finite Element formulation	42
4.1.3	Time integration	43
4.1.4	Incremental iterative solution procedure	43
4.2	Mechanical response	44
4.2.1	Weak formulation	44
4.2.2	Finite element solution	44
4.2.3	Integration of the visco-elasticity constitutive equation	45
4.2.4	Integration of the plasticity constitutive equation	47
4.2.5	Incremental-iterative solution procedure	50
4.2.6	Adaptive time-stepping	51
4.3	Finite element interpolation order	53
5	CRACK MODELLING STRATEGIES	55
5.1	Discrete modelling	55
5.1.1	An interface model for 2-D masonry discrete modelling	56
5.1.2	Verification and validation of discrete approach	62
5.1.3	Extension to plane interface behaviour for 3-D discrete analysis	66
5.2	Continuum modelling	69
5.2.1	An anisotropic Rankine-Hill model	69
5.2.2	The regularisation of the localisation problem	73
6	VALIDATION OF THE MECHANICAL MODEL: FAILURE UNDER SUS- TAINED LOAD	77
6.1	Description of three-point bending tests	78
6.2	Characterisation of the model parameters	79
6.3	The failure envelope by displacement control	80
6.4	Sustained load response	81
6.5	The failure envelope for long term, rate-independent response	82
6.6	Discussion	85
7	VALIDATION OF THE TOTAL MODEL: MASONRY TRANSIENT CREEP	89
7.1	Modelling approach	89

7.1.1	Characterisation of the model parameters	91
7.1.2	Spatial and time discretisation	95
7.1.3	Boundary conditions and initial values	96
7.2	Shrinkage and transient creep response	97
7.2.1	Large block (CS-block) specimen response	97
7.2.2	Small brick (CS-brick) specimen response	100
7.3	Mesh objectivity	106
7.4	Sensitivity study	107
7.4.1	Moisture content dependence on surface convection coefficient . .	107
7.4.2	Shrinkage coefficient dependence on humidity	108
7.4.3	Pickett effect	109
7.4.4	Creep/relaxation	110
7.5	Discussion	112
8	MASONRY WALLS UNDER RESTRAINED SHRINKAGE	115
8.1	Modelling approach	116
8.1.1	Moisture migration analysis	117
8.1.2	Mechanical analysis	118
8.2	Base-restrained shrinkage response	119
8.3	Regularisation through the cracking rate dependence	122
9	TOWARDS RATIONAL DESIGN RULES	127
9.1	Current status of movement joint spacing design	127
9.2	Modelling approach	129
9.2.1	Characterisation of the equivalent vertical crack	130
9.2.2	Typical Dutch masonry characterisation	132
9.3	Verification of modelling approach	134
9.3.1	Reference response: discrete analyses of base-restrained walls . .	134
9.3.2	Equivalent modelling response	140
9.3.3	Deficiencies of simple modelling strategy	146
9.4	Design rules	148
9.5	Discussion	149

10 SUMMARY AND CONCLUSIONS	155
REFERENCES	159
SUMMARY	167
SAMENVATTING	169
CURRICULUM VITAE	171

Chapter 1

INTRODUCTION

1.1 Objectives and scope

The main objective of this study is to bridge the gap between the fundamental scientific knowledge of physical processes and mathematical descriptions thereof on one hand and their application in practical design on the other hand. This means in the first place that, for practical relevance, the processes are viewed at the macroscopic level. Secondly, the emphasis lies on the casting of existing formulations for individual phenomena into an integrated, robust formulation, which enables the viable analysis of the synergism of the interacting phenomena.

The above endeavor is focused on unreinforced masonry. Because the level of characterisation of this material lags behind concrete, borrowing from the concrete world is inevitable. It is justified by the shared cementitious nature, which governs the behaviour of both materials and causes similarities between them. An intended by-product is the broadening of the research front of masonry, by delivering a numerical model which anticipates experimental observations. In this manner the characterisation process may be accelerated.

The processes of particular interest for this study are those of shrinkage and creep. The interest in these phenomena arises from the damage they inflict on structures. To assess such damage, an ability to capture crack initiation and growth is required. The product of this work is a numerical model, which has the ability to simulate and predict the interaction of shrinkage, creep and cracking in masonry structures of practical relevance and scale.

It is imperative that the developed model is thoroughly verified and validated. Where experimental data on masonry are lacking, it is defensible to revert to concrete experiments.

1.2 Outline

If one embarks on the modelling of a process, it is instructive to study the prominent features that are to be captured, in order to distinguish trends and dependencies. In Chapter 2 the main features and mechanisms of shrinkage, creep and cracking of cementitious materials are described at the hand of experimental observations over the past century. Where data are not available for masonry, they are borrowed from the concrete literature.

Chapter 3 proceeds with the mathematical modelling of the phenomena described in Chapter 2. The hygral response is formulated as a nonlinear diffusive process. The mechanical response, i.e. the stress-deformational response, is elaborated from the static equilibrium, the kinematics of deformation and a constitutive relation. Mathematical descriptions of the shrinkage, creep and cracking enter the constitutive relation, which is in a rate form due to the nonlinearity of these phenomena. For the analysis of practical problems a numerical solution of the mathematical formulation is necessary. The finite element solution of the governing set of differential equations is elaborated in Chapter 4.

Chapter 5 presents two alternative strategies to model cracking in masonry. As the joints are the weak link in masonry, a discrete description of the cracks is particularly useful, because their position and orientation are predictable. An interface material model is formulated, which captures the debonding and shearing along the masonry joints. A continuous description of the cracks, an elegant alternative to the discrete approach when the structural size is large relative to the brick size, is also formulated.

The model is verified and validated in a modular way. In Chapter 6 the mechanical part is activated to analyse the interaction between creep and cracking, as exhibited by concrete beams tested in three-point bending. Subsequently, the hygral part of the model is also activated in the verifying analyses of masonry drying and creep experiments, Chapter 7. Special attention is given to the distinction between the basic creep and the drying creep, or Pickett effect.

Moving away from the verification and validation analyses on small to medium size laboratory specimens, large masonry walls are analysed in Chapter 8. These analyses serve to demonstrate the robustness of the model in capturing crack initiation and growth into a fully developed crack pattern, as well as the objectivity in terms of crack spacing and orientation.

In Chapter 9 a step is made towards deriving practical design rules from numerical results. A particularly lean design aspect, namely the spacing of movement joints in masonry walls, which controls cracking due to differential thermal and hygral movement, is taken as an illustrative example. A simplified modelling strategy is described and verified numerically with reference analyses, to make the repetitive analysis of such large masonry walls viable.

Finally, in Chapter 10, some concluding and reflecting remarks are made.

Chapter 2

FEATURES OF MASONRY BEHAVIOUR

The behaviour of cementitious materials is complex and is subjected to various influencing factors. To a large extent the complicated microstructure, which is continuously modified by ongoing chemical and physical processes, causes the complexity. The microstructural modification is brought about by the formation of hydration products, by thermal variation, as well as by the forced migration of moisture through the micropores and the ensuing breakage of bonds at this level. However, for the viable analysis and prediction of the global behaviour of such materials, a macroscopical approach is required. Then, they are considered as homogeneous continua, which obey laws obtained by the combination of volume-averaging of the microscopical processes and the attribution of the most prominent features of the global behaviour. In this chapter these features are briefly presented, to set the scene for the formulation of a numerical model in the subsequent chapters. No attempt is made to present a textbook on the physics and chemistry of the processes at hand. A summary of the state-of-the-art knowledge was made by Young (1988) and Neville (1991), while many research results are scattered across scientific journals, proceedings of conferences, for example Wittman (1982), Bažant and Carol (1993) and chapters in books, for example Domone (1994).

The features of concrete behaviour have been studied systematically since the beginning of the 20th century and a vast pool of experimental data has been gathered and trends have been established. Despite the efforts of the pioneers up to the contemporary researchers of masonry, the level of characterisation lags behind concrete. However, the shared cementitious nature governs the behaviour of both materials and causes similarities. In this chapter this is exploited by reverting to concrete data where masonry experimental data are inadequate or absent. This is done in the belief that the broadening of the research front, by adding a provisional numerical tool to the pool of methods of studying masonry, will accelerate the convergence to the understanding of and the ability to predict masonry response.

The major contributors to time-dependent deformation are hygral and thermal shrinkage and creep. Therefore, the trends and dependencies of these phenomena are outlined at the hand of experimental evidence. This study focuses on hygral shrinkage and creep. The evolution of the moisture content in the material to achieve equilibrium with the environment it is exposed to, is discussed, deemed necessary by the overwhelming proof that it drives the shrinkage and creep. Cracks contribute to the complexity of the time-dependent behaviour. They exist even when the material is not mechanically loaded, due to hygral and thermal gradients. An overview is given of the observed trends in the cracking of masonry. Finally, the coupling between the hygral and thermal processes and the mechanical behaviour is discussed.

2.1 Shrinkage

Shrinkage is the stress-less volume reduction of matter. The major contributors to this volume change in cementitious material are the *drying shrinkage*, which is the shrinkage/swelling due to the variable humidity and the *thermal shrinkage*, which denotes the shrinkage/swelling due to temperature changes. Other sources of shrinkage are the *autogeneous shrinkage*, which is the volume change caused by the hydration process, and the *carbonation shrinkage*, which is the result of the reaction of calcium hydroxide in the cement paste with atmospheric carbon dioxide.

There is evidence that the autogeneous shrinkage increases in significance with decreasing water/cement (w/c) ratio in concrete (Le Roy and De Larrard 1993). For the extremely dry pastes currently obtainable in search of high strength concrete, an autogeneous volume reduction of 4 mm/m has been reported for the paste and 0.7 mm/m for concrete containing such paste, Tazawa and Miyazawa (1993). These values are of the same order as the drying shrinkage. For normal concretes, however, the autogeneous shrinkage is usually negligible (Bažant 1988, Tazawa and Miyazawa 1993). This source of shrinkage is also active in masonry with cement-based mortar joints, as well as in masonry containing concrete units, but is equally, or more insignificant.

Likewise, the carbonation shrinkage can reach levels of 3 to 4 mm/m in cement pasts (Houst 1993). However, the overall contribution to the shrinkage is usually negligible in concrete, due to the small penetration depth (a few millimeters) of the carbonation process in well-compacted, average to high quality concrete (Bažant 1988, Domone 1994). However, the carbonation may penetrate to a significant depth in poor concrete, or in poorly compacted regions, in which case the carbonation shrinkage may be of the same order as the drying shrinkage (Domone 1994). With regard to its importance in masonry, the above

arguments apply for concrete bricks and cement-based mortars, but this type of shrinkage has also been identified in calcium silicate units (Schubert 1982). Nevertheless, in this study the drying and thermal shrinkage are considered to dominate the total shrinkage in masonry and the autogeneous and carbonation contributions are neglected.

The *free drying shrinkage*, which is defined as the true, stress-free drying shrinkage, can not be measured directly, because the distribution of moisture content is never uniform, which causes differential strains and associated stresses (Picket 1946, Wittmann 1980, Bažant 1988, Alvaredo 1994). The nonuniformity is caused by the slow nature of the drying process in cementitious materials like concrete and masonry, where the material close to an exposed surface dries quicker than the central part, Figure 2.1a. If the material had consisted of a stack of non-interconnected layers, the different layers would have different lengths upon shrinkage, as shown by the dotted lines in Figure 2.1b. However, due to the connection the free deformation is inhibited to take the form indicated by the solid line, 2.1b. The left layers are extended, which causes tensile stress in them, while the right layers shorten, generating compressive stress. These internal stresses, or *eigenstresses*, are shown in Figure 2.1c.

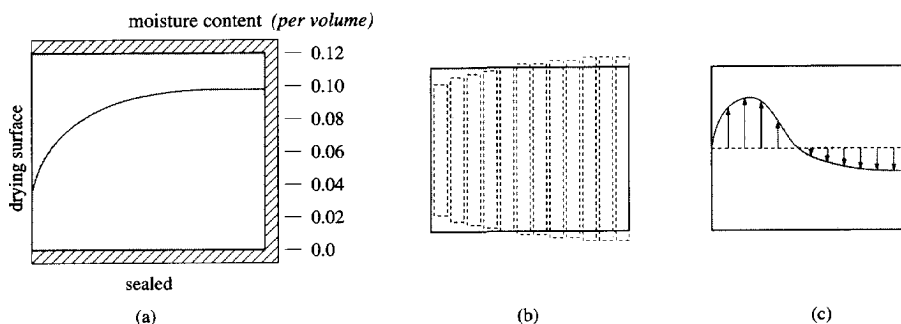


Figure 2.1: Illustration of (a) nonuniform drying, (b) shrinkage and (c) *eigenstressing* due to the slow drying of cementitious materials.

One way of finding the true drying shrinkage is to measure the shrinkage of very thin specimens, in which no, or an insignificant hygral gradient exists. Alternatively, it must be determined indirectly, by assuming a model of the interacting phenomena and iteratively modifying the model parameters until acceptable agreement is found with the measured response of drying specimens.

Finding a simple relation between the drying shrinkage and the moisture loss is complicated by the various mechanisms that drive the moisture flow. Figure 2.2a indicates a bilinear relation, with a distinct change of slope at a relative humidity (RH) of about 10%,

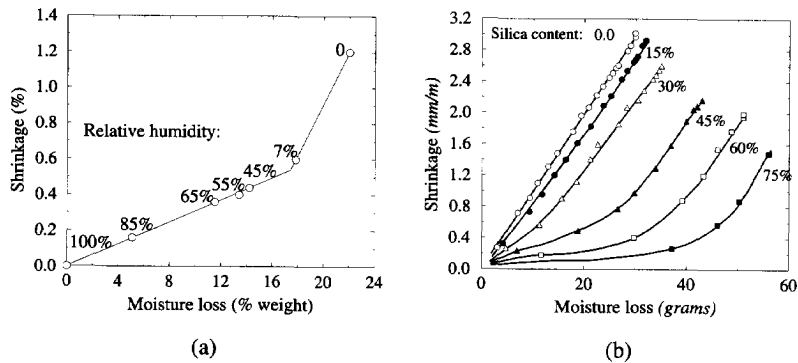


Figure 2.2: The relation between moisture loss and drying shrinkage in (a) a typical hardened cement paste (Verbeck and Helmuth 1968) and (b) cement pastes containing different proportions of pulverised silica (Powers 1959).

which suggests that a different mechanism becomes active at this point. Powers (1959) prepared cement pastes containing different proportions of *capillary voids*, which are the larger pores in cementitious materials, by adding pulverised silica to the mixture. The larger water/cement ratio requirement of such mixtures causes a larger amount of capillary pores. He concluded from his study of the drying shrinkage of these cement pastes that the loss of free water from the capillary voids causes little or no shrinkage, Figure 2.2b. Only once they are emptied, significant shrinkage occurs upon further drying.

However, the enormous research effort over the last four decades has revealed more mechanisms, Table 2.1, which makes the prediction of shrinkage upon drying even more difficult than indicated by Figure 2.2. For detailed discussions of these mechanisms the reader is referred to Young (1988), or Domone (1994).

Further complexities in the moisture movement-shrinkage relation is revealed upon cyclic

	Relative humidity:					
	0	0.2	0.4	0.6	0.8	1.0
Powers (1965)	Disjoining pressure					
Ishai (1965)	Surface energy			Capillary tension		
Feldman and Serada (1970)	Interlayer water			Capillary tension and surface energy		
Wittmann (1968)	Surface energy			Disjoining pressure		

Table 2.1: Proposed mechanisms of shrinkage (Soroka 1979).

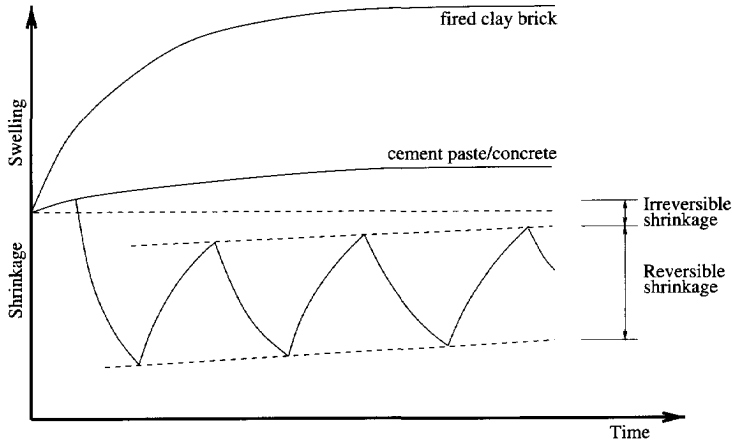


Figure 2.3: Illustration of typical swelling and shrinkage in concrete or masonry constituent materials (L'Hermite et al. 1949).

drying and re-wetting, Figure 2.3 (L'Hermite et al. 1949). A part of the shrinkage is irreversible, nearly all of which establishes during the first drying-rewetting cycle (L'Hermite et al. 1949, Parrot and Young 1982, Sabri and Illston 1982). This suggests that, in addition to the various shrinkage mechanisms which cause *reversible* shrinkage (Table 2.1), chemical reactions change the microstructure. The large initial irreversible shrinkage is probably caused by the formation of new links in the cement gel when the particles are in closer contact upon shrinkage (Neville 1991). The gradual reduction of the irreversible shrinkage upon subsequent drying/wetting cycles, is largely explained by the continuing hydration of the cement paste, by which process the proportion of the fine pores decreases and the shrinkage level at a particular moisture content decreases along with it.

Although the attempts to mathematically model the processes in the microstructure lead to better understanding of the mechanisms of shrinkage, the complex nature of the microstructure and the still limited knowledge of the microstructural processes remain stumbling blocks. Furthermore, a viable practical analysis of shrinkage requires a macroscopical approach. This has led analysts to establish simple relations between the drying shrinkage and moisture loss, or, for mathematical convenience, relations between the shrinkage and the relative humidity (Wittmann 1977, Bažant 1988, Alvaredo et al. 1995). Figure 2.4 shows the shrinkage of several thin samples of hardened cement paste which were allowed to reach hygral equilibrium with an environmental climate of different, constant humidities and a constant temperature. The significant irreversible shrinkage proportion is evident from Figure 2.4a, which calls for a different shrinkage-humidity relation

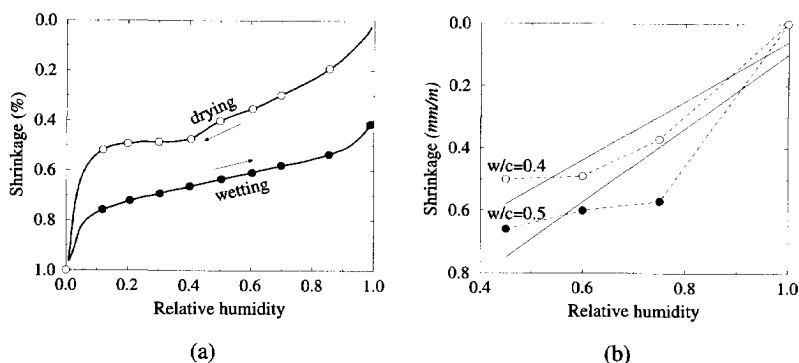


Figure 2.4: The relation between relative humidity and drying shrinkage obtained from (a) a single drying-wetting cycle (Sabri and Illston 1982) and (b) end values of shrinkage from saturation ($RH = 1.0$) to various, constant environmental humidities (Alvaredo et al. 1995).

for the drying than for the (re)wetting. To model the subsequent cycles requires different sets of relations, because of their hysteretic, ratchetting nature. Figure 2.4b shows the simple linear approximation by Alvaredo et al. (1995) in the range $0.4 < RH < 1.0$. The applicability of such an approach is clearly limited to a single drying or wetting cycle in this humidity range.

The above choice of the relative humidity for the characterisation of the shrinkage avoids the need to account for the significant loss of free water caused by the continuing hydration, because the self-desiccation humidity drop is negligible (Bažant 1988).

With regard to masonry, it must be noted that, for drying shrinkage to occur, there must be moisture in the material in the first place. In concrete moisture is naturally present initially due to the fabrication process. Also in concrete bricks/blocks some moisture is retained, while moisture is introduced into calcium silicate unit masonry by the standard practice of pre-wetting the units to a moisture content as high as 9% by weight to achieve better bond with the mortar. On the other hand, the firing process leaves fired clay bricks dry. After these bricks have been laid, they absorb moisture from the environment, which causes the swelling observed in the bricks and the masonry of which it is a constituent by, for example, Drysdale et al. (1994) and Van der Pluijm and Wubs (1996) and is provided for in design codes (CEN 1995). This process is accompanied by complex chemical reactions in the fired clay, which renders the swelling irreversible (Drysdale et al. 1994), unlike the swelling observed in concrete upon submergence in water, Figure 2.3. Yet, the swelling of the units can be offset by the mortar shrinkage to result in an overall volume decrease

of the masonry composite (Van der Pluijm and Wubs 1996, Forth and Brooks 1997).

A further aspect particular to masonry is the anisotropy of the shrinkage. This is not only caused by the different geometrical arrangements of the units and joints in the orthogonal directions, because a 25% difference between the vertical and horizontal shrinkage of free units of calcium silicate has been observed (Van der Pluijm and Wubs 1996).

2.2 Moisture movement in porous, cementitious media

The movement of moisture in porous, cementitious media is complex, driven by various mechanisms. By accepting a phenomenological approach it is possible to avoid the solution of these transport phenomena at the micro level in a porous medium, i.e. at the pore level. The formulation of such an approach is facilitated by knowledge of the moisture movement in specimens. By measuring techniques varying from dielectric probes (L'Hermite and Mamillan 1973) to the contemporary high resolution nuclear magnetic resonance (NMR) method (Pel 1995) it is possible to measure moisture profiles within the material, Figure 2.5. In this way the high absorption/drying rate near the surface in

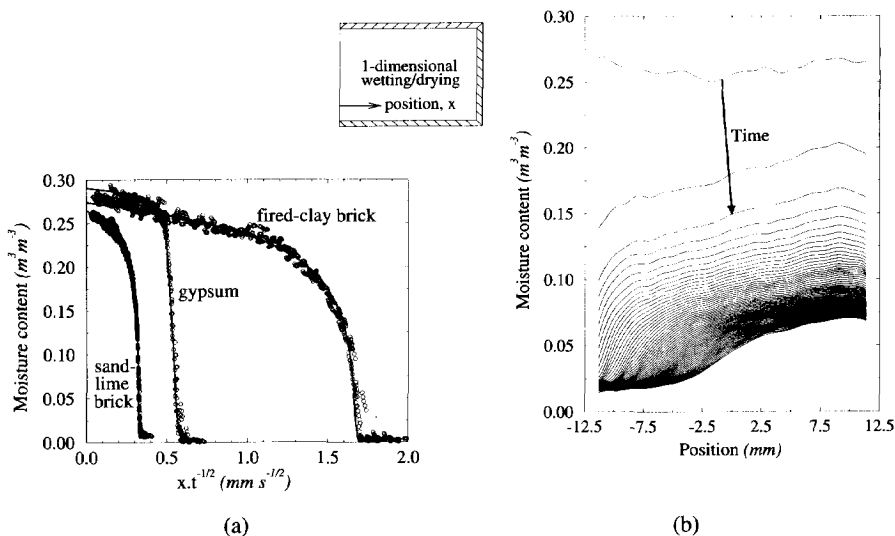


Figure 2.5: Distribution of moisture in cementitious materials upon (a) wetting and (b) drying (Pel 1995).

relation to inner core is revealed. In a macroscopical sense this can be seen as a diffusive process, the validity of which has been verified by the *Boltzmann transformation* of the wetting profiles, Figure 2.5a, i.e. the division of the position with the square root of time. It remains to define a global diffusivity, which, in a diffusion formulation, accounts for all the different microscopical flow processes in an average sense.

For the estimation of the shrinkage evolution by the simple approach discussed in the previous section, the moisture content in a material point must be translated to the relative humidity via the *sorption isotherm*, Figure 2.6.

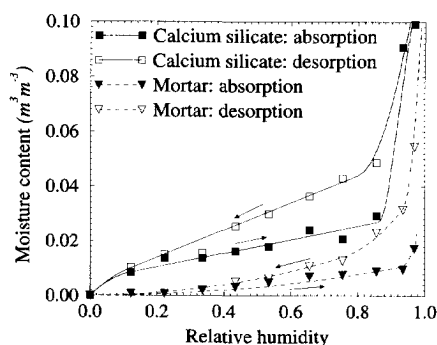


Figure 2.6: Isothermal sorption curves (Pel 1995) for masonry constituents.

Neither the water transport, nor the heat flow in cementitious materials is influenced by the mechanical straining of the material (L'Hermite and Mamillan 1968, Bažant 1988, Bažant and Kaplan 1996). In Figure 2.7 it can be seen that the difference between the responses of loaded and unloaded specimens, which were subjected to the same environmental conditions, is negligible. Only if large cracks open, the permeability is increased significantly (Bažant et al. 1987). Therefore, in the absence of large cracks, the moisture migration process is essentially decoupled from the mechanical stresses and strains, which allows the separate characterisation and solution of the two phenomena.

2.3 Creep

2.3.1 INTRODUCTION

Like concrete, masonry continues to deform, or *creeps* if it is subjected to a constant load. Figure 2.8a. Conversely, if a particular deformation is sustained, the force required for the

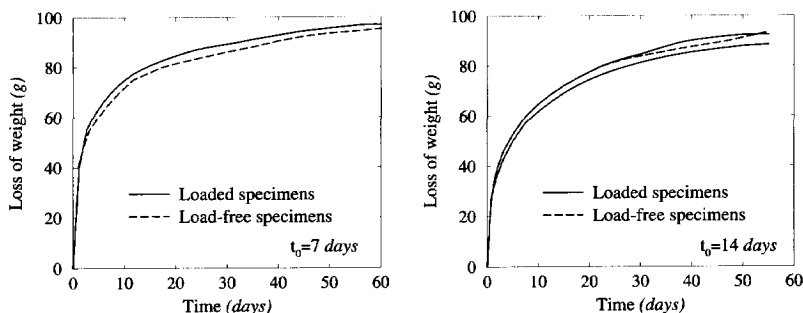


Figure 2.7: Weight loss evolution of identical loaded and unloaded specimens (L'Hermite and Mamillan 1968).

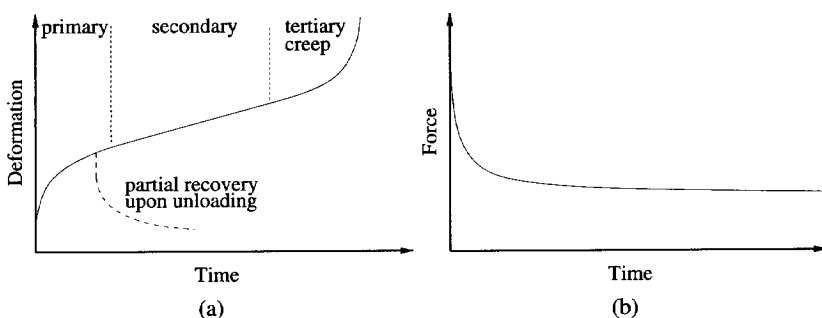


Figure 2.8: (a) Stages of time-dependent deformation under constant load. (b) *Relaxation* of the force required to sustain a constant deformation.

constraint *relaxes* in time, Figure 2.8b. The creep deformation may become several times as large as the instant deformation upon loading, rendering creep an important factor in the medium to long term behaviour of concrete and masonry structures.

Traditionally three stages of “creep” are identified, Figure 2.8a. However, in this representation the total time-dependent deformation, excluding only the free shrinkage, is attributed to creep. The time-dependent crack evolution is not distinguished. In the *primary* stage the initial high creep rate gradually decreases to a constant rate, at which point the *secondary* stage commences. Eventually, an increased deformation rate marks the onset of the *tertiary* stage. In the latter stage the deformation rate increases rapidly until failure occurs. For the last two stages, a sufficiently high level of diffuse micro-cracking has to be initiated by the applied load, which then coalesces into a macro-crack and propagates in the secondary phase and eventually reduces the load bearing capacity to cause failure

under the sustained load.

Only a part of the creep is recovered upon unloading (Lenczner 1981, Young 1988, Neville 1991), Figure 2.8a. This is due to irreversible changes to the microstructure by the hydration process, micro-cracking, as well as the breakage of interpartical bonds by moisture seepage.

It is generally agreed that the mechanisms of shrinkage and those of creep are intertwined. Not only the shrinkage and swelling are dependent on the moisture content and migration, but also the creep (Bažant 1988), though in a different way. For instance, a sealed specimen which is in hygral equilibrium does not shrink, because it does not lose moisture to its environment. Yet, such a specimen creeps under a constant load, due to the forced redistribution of the moisture from the larger, capillary pores into the micropores of the complex pore structure of cementitious materials, where it causes a debonding and re-bonding of solid particles. This means that knowledge of the microscopical moisture transport is necessary to understand and predict creep, in contrast to the adequacy of a macroscopical description of the moisture migration for the reasonable prediction of the shrinkage. This requirement renders the direct determination of the creep impossible, due to the complexity of the microstructure.

Instead, the apparent mechanisms of creep are studied and characterised. The most important factors that have been identified in creep are the stress level, the temperature as well as the moisture content and transport rate. In the characterisation process care must be taken to single out the individual mechanisms to minimise cross-coupling between them, as well as to avoid that behaviour which belongs to another phenomenon, is attributed to creep. For example, sealed specimens should be used and creep should be performed at a constant temperature so that no simultaneous drying and thermal shrinkage occurs, because a coupled effect between these three phenomena otherwise causes an increased total time-dependent deformation, the so-called *Pickett effect* (Pickett 1942), or *drying creep*. Furthermore, the creep load level must be sufficiently low to minimise cracking. The time-dependent deformation at a constant hygral and thermal climate in the absence of cracking defines the *basic creep* (Bažant 1988, Neville 1991). Once the basic creep has been characterised, the cross-coupling effects can be investigated separately. To complete the description of the total time-dependent deformation, the cracking process must be characterised. Such a separate, phenomenological approach is a direct consequence of not modelling the true, microstructural physics of the problem at hand. Yet, it is justified as a pragmatic approach to predict the creep and shrinkage behaviour of cementitious materials in the absence of a complete understanding of the microstructural processes.

2.3.2 CREEP STRESS DEPENDENCE

At low load levels the secondary and tertiary stages of creep, Figure 2.8a, are not entered, but the deformation will continue at a monotonically declining rate. Furthermore, under such low loads, roughly below 40-50% of the instantaneous load capacity (eg. Bažant 1988), the creep appears to be proportional to the stress level, enabling the normalisation of the (primary) creep strain by division with the average stress to give the so-called *specific creep*, or *creep compliance*. The specific creep concept is usually assumed to apply to masonry behaviour as well (eg. Warren and Lenczner 1981, Lenczner 1981, Shrive et al. 1997). Figure 2.9a shows that it is a reasonable approximation. Furthermore, the specific creep reduces with increasing age upon loading, Figure 2.9b. This is attributed to the continuing hydration of cementitious materials and the accompanied decrease in the number of micropores.

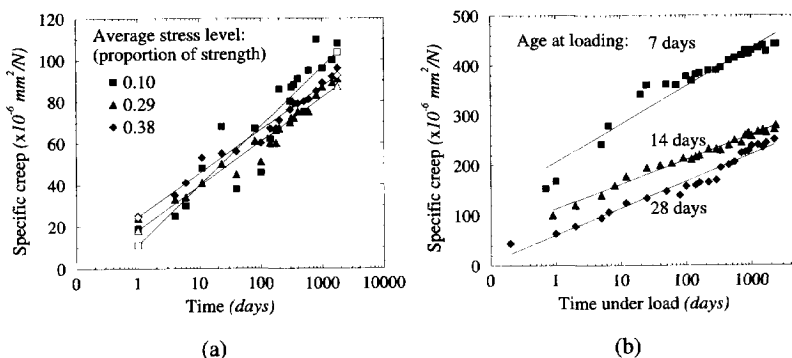


Figure 2.9: (a) Specific creep and (b) its dependence on the age upon loading of a typical clay brick masonry (Sayed-Ahmed et al. 1998).

Already in the previous century this creep linearity was exploited in the formulation of the principle of *superposition* (Boltzmann 1876), which enables the calculation of the strain caused by a stress history by merely adding the creep strains due to increments of stress by which the stress history is discretised.

There are deviations from the proportionality (Bažant 1988). In the low creep load range (below 50% of the peak resistance) it is attributed mainly to the inobjectivity of the determination of the creep, due to simultaneous drying. Thereby cracks may arise, caused by the eigenstressing. The mechanism of the nonproportionality of creep at high stress levels is not clear, but it is likely that the nonlinear response to severe loads due to, for instance the localised cracking in tension and the diffuse cracking in compression, con-

tributes significantly to the increased apparent creep. This phenomenon, as well as the aging process of continued hydration, also accounts to a large extent for the irreversibility of the apparent creep, Figure 2.8a.

2.3.3 CREEP DEPENDENCE ON MOISTURE CONTENT AND TRANSPORT RATE

There is conflicting evidence about the dependence of basic creep on the moisture content, or the environmental humidity. Neville (1959) reported that cementitious specimens, which were allowed to reach hygral equilibrium with the surrounding, constant environmental conditions, showed no significant dependence on the humidity, Figure 2.10a. On the other hand Bažant and Chern (1985) and Wittmann (1968) have claimed that the creep rate is lower for a lower humidity.

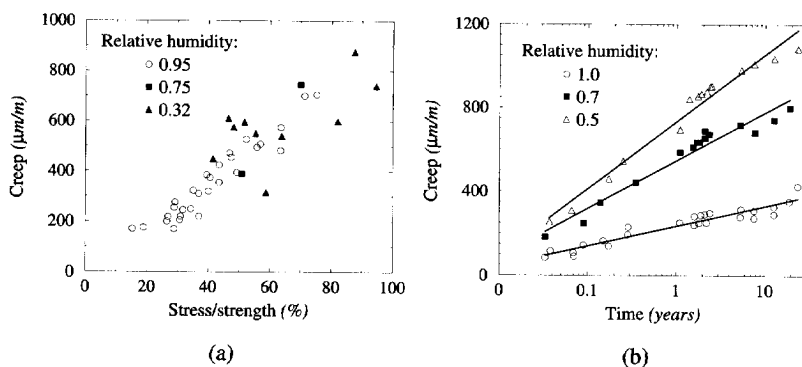


Figure 2.10: Creep dependence on relative humidity of specimens (a) at hygral equilibrium (Neville 1959) and (b) which dry simultaneously from RH=1.0 to the particular, constant relative humidity (Troxell et al. 1958). The drying shrinkage of separate unloaded specimens has been subtracted in (b).

By intuitive reasoning, a completely dry material will not creep, because it lacks the moisture which mobilises creep. In a saturated material, the lack of empty micropores inhibits the moisture transport. Some creep will be caused by the forced redistribution of moisture due to asymmetry of either the microstructure, or the load. For the intermediate moisture contents the presence of free micropores and moisture enhances creep, which probably causes larger creep deformation than in the above moisture content limit cases. This complicates the characterisation of the creep and, together with the scarcity of measurement data of pure basic creep, tempts the analyst to accept the simple result of Figure 2.10a.

If, however, the creep specimens are simultaneously drying to a lower humidity level, i.e. *transient creep* occurs, the creep strain is higher for a lower ambient humidity, Figure 2.10b. In this figure the apparent creep is plotted, which was calculated by subtracting the drying shrinkage of separate, unloaded specimens from the total long-term deformation of the creep specimens (Troxell et al. 1958). This neglects the observed additional creep deformation which occurs when the creep specimens are also subjected to drying shrinkage. The additional creep is called the drying creep, or Pickett effect (Pickett 1942), Figure 2.11. In the figure it is illustrated how the drying creep can be determined experimentally. Simultaneous experiments on three identical specimens are required. One specimen is unloaded and is drying. The second specimen is loaded, but sealed to prevent drying shrinkage. This enables the measurement of the basic creep. The third specimen is loaded and allowed to dry in the same environment as the first specimen. By subtraction of the drying shrinkage, i.e. the deformation of the first specimen, and the basic creep, i.e. the time-dependent deformation of the second specimen, from the total time-dependent deformation of the transient creep specimen, the drying creep is obtained.

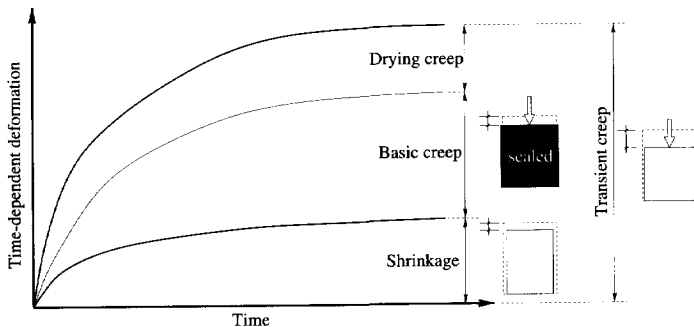


Figure 2.11: Illustration of the Pickett effect/drying creep.

The Pickett effect/drying creep is the subject of continuing investigation. On one hand it is ascribed to the *drying induced creep*, which is the creep dependence on the moisture diffusion rate (Bažant 1988), which increases when moisture can be lost to the environment. However, because of the interaction of the drying shrinkage and the creep under these circumstances, it is not clear whether the supplementary deformation is an increased creep, or whether the drying shrinkage is enhanced. The latter is implied by the *stress-induced shrinkage* coefficient introduced by Bažant and Chern (1985). Wittmann (1980), on the other hand, explains the additional deformation by pointing out that the eigenstressing causes cracking in the unloaded control specimens on which the drying shrinkage is measured for the correction of the creep strain, but not in specimens loaded in compression,

because the load offsets the tensile eigenstresses. The cracking reduces the overall deformation of the control specimens, with the effect that a too small shrinkage is subtracted from the transient creep, rendering a too large creep. For a lower ambient humidity to which the specimens are subjected, the amount of cracking is larger and, therefore, the drying creep will also be larger. It appears that both the drying-induced creep, or the stress-induced shrinkage and the cracking contribute to the Pickett effect (Bažant 1988), as is illustrated in Figure 2.12.

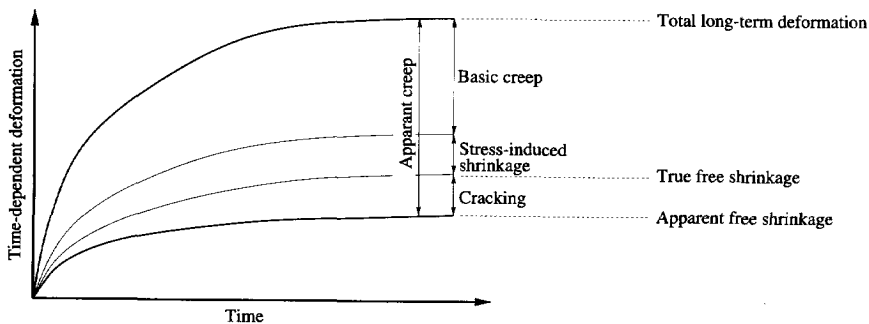


Figure 2.12: Illustration of the contribution by the cracking and stress-induced shrinkage to the Pickett effect.

2.4 Cracking

The complex microstructure of cementitious materials complicates not only the creep process, but also the cracking process. To gain insight in the cracking behaviour, the main features of the behaviour of such materials are usually studied when they are subjected to mechanical loads. Subsequently, mathematical and numerical models are formulated to simulate these features in a macroscopical, phenomenological approach.

With regard to the mechanical behaviour of masonry, a comprehensive discussion has been given by Lourenço (1996). Here, only a brief overview is given to highlight the main features and to illuminate some extensions to his models.

Masonry lends itself to a discrete treatment in the sense of separate consideration of the bricks/blocks and the joints. This is due to the structured arrangement of constituents and the fact that joints usually form the weak links (Page 1978). For such an approach it is sufficient to characterise the cracking behaviour of the joints, while the bricks mostly exhibit a linear elastic response to mechanical loads. Van der Pluijm and Vermeltfoort

(1991) performed deformation-controlled uniaxial tensile tests on small masonry specimens with single joints, Figure 2.13. The average stress-crack displacement response indicates a gradual degradation from the peak strength to a zero residual strength.

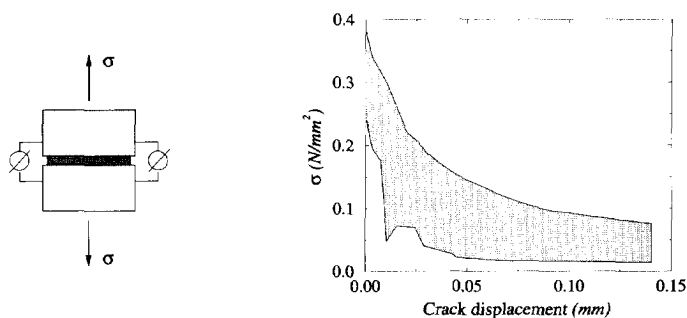


Figure 2.13: Typical clay brick masonry joint tensile behaviour (Van der Pluijm and Vermeltfoort 1991). The shaded area represents the envelope of responses from several tests.

Shear-slipping along the joints is another important feature of the masonry mechanical response. Shear tests on small masonry assemblies (Van der Pluijm 1992) revealed its *Coulomb-friction* nature, Figure 2.14. The peak shear stresses τ for the different, constant normal confining pressures σ indicate that the shear strength is proportional to the confining pressure, but offset with an adhesion strength at zero confining pressure. A gradual degradation of the shear resistance occurs to a residual value, which is also proportional to the confining pressure. At this stage the adhesion is destroyed so that a shearing displacement at zero confinement will have no resistance.

By analysing the shearing responses a trend is found of an increased shearing degradation toughness with increased normal pressure, Figure 2.15a. This toughness is referred to as the shear *fracture energy* and defined by the integral of the shear stress-inelastic shear displacement response between the peak and residual shear strengths. Furthermore, the shearing along the joints is accompanied by *dilatancy*, which is the displacement orthogonal to the shearing plane due to the uneven shearing surface, Figure 2.15b. The prevention of this global volume increase by an external constraint or by internal wedging will cause the build-up of stresses in masonry. However, in what may be called a smoothing action, a sufficient confining pressure and/or a sufficient amount of shear slipping will arrest the normal uplift, Figure 2.15b.

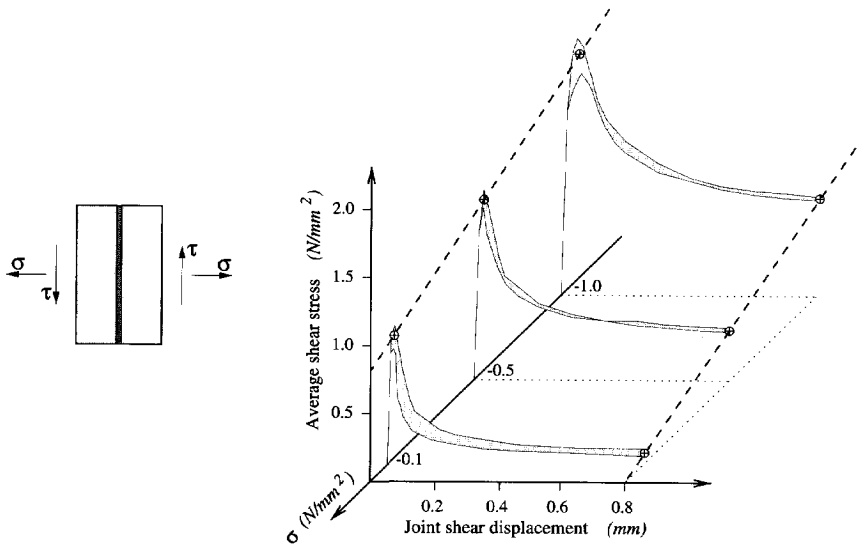


Figure 2.14: Shear test for characterising masonry joint shear behaviour, showing average shear stress-displacement responses at various confining pressures (Van der Pluijm 1992). The shaded areas represent the envelopes of responses from several tests.

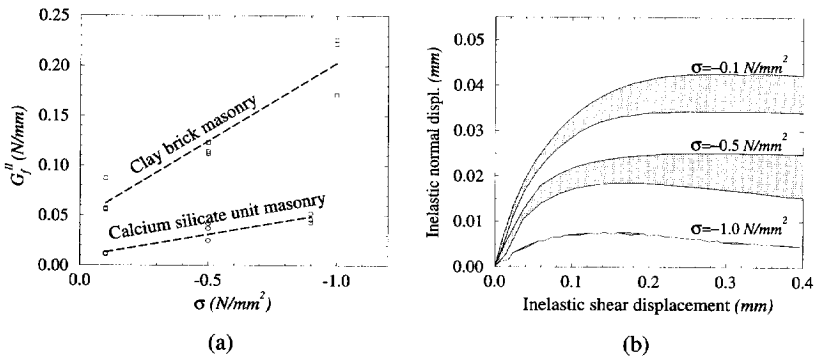


Figure 2.15: Masonry joint (a) shear fracture energy as function of normal confining pressure and (b) dilatancy, or normal uplift during shear slipping (Van der Pluijm 1992). The shaded areas represent the envelopes of responses from several tests.

In large scale analyses the discrete approach is generally not viable. Various experimental programs have been performed to study the behaviour of masonry as a composite material subjected to general, biaxial mechanical loads (Page 1981, 1983, Ganz and Thürlimann 1982, Guggisberg and Thürlimann 1987 and Lurati et al. 1990). From the peak biaxial strength data in Figure 2.16 (Page 1981, 1983) it appears that, as for concrete (eg. Kupfer and Gerstle 1973), a failure envelope exists for masonry. The envelope is asymmetric and dependent on the angle between the loading axes and the material axes, which are conveniently orientated along the joints in the figure. This is due to the inherent anisotropy caused by the brick arrangement, which causes different failure modes for different load orientations (Dhanasekar et al. 1985). As indicated by the lines connecting the points of failure, the specimens were subjected to proportional loads. Nonproportional loads may trigger different failure modes and render the envelopes invalid, but this has not yet been investigated.

The failure envelopes provide a way of approximating the cracking process. Whereas the crack pattern in the uniaxial and biaxial compression regime is usually diffuse, a quite localised failure is found in the tension regime, as well as the tension/compression regime (Dhanasekar et al. 1985). There the peak strength usually coincides with the localisation of the damage in a single crack, which may be considered as the initiation of the *macro-crack*. Unfortunately information about the softening after the peak response under biaxial loading is scarce, which fact hinders the characterisation of the crack growth.

Another important aspect of the mechanical behaviour of cementitious materials is the increase in strength if the loading rate is increased. This is not only the case for high rates, but has been observed for low, quasi-static rates (Rüsch 1960, Bažant and Gettu 1992, Zhou 1992), Figure 2.17. The figure shows the load-deformational responses, which were obtained by the central deflection-controlled three-point bending tests on notched concrete beams. The time it took to reach the peak resistance varied from about 5 seconds for the $50 \mu\text{m/s}$ deflection rate, to 5000 seconds for the $0.05 \mu\text{m/s}$ deflection rate (Zhou 1992). A marked increase in strength is brought about by the rate increase.

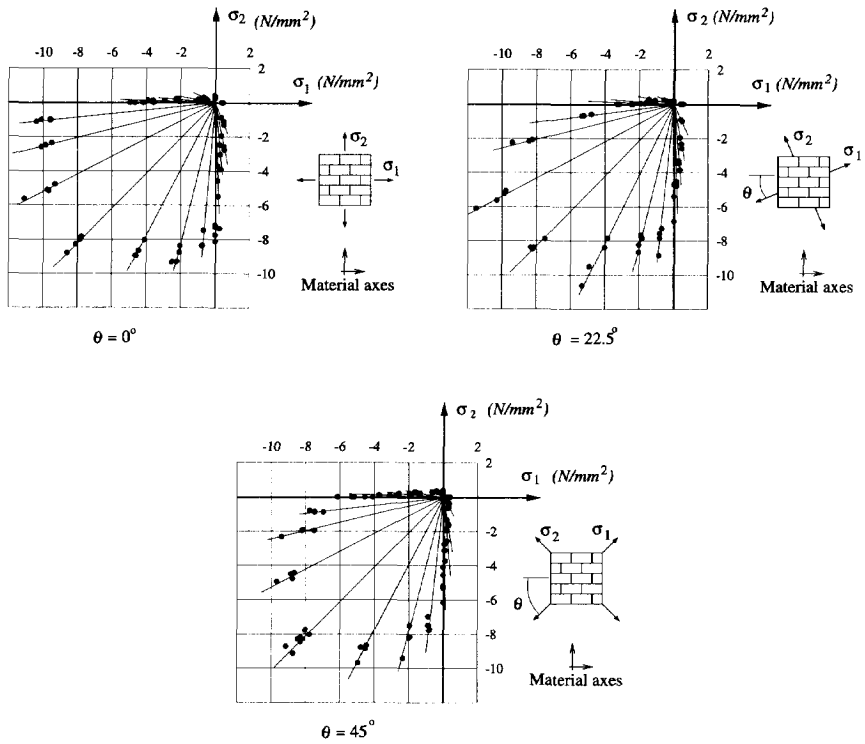


Figure 2.16: Biaxial strength of clay brick masonry (Page 1981, 1983).

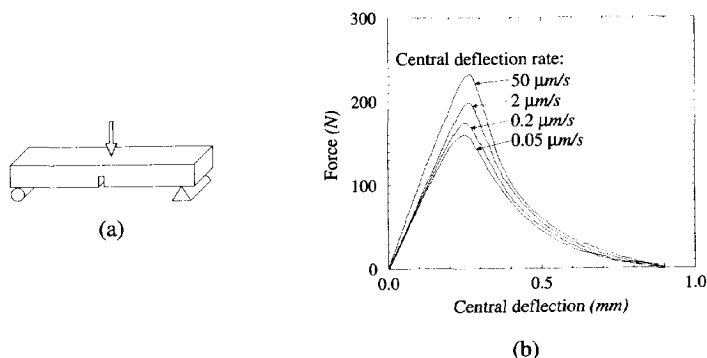


Figure 2.17: (a) Three-point bending test set-up and (b) load-deformational responses for various central deflection rates (Zhou 1992).

2.5 Thermal shrinkage and creep

The thermal shrinkage or expansion of cementitious materials contributes significantly to their volume change. Also, the mechanisms of moisture transport, hygral shrinkage and creep are dependent on the temperature. Nevertheless, this study is restricted to the hygral influence on the long-term behaviour. Isothermal conditions are, therefore, implicitly assumed.

Despite the above restriction, some comments on the thermal interaction are in order. An attractive feature is that, like the moisture diffusion, the thermal conduction process, which describes the evolution of temperature at each material point, is unaffected by the mechanical stresses and strains (Bažant 1988, Bažant and Kaplan 1996). This means that the drying and thermal shrinkage can be determined independently from the mechanical response, i.e. a *one-way coupling* exists between the hygral and thermal diffusive processes on one hand and the mechanical, or stress and strain response on the other hand. Also, apart from the additional contribution of stress-free strain, the analysis of the stress and strain response, including cracking, proceeds exactly as when only hygral effects act. A possible complication lies in the thermal dependence of the creep compliance, of which contradicting evidence exists. A distinction must be made between the normal environmental thermal conditions and exposure to high temperatures, because the nature of the microstructure and the acting mechanisms is changed at temperatures in the range 70°C – 100°C (Bažant 1988, Neville 1991, Bažant and Kaplan 1996). This has been revealed by the intense research effort for the application of concrete in the nuclear industry. In the

normal operating temperature range below about 50°C, an insignificant thermal influence on the creep compliance has been reported by Neville (1991), while a clear trend of increased creep at a higher temperature was established by Hannant (1967). If the latter trend is considered, the creep compliance, or specific creep must be adjusted accordingly before commencing with the mechanical analysis.

However, the main complication of simultaneous hygral and thermal variation is the coupled nature of the moisture transport and the thermal conductivity in cementitious materials (Bažant and Kaplan 1996). Both the moisture and heat flux are driven by moisture content gradients as well as thermal gradients. Another source of the coupling is the heat sorption of free water, which links the conservation of heat with the moisture content. The determination of the moisture and thermal evolutions at each material point, the first step in the calculation of drying and thermal shrinkage strains, would require the simultaneous solution of the two coupled, governing processes. Furthermore, the subsequent estimation of the shrinkage would require the characterisation of the coefficients of drying and thermal shrinkage, which are both functions of moisture content and temperature.

Chapter 3

MATHEMATICAL DESCRIPTION

In this chapter a mathematical framework is developed to capture the features of the time-dependent phenomena shrinkage, creep and cracking of cementitious materials, which were discussed in the previous chapter. Of primary concern is the *hygral response*, which is defined here as the pore humidity evolution, because it governs the time-dependent phenomena of shrinkage and creep in cementitious materials. Therefore, the point of departure will be the formulation of a diffusion equation that describes the hygral response macroscopically. Next, a mathematical formalism is given for the *mechanical response*, which is defined as the stress and deformational response, including the shrinkage and creep, as well as the crack initiation and growth. Also included in the mechanical response is an expression for the drying creep, but in its mathematically equivalent formulation of stress-dependent shrinkage and thermal strain, following Bažant (1988). The observation of a rate-enhanced strength is addressed, by defining a cracking mouth opening rate dependence. The chapter is concluded with some remarks on the adopted formalism.

3.1 Moisture migration

As outlined in sections 2.1 and 2.2 the solution of the various moisture transport phenomena at the micro level in a porous medium, i.e. at the pore level, is hardly possible, due to the complexity of the pore geometry. Besides, for practical relevance a description at the macro level is required. However, the description of the phenomena at the micro level and subsequent volume averaging (Whitaker 1977, Bear and Bachmat 1990) facilitate setting up such a macroscopic formulation. In this spirit the Navier-Stokes equations for the microscopic *liquid* transport are volume-averaged, leading to Darcy's law for macroscopic liquid moisture flux

$$q_l = -d_{\theta l} \nabla \theta_l - d_{Tl} \nabla T, \quad (3.1)$$

where θ_l is the volumetric liquid moisture content, T is the temperature, $d_{\theta l}$ is the liquid moisture diffusivity and d_{Tl} is the thermal liquid moisture diffusivity. Fick's law for the vapour transport in the micropores is volume averaged, giving the expression for macroscopic vapour flux

$$q_v = -d_{\theta v} \nabla \theta_l - d_{Tv} \nabla T, \quad (3.2)$$

where $d_{\theta v}$ is the vapour moisture diffusivity and d_{Tv} is the thermal vapour moisture diffusivity. By addition the total moisture flux is

$$q = -d_{\theta} \nabla \theta_l - d_T \nabla T \quad (3.3)$$

where

$$\begin{aligned} d_{\theta} &= d_{\theta l} + d_{\theta v} \\ d_T &= d_{Tl} + d_{Tv}. \end{aligned} \quad (3.4)$$

By combining the results with the macroscopic descriptions of mass conservation, the moisture flow in a non-saturated, porous medium under hygral and thermal gradients can be described by the nonlinear diffusion-type equation

$$\begin{aligned} \frac{d\theta}{dt} + \nabla \cdot q + Q &= 0 \\ q &= -d_{\theta} \nabla \theta - d_T \nabla T \end{aligned} \quad (3.5)$$

where θ is the total moisture content in liquid phase θ_l and vapour phase θ_v and Q is the rate of moisture loss due to hydration. Note that gravitational effects on the moisture transport have been neglected. See for example Philip and De Vries (1957), or Pel (1995) for comprehensive discussions and the derivation of eq. (3.5).

The nonlinearity is caused by especially the moisture diffusivity being strongly dependent on the moisture content.

It is convenient to write the diffusion process in terms of the relative pore humidity

$$h = p/p_s, \quad (3.6)$$

with p the macroscopical pore pressure and p_s the macroscopical pore pressure at saturation. Since $\theta = \theta(p, T)$ and thus $\theta = \theta(h, T)$ eq. (3.5) becomes

$$\begin{aligned} \frac{dh}{dt} &= -c^{-1} (\nabla \cdot q + Q) - \frac{\partial h}{\partial T} \frac{\partial T}{\partial t} \\ q &= -d_h \nabla h - \left(d_T + d_{\theta} \frac{\partial \theta}{\partial T} \right) \nabla T, \end{aligned} \quad (3.7)$$

where

$$\begin{aligned} c &= \frac{\partial \theta}{\partial h} \\ d_h &= d_\theta c. \end{aligned} \quad (3.8)$$

The parameters in eq. (3.7) can be interpreted physically. The gradient of the hygroscopic relation c reflects the ability to absorb or release water under unit change in h . Furthermore, d_h has been shown to represent permeability (Bažant and Najjar 1971). An added benefit of this formulation is that the influence of the continued hydration can usually be ignored (Bažant 1988). If, in addition, isothermal conditions are assumed, eq. (3.7) reduces to

$$\begin{aligned} \dot{h} &= -c^{-1} \nabla \cdot \mathbf{q} \\ \mathbf{q} &= -d_h \nabla h. \end{aligned} \quad (3.9)$$

Note that the superimposed dot notation has been introduced for the time derivative. Often the fact that the coefficient of absorption c is approximately constant is exploited, for example for concrete in the range $0.2 \leq h \leq 0.95$, simplifying eq. (3.9) to

$$\dot{h} = \nabla \cdot (d_\theta \nabla h). \quad (3.10)$$

In this report the general case of eq. (3.9) will be considered. It is only valid in the hygroscopic range, i.e. where $\frac{\partial \theta}{\partial h}$ is defined. Beyond this range of moisture contents moisture is accumulated in the large (capillary) pores. The migration of the water in these macropores does not contribute to shrinkage, Figure 2.2b.

3.1.1 INITIAL AND BOUNDARY CONDITIONS

A further advantage of employing the relative pore humidity as potential for the diffusion equation is that the boundary conditions can be easily identified:

$$\begin{aligned} \text{essential,} & \quad \text{i.e. prescribed humidity:} & h_B &= h_E \\ \text{natural,} & \quad \text{i.e. prescribed boundary flux:} & \mathbf{q} \cdot \mathbf{n} &= -q_B \\ \text{convective:} & & \mathbf{q} \cdot \mathbf{n} &= \beta(h - h_E) \end{aligned} \quad (3.11)$$

with \mathbf{n} the unit vector pointing outward and normal to the boundary, the subscript B denoting the boundary and the subscript E denoting the prescribed, or environmental value.

The surface convection coefficient β , sometimes referred to as the film coefficient, is given by

$$\beta = \frac{\beta^* p_s}{\rho_l} \quad (3.12)$$

with β^* (s/m) the transfer coefficient depending mainly on air velocity and surface smoothness (Tammes and Vos 1984) and ρ_l (kg/m^3) the liquid moisture mass density.

3.1.2 MOISTURE MIGRATION IN A TWO-PHASE MEDIUM

Masonry is a composite material comprising of bricks/blocks and mortar/lime. It is often assumed that brick/mortar interfaces are hydraulically perfect, i.e. the contact is perfect. This implies that the pressure, of which pore humidity is a measure, is considered to be continuous across the interface:

$$h_b = h_m \quad (3.13)$$

where the subscript b denotes brick/block and the subscript m denotes mortar. However, recent studies of moisture transport across such brick/mortar interfaces have indicated that the contact between the two masonry constituents may not be perfect (Pel 1995), calling for an interfacial hygral resistance to be included in the model (Brocken and Pel 1997). The same authors have since reported that by just slightly varying numerical modelling parameters, the assumption of perfect hydraulic contact does in fact enable numerical simulation of moisture transport across such interfaces (Brocken et al. 1997).

In the current study perfect contact is assumed, implying that, for the general case that the hygroscopic relations for brick and mortar differ, a discontinuity in moisture content occurs at the interface:

$$\theta_b(h_b) \neq \theta_m(h_m). \quad (3.14)$$

For a solution of the differential equation in terms of moisture content (3.5), this discontinuity would require the nonlinear constraint of the interfacial values, complicating the numerical modelling. This is another advantage of adopting the diffusion formalism in terms of the pore humidity (3.9). Figure 3.1 shows the pore humidity and moisture content profiles along a vertical line in the centre of a masonry specimen (Van Zijl 1999b).

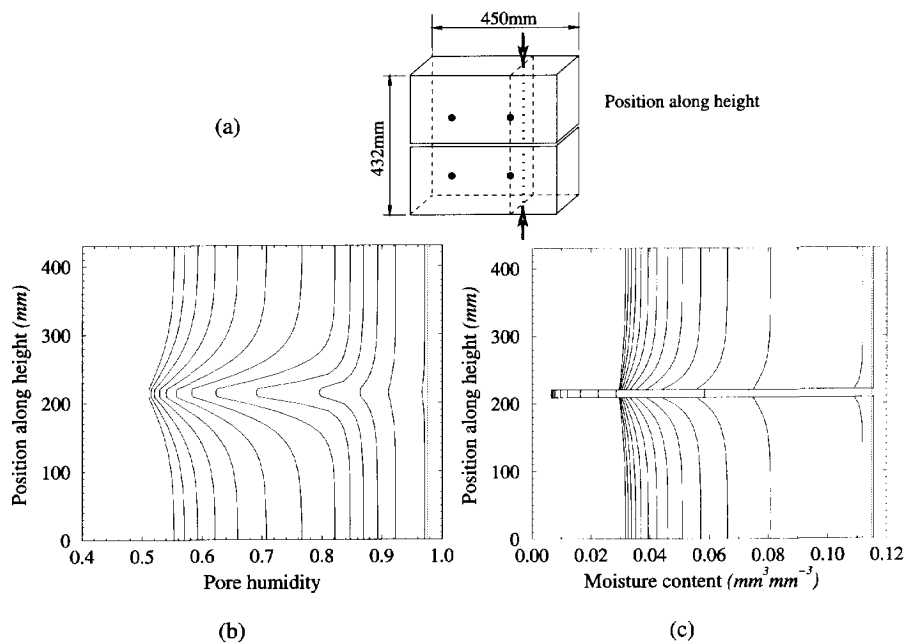


Figure 3.1: Illustration of the moisture content discontinuity across the mortar interface. (a) Line along which the evolution of the (b) pore humidity and (c) moisture content is shown in the single-jointed, drying calcium silicate masonry specimen. The profiles are shown for 1 hour, 1 day and subsequently with 10 day intervals.

3.2 Mechanical behaviour

The usual approach is followed for building the mathematical framework, by firstly considering the static equilibrium in a material point, secondly describing the kinematics of deformation and finally formulating the constitutive law.

The static equilibrium in a material point is described by:

$$\frac{\partial \sigma_{ij}}{\partial x_i} + b_j = 0 \quad (3.15)$$

where σ_{ij} is a second order tensor representing the Cauchy stresses and b_j is a first order tensor of internal body forces. The relation between strains and displacements is given by the kinematic equation for small displacements

$$\epsilon_{ij} = \frac{1}{2} \left(\frac{\partial u_i}{\partial x_j} + \frac{\partial u_j}{\partial x_i} \right). \quad (3.16)$$

To facilitate the description of the constitutive behaviour of the material it is assumed that the strain rate $\dot{\epsilon}$ can be subdivided as follows:

$$\dot{\epsilon} = \dot{\epsilon}_e + \dot{\epsilon}_c + \dot{\epsilon}_s + \dot{\epsilon}_T + \dot{\epsilon}_p \quad (3.17)$$

where ϵ_e is the elastic strain, ϵ_c the creep strain, ϵ_s the shrinkage, ϵ_T the thermal strain and ϵ_p represents the cracking strain. In this way the constitutive laws for the different phenomena can be elaborated independently.

3.2.1 CREEP

Creep in a cementitious material is considered to be closely linked to the viscous processes, section 2.3. Yet, due to the complex microstructure it is not derived directly from the pore humidity evolution. Instead, as has become usual for cementitious materials, visco-elastic behaviour is assumed. This implies the replacement of the sum of the elastic and creep strain with the visco-elastic strain as follows

$$\dot{\epsilon}_{ve} = \dot{\epsilon}_e + \dot{\epsilon}_c. \quad (3.18)$$

The strain evolution can be formulated as

$$\epsilon_{ve}(t) = J(t, \tau) \sigma(t), \quad (3.19)$$

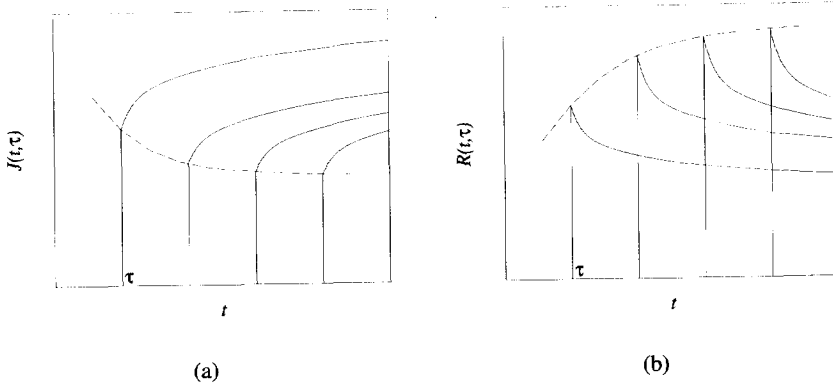


Figure 3.2: (a) Creep and (b) relaxation moduli for various ages τ at loading.

with $J(t, \tau)$ the creep modulus representing the (visco-elastic) strain at time t caused by a unit stress acting since time τ , Figure 3.2a. This formulation exploits the existence of the specific creep, section 2.3.2. It also provides for the reduced creep upon loading at a later maturation age τ , due to the continued hydration. In the absence of aging a single variable creep modulus $J(t - \tau)$ would have been adequate. Furthermore, the creep is considered to be independent of the pore humidity level, following the observations of Neville (1959), Figure 2.10a, section 2.3.3.

Conversely, the one-dimensional stress evolution in a visco-elastic material is given by

$$\sigma(t) = R(t, \tau) \epsilon_{ve}(t) \quad (3.20)$$

if zero initial stresses are assumed. The relaxation function or modulus $R(t, \tau)$ describes the stress evolution at time t due to a unit strain acting since time τ . Age-dependent relaxation moduli typical for concrete are shown in Figure 3.2b.

In order to calculate the strain caused by a variable stress, the principle of superposition, section 2.3.2, implies that the strain due to the stress history is the sum of the responses to all the separate stress increments, leading to:

$$\epsilon_{ve}(t) = \int_0^t J(t, \tau) \dot{\sigma}(\tau) d\tau. \quad (3.21)$$

On the other hand, the strain can be considered to be composed of small increments, which are imposed at times τ . By the principle of superposition the stress response is

equal to the accumulation of the response to each strain increment as follows:

$$\sigma(t) = \int_0^t R(t, \tau) \dot{\epsilon}_{ve}(\tau) d\tau. \quad (3.22)$$

Because of availability of creep experimental data the creep formulation (3.21) is adopted most frequently, but the relaxation formulation is to be preferred when aging, moisture or temperature effects are to be considered. In the latter case $R(t, \tau)$ can be calculated from the creep formulation by considering constant, unit strains imposed as step functions at various ages τ . Here, only the relaxation formulation is developed further, see for example Van Zijl (1999a) for the elaboration of the creep formulation.

The one-dimensional expression is generalised to three dimensions, written in matrix-vector notation as:

$$\sigma(t) = \int_0^t R(t, \tau) D \dot{\epsilon}_{ve}(\tau) d\tau \quad (3.23)$$

where D is the matrix representation of the second order tensor

$$D_{ijkl} = \frac{1}{1+\nu} \left[\frac{\nu}{1-2\nu} \delta_{ij} \delta_{kl} + \frac{1}{2} (\delta_{ik} \delta_{jl} + \delta_{il} \delta_{jk}) \right], \quad (3.24)$$

with ν Poisson's ratio, which is assumed to be time-independent.

The relaxation formulation is an integral form and requires storage and integration of the entire stress or deformation history. Fortunately it is possible to convert the visco-elastic formulation into a rate form, which requires a finite number of so-called internal variables to memorise the history. This conversion is adopted here and entails degeneration of the kernel of the history integral into a Dirichlet series as follows:

$$R(t, \tau) = E_0(\tau) + \sum_{n=1}^N E_n(\tau) e^{-\frac{t-\tau}{\zeta_n}} \quad (3.25)$$

where E_n is the stiffness modulus of element n , depending on the loading age τ and ζ_n is the relaxation time. Instead of a Dirichlet series, a Taylor series degeneration can be performed. The latter is preferable when short time spans have to be analysed, for instance for the behaviour of young concrete, where pronounced stress fluctuations may occur (De Borst and Van den Boogaard 1993). The Dirichlet series is applicable to the long term behaviour of shrinkage and creep and will be elaborated here.

Replacement of the relaxation kernel in eq. (3.23) by the Dirichlet series (3.25) produces

$$\sigma(t) = \int_0^t \left[E_0(\tau) + \sum_{n=1}^N E_n(\tau) e^{-\frac{t-\tau}{\zeta_n}} \right] D \dot{\epsilon}_{ve}(\tau) d\tau \quad (3.26)$$

which, upon time differentiation becomes

$$\dot{\sigma}(t) = E_0(t) D\dot{\epsilon}_{ve}(t) + \sum_{n=1}^N \dot{\sigma}_n(t) \quad (3.27)$$

where

$$\sigma_n(t) = \int_0^t E_n(\tau) e^{-\frac{t-\tau}{\zeta_n}} D\dot{\epsilon}_{ve}(\tau) d\tau. \quad (3.28)$$

Time differentiation of (3.28) (with the aid of Leibnitz' rule) reveals that

$$\dot{\sigma}_n(t) = E_n(t) D\dot{\epsilon}_{ve}(t) - \frac{1}{\zeta_n} \sigma_n(t). \quad (3.29)$$

By the inspection of eqs. (3.27) and (3.29) it becomes clear that this visco-elastic formulation can be represented by a Maxwell chain, with E_n the spring stiffness and $\eta_n = \zeta_n E_n$ the dashpot viscosity of each element, as shown schematically in Figure 3.3a. If the point of departure is the creep formulation (3.21), a visco-elastic law is derived, which can be represented by a Kelvin chain model, Figure 3.3b (Van Zijl 1999a). As mentioned before, the Maxwell formulation is chosen here.

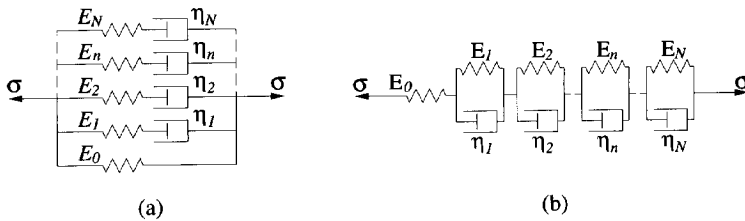


Figure 3.3: (a) Maxwell and (b) Kelvin chain models.

From eqs. (3.27) and (3.29) it is possible to express the stress rate as

$$\dot{\sigma} = D^{ve} \dot{\epsilon}_{ve} + \Sigma \quad (3.30)$$

where D^{ve} is an equivalent stiffness modulus, which is dependent only on the current time t , and Σ is a viscous stress term which accounts for the history, by virtue of a fading memory. It will be shown in the next chapter that the latter term can be represented by a few state variables, avoiding the repeated evaluation of the entire stress history.

3.2.2 DRYING AND THERMAL SHRINKAGE

In this section the phenomena of hygral and thermal shrinkage/expansion are addressed. As discussed in Chapter 2, these phenomena are governed by the moisture and thermal diffusive processes. There it was mentioned that they are coupled and require the solution of a set of coupled partial differential equations, which is not embarked upon in this study, where the focus is on the hygral processes. Nevertheless, due to the one-way coupled nature of the thermal and hygral diffusion processes on one hand and the mechanical response on the other hand, provision is made for both sources of stress-free strain in the mechanical formulation. In this way the mechanical response to a variable environmental humidity and temperature can be analysed if the pore humidity and temperature evolutions are known.

3.2.2.1 Free drying shrinkage and thermal strain

There is general agreement that the drying shrinkage of cementitious materials is driven by the pore pressure (Wittmann 1977, Bažant 1988), section 2.1. The free drying shrinkage is usually obtained from the incremental relation:

$$\dot{\epsilon}_{s,o} = \alpha_s \dot{h}. \quad (3.31)$$

Experimental measurements indicate that the shrinkage coefficient α_s is constant in the range $0.4 \leq h \leq 0.99$, but Van Zijl (1999b) showed by inverse fitting that a polynomial function of h may be more appropriate. This poses no mathematical or numerical difficulty, but until more experimental evidence is obtained, the constant relation is assumed. Eq. (3.31) can be generalised to three dimensions and allowing for a different free shrinkage in orthotropic directions, one obtains

$$\dot{\epsilon}_s = \dot{\epsilon}_{s,o} \mathbf{P}_s, \quad (3.32)$$

where \mathbf{P}_s is a scaling, normalised vector defined as

$$\mathbf{P}_s = [P_{sx} \ P_{sy} \ P_{sz} \ 0 \ 0 \ 0]^T. \quad (3.33)$$

The thermal strains are related to the temperature in a similar way:

$$\dot{\epsilon}_T = \dot{\epsilon}_{T,o} \mathbf{P}_T, \quad (3.34)$$

with

$$\dot{\epsilon}_{T,o} = \alpha_T \dot{T}, \quad (3.35)$$

where α_T is the thermal expansion coefficient and

$$\mathbf{P}_T = [P_{Tx} P_{Ty} P_{Tz} 0 0 0]^T \quad (3.36)$$

provides for orthotropic thermal expansion.

3.2.2.2 Stress-dependent shrinkage and thermal strain

To address the phenomenon of drying creep, or the Pickett effect (Pickett 1942), the influence of the pore humidity rate on the creep is investigated. Bažant (1988) has attempted to find a physical rationale for this effect. He argues that it is reasonable to assume that the breakage of bonds in the micropores, which is commonly believed to be the physical mechanism of creep, is promoted by moisture flux. Therefore, it can be postulated that the creep rate, and thus the viscosity, is dependent on the moisture flux. This dependence is argued to be equivalent to the viscosity dependence on the humidity rate \dot{h} and thermal rate \dot{T} , expressed as (Bažant 1988)

$$\frac{1}{\eta} = \frac{1}{\eta_o} + \chi|\dot{h} + c\dot{T}|, \quad (3.37)$$

with η_o the viscosity at zero moisture flux and χ and c positive constants. With (3.37) the differential equation for a one-dimensional Maxwell unit reads:

$$\frac{\dot{\sigma}}{E} + \left(\frac{1}{\eta_o} + \chi|\dot{h} + c\dot{T}| \right) \sigma = \dot{\epsilon} - \alpha_s \dot{h} - \alpha_T \dot{T}, \quad (3.38)$$

which can be rewritten as

$$\frac{\dot{\sigma}}{E} + \frac{\sigma}{\eta_o} = \dot{\epsilon} - \alpha_s (1 + r_s \sigma) \dot{h} - \alpha_T (1 + r_T \sigma) \dot{T}, \quad (3.39)$$

with

$$\begin{aligned} r_s &= \frac{\chi}{\alpha_s} \text{sign}(\dot{h} + c\dot{T}) \\ r_T &= \frac{\chi c}{\alpha_T} \text{sign}(\dot{h} + c\dot{T}). \end{aligned} \quad (3.40)$$

Thus it can be seen that the viscosity dependence on humidity and thermal rate is equivalent to a stress-induced shrinkage and thermal shrinkage. An experimental scheme for quantifying the stress-induced shrinkage coefficient r_s for masonry objectively is described by Van Zijl (1999b). With the values for concrete reported to be (Bažant and

Chern 1985)

$$\begin{aligned} 0.1/f_t \leq |r_s| \leq 0.6/f_t \\ |r_T| \approx 2.5/f_t, \end{aligned} \quad (3.41)$$

f_t being the tensile strength, the contribution of this phenomenon is significant and therefore included in the current model.

In three dimensions (3.39) can be expressed as

$$\frac{1}{E} \mathbf{D}^{-1} \dot{\boldsymbol{\sigma}} + \frac{1}{\eta} \mathbf{D}^{-1} \boldsymbol{\sigma} = \dot{\boldsymbol{\epsilon}} - \dot{\boldsymbol{\epsilon}}_s - \dot{\boldsymbol{\epsilon}}_T, \quad (3.42)$$

with

$$\begin{aligned} \dot{\boldsymbol{\epsilon}}_s &= \alpha_s (\mathbf{P}_s + \mathbf{r}_s \boldsymbol{\sigma}) \dot{h} \\ \dot{\boldsymbol{\epsilon}}_T &= \alpha_T (\mathbf{P}_T + \mathbf{r}_T \boldsymbol{\sigma}) \dot{T}. \end{aligned} \quad (3.43)$$

Provision is made for orthotropy by defining the stress-induced shrinkage and thermal expansion coefficient matrices as

$$\begin{aligned} \mathbf{r}_s &= \text{diag} [r_{sx} \ r_{sy} \ r_{sz} \ 0 \ 0 \ 0] \\ \mathbf{r}_T &= \text{diag} [r_{Tx} \ r_{Ty} \ r_{Tz} \ 0 \ 0 \ 0]. \end{aligned} \quad (3.44)$$

3.2.3 CRACKING

As for the creep, a phenomenological approach is followed for modelling cracking. The mechanisms are modelled in such a manner that the simulated response is in reasonable agreement with experimental observations, section 2.4. Cracks are considered to form and grow at predefined locations in the discrete approach, or are smeared over a finite width, while the damaged material still behaves as a continuum to which the notions of stress and strain apply. In the latter case no pre-knowledge is needed where cracks are likely to occur. For both cases a consistent plasticity formulation is chosen. Due to the elastic unloading modulus, this formulation is not suitable for analysing the response of quasi-brittle materials to cyclic loading. Also, its realistic capturing of crack propagation, which is accompanied by some material points being unloaded, is questionable. Yet, it has been shown to capture global, quasi-static response of concrete (Feenstra 1993, De Borst et al. 1994) and masonry structures (Lourenço 1996) reasonably well. Therefore,

it is considered to be a pragmatic choice, due to its supremacy in terms of robustness and solution convergence speed.

The stress rate is related to the elastic strain rate by the elastic stiffness matrix D^e

$$\dot{\sigma} = D^e \dot{\epsilon}_e, \quad (3.45)$$

which, when considering the rate form of visco-elasticity in eq. (3.30) and the decomposition of strains (3.17), can be written as

$$\dot{\sigma} = D^{ve} (\dot{\epsilon} - \dot{\epsilon}_s - \dot{\epsilon}_T - \dot{\epsilon}_p) + \Sigma. \quad (3.46)$$

Note that, in the case of discrete analysis of masonry, the different phenomena are separated in the sense that the plastic flow is captured by interface elements, while the creep, shrinkage and thermal strains are accounted for by continuum elements.

To establish whether yielding occurs, a yield function, which bounds the (visco-)elastic domain

$$f(\sigma, \kappa, \dot{\kappa}) \leq 0, \quad (3.47)$$

is evaluated, where κ is an equivalent strain or degradation parameter. The Kuhn-Tucker conditions

$$\dot{\lambda} \geq 0 \quad f \leq 0 \quad \dot{\lambda} f = 0 \quad (3.48)$$

enable convenient distinction between loading and unloading at a material point, where $\dot{\lambda}$ is the plastic flow rate. When yielding, or plastic flow is detected, the plastic strain is calculated from the non-associative plastic flow rule

$$\dot{\epsilon}_p = \dot{\lambda} \frac{\partial g}{\partial \sigma} \quad (3.49)$$

where the plastic potential function g can be written as

$$g = g(\sigma, \kappa). \quad (3.50)$$

The yield surface can grow or shrink according to a hardening or softening rule. The hardening/softening rule is usually dependent on the equivalent strain or degradation parameter κ , which is derived from a strain hardening/softening or a work hardening/softening hypothesis. An example of the former is

$$\dot{\kappa} = \sqrt{\frac{1}{2} \dot{\epsilon}_p^T \dot{\epsilon}_p}, \quad (3.51)$$

and of the latter:

$$\dot{\kappa} = \sigma^T \dot{\epsilon}_p. \quad (3.52)$$

In the case of complex material behaviour it is often impossible to define a single yield function, enforcing the use of multi-surface plasticity. The intersections of the yield functions form singular points. Koiter's generalised plastic flow rule (Koiter 1953) suggests a linear combination of the plastic strain rates obtained from the two intersecting yield surfaces as follows

$$\dot{\epsilon}_p = \dot{\lambda}_1 \frac{\partial g_1}{\partial \sigma} + \dot{\lambda}_2 \frac{\partial g_2}{\partial \sigma}. \quad (3.53)$$

3.2.4 CRACK MOUTH OPENING RATE DEPENDENCE

A mathematical formalism to capture the rate-enhanced strength of cementitious materials, as observed for instance by Zhou (1992), Figure 2.17, is given next. The source of the rate dependence is sought in the viscosity of the cracking process. The time-dependence of the behaviour of cementitious materials is caused not only by the *bulk creep*, which is defined here as the creep in the bulk of the material, as it is represented by the Maxwell chain, but also by the rate-dependence of the breakage of bonds in the fracture process zone. Bažant (1993) has derived a formulation for the latter rate effect from the theory of *activation energy*, according to which the rupture of a bond requires that the limiting bond potential, called the activation energy, be exceeded. Departing from the Maxwell-Boltzmann distribution of the frequency of exceedence of the activation energy, the following expression for the crack opening rate \dot{w} can be derived (Wu and Bažant 1993):

$$\dot{w} = \dot{w}_r \sinh \left[\frac{\sigma - \sigma_t(w)}{k_0 [\sigma_t(w) + k_1 f_t]} \right] e^{\frac{Q}{RT_0} - \frac{Q}{RT}} \quad (3.54)$$

where \dot{w}_r is a constant, reference crack opening velocity, $\sigma_t(w)$ describes the strength degradation with infinitely slow crack opening displacement, Q is the activation energy, R the gas constant and T_0 the reference temperature. The material parameter k_0 is estimated to be in the range 0.01 - 0.08 from the knowledge that for a 10^4 -fold increase of the loading rate a 25% increase in peak strength is found experimentally. The material parameter k_1 is an offset factor to prevent the denominator in eq. (3.54) from becoming zero. For isothermal conditions and by approximating the crack opening displacement $w = l_b \kappa$, with l_b the crack band width and κ the crack strain, eq. (3.54) can be rewritten as

$$\sigma = \sigma_t(\kappa) \left[1 + k_0 \sinh^{-1} \left(\frac{\dot{\kappa}}{\dot{\kappa}_r} \right) \right] + k_0 k_1 f_t \sinh^{-1} \left(\frac{\dot{\kappa}}{\dot{\kappa}_r} \right). \quad (3.55)$$

A simple, alternative approach is illustrated in Figure 3.4. Following Sluys (1992), De Borst et al. (1993) and Wang (1997) the crack rate dependence is captured via a dashpot of viscosity m in parallel to the plasticity elements. The rate-dependent cracking stress is written as

$$\sigma = \sigma_t(\kappa) \left[1 + \frac{m}{f_t} \dot{\kappa} \right], \quad (3.56)$$

which implies that the rate term is degraded with increasing crack width to avoid a residual strength. The viscosity m should be derived from experimental strength tests at various loading rates. However, such tests should represent the rates of the physical process which are to be simulated.

Both eqs. (3.55) and (3.56) have been incorporated in the yield criterion (3.47), causing its equivalent strain rate dependence.

3.3 Discussion

The combined constitutive model for the mechanical behaviour can be represented rheologically by the series coupling of a Maxwell chain, a shrinkage and thermal source and a module accounting for the cracking, as illustrated in Figure 3.4. The simple, one-way coupled approach is justified by the main objective of this study, which is to formulate a model that can rigorously describe the time-dependent behaviour of cementitious materials, specifically masonry. It is also motivated by the scarcity of experimental data to characterise subtle interdependencies and the computational effort to solve them.

A brief reflection on the inclusion of the cracking rate dependence is in order. It has been introduced in the first place to account for the observed strength increase with an increased loading rate in a phenomenological way. However, the contribution of the cracking rate to the strength, eq. (3.56), has been shown to have a stabilising influence in dynamic

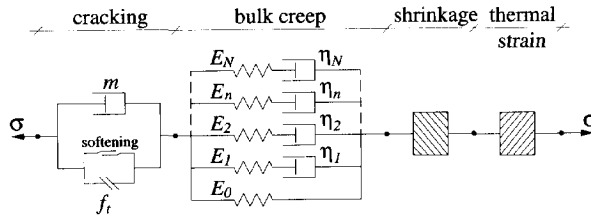


Figure 3.4: Maxwell chain model with cracking, thermal and shrinkage strain elements in series.

problems (Sluys 1992, Wang 1997), as well as quasi-static problems (De Borst et al. 1993, Wang 1997), under which the problem at hand is categorised. The loss of hyperbolicity and ellipticity of the governing equations of dynamic and quasi-static problems respectively, are avoided. The symptoms of these mathematical instabilities, namely the emergence of difficulties upon the numerical solution of these problems and the ensuing inobjectivity with regard to crack orientation and spacing, are then resolved.

Chapter 4

NUMERICAL SOLUTION

To enable the solution of practical problems, a numerical solution of the mathematical formulation is sought. The finite element (FE) method is adopted. The transformation of the governing set of differential equations to a set of ordinary equations is a well-established procedure and described in detail by, for instance, Becker et al. (1981), Bathe (1982) and Zienkiewicz (1986).

The decoupling of the hygral and the mechanical responses enables separate treatment. Therefore, the weak formulation, the finite element discretisation and the iterative solution of these phenomena are elaborated separately. Finally, some remarks are made about the order of the finite element interpolation.

4.1 Moisture migration

4.1.1 WEIGHTED RESIDUAL FORMULATION

The diffusion equation (3.9) states the process at hand in the *strong* form, i.e. the conditions must be met at each material point. For a numerical approximation the *weak* form is adopted. Now the conditions are met only in an average sense

$$\int_V W (\dot{c}h + \nabla \cdot \mathbf{q}) \, dV = \int_V W \epsilon \, dV = 0, \quad (4.1)$$

where W is a weight function to force the error or residual ϵ to zero in a volume-averaged sense. To reduce the order of the differential equation and to introduce non-essential boundary conditions, the theorem of *Gauß* is applied, giving

$$\int_V W \dot{c}h \, dV - \int_V \nabla W \cdot \mathbf{q} \, dV + \int_B W \mathbf{q} \cdot \mathbf{n} \, dB = 0. \quad (4.2)$$

Assuming natural conditions at a part of the boundary B_N and surface convection on another part of the boundary B_C cf. eqs. (3.11,3.12), eq. (4.2) becomes

$$\int_V W c \dot{h} dV - \int_V \nabla W \cdot \mathbf{q} dV + \int_{B_C} W \beta h dB = \int_{B_N} W q_B dB + \int_{B_C} W \beta h_E dB. \quad (4.3)$$

4.1.2 FINITE ELEMENT FORMULATION

In the FE approach to solve eq. (4.3) the domain is discretised into finite elements. Instead of selecting trial functions that satisfy global boundary conditions, approximation or interpolation functions are selected to satisfy the element boundary conditions. A variable is approximated within each element as follows:

$$h^e = \mathbf{N}^e \mathbf{h}^e \quad (4.4)$$

where \mathbf{N}_e is a matrix of element interpolation functions and \mathbf{h}^e the vector of relative humidities at discrete points on the boundary and/or within the element. Also, in the Galerkin approach, the weight function W is chosen to be of the same class as the interpolation functions \mathbf{N} . By substitution of (4.4) and (3.9b), eq. (4.3) now becomes

$$\begin{aligned} \int_{V^e} \mathbf{N}^T c \mathbf{N} \dot{\mathbf{h}} dV + \int_{V^e} (\nabla \mathbf{N})^T \mathbf{d}_h \nabla \mathbf{N} \mathbf{h} dV + \int_{B_C^e} \mathbf{N}^T \beta \mathbf{N} \mathbf{h} dB = \\ \int_{B_N^e} \mathbf{N}^T q_B dB + \int_{B_C^e} \mathbf{N}^T \beta h_E dB \end{aligned} \quad (4.5)$$

in each element. For clarity the superscripts e have been retained only on the symbols for the integration domains. Eq. (4.5) can be written symbolically as

$$\mathbf{C}^e \dot{\mathbf{h}}^e + \mathbf{D}_h^e \mathbf{h}^e = \mathbf{Q}^e \quad (4.6)$$

with

$$\begin{aligned} \mathbf{C}^e &= \int_{V^e} \mathbf{N}^T c \mathbf{N} dV \\ \mathbf{D}_h^e &= \int_{V^e} (\nabla \mathbf{N})^T \mathbf{d}_h \nabla \mathbf{N} dV + \int_{B_C^e} \mathbf{N}^T \beta \mathbf{N} dB \\ \mathbf{Q}^e &= \int_{B_N^e} \mathbf{N}^T q_B dB + \int_{B_C^e} \mathbf{N}^T \beta h_E dB. \end{aligned} \quad (4.7)$$

By accumulation of contributions from all elements the set of differential equations are assembled as

$$\mathbf{C} \dot{\mathbf{h}} + \mathbf{D}_h \mathbf{h} = \mathbf{Q}. \quad (4.8)$$

where \mathbf{h} contains the relative pore humidities at the discrete points employed for discretising the domain.

4.1.3 TIME INTEGRATION

Eq. (4.8) is solved step-wise by direct time integration for each time step Δt at time $t + \alpha \Delta t$, $0 \leq \alpha \leq 1$ in a generalised trapezoidal fashion. Hereby the set of differential equations is converted into a set of ordinary equations

$$D_h^* \dot{h}^* = Q^* \quad (4.9)$$

with

$$\begin{aligned} h^* &= {}^{t+\alpha\Delta t}h \\ D_h^* &= {}^{t+\alpha\Delta t}C + \alpha \Delta t \quad {}^{t+\alpha\Delta t}D_h \\ Q^* &= \alpha \Delta t \quad {}^{t+\alpha\Delta t}Q + {}^{t+\alpha\Delta t}C \quad {}^th. \end{aligned} \quad (4.10)$$

In eq. (4.10) use is made of the time derivative

$${}^{t+\alpha\Delta t}\dot{h} = \frac{{}^{t+\alpha\Delta t}h - {}^th}{\alpha \Delta t}. \quad (4.11)$$

In this study fully implicit *Euler backward* integration has been used by selecting $\alpha = 1$.

4.1.4 INCREMENTAL ITERATIVE SOLUTION PROCEDURE

Due to the nonlinearity of eq. (4.9), caused by the dependence of the diffusivity and the moisture capacity on the pore humidity, an incremental-iterative solution procedure is followed:

$$h_{i+1}^* = h_i^* + (D_{inc})^{-1} (Q_i^* - D_{h,i}^* h_i^*), \quad (4.12)$$

where i denotes the convergence iteration number. Here, either the *regular* Newton-Raphson method is employed, rendering

$$D_{inc} = D_{h,i}^*, \quad (4.13)$$

or the modified Newton-Raphson method, when

$$D_{inc} = D_{h,1}^*. \quad (4.14)$$

4.2 Mechanical response

4.2.1 WEAK FORMULATION

The mathematical formulation of equilibrium (3.15), the kinematic relation (3.16) and the constitutive law (3.46) state the process at hand in the *strong* form, requiring the conditions to be met at each material point. For a numerical solution a *weak* form of the equilibrium eq. (3.15) is adopted:

$$\int_V \delta u_j \left(\frac{\partial \sigma_{ij}}{\partial x_i} + b_j \right) dV = 0. \quad (4.15)$$

This form corresponds to the principle of virtual work, stating that when a body, which is in a state of equilibrium, is disturbed by an admissible virtual displacement δu_j , the net work performed is zero. After integration by parts, substitution of the kinematic eq. (3.16) and taking account of rotational equilibrium, which implies symmetry of the Cauchy stress tensor ($\sigma_{ij} = \sigma_{ji}$), the principle of virtual work can be expressed as

$$\int_V \delta \epsilon_{ij} \sigma_{ij} dV = \int_V \delta u_j b_j dV + \int_V \frac{\partial}{\partial x_i} (\sigma_{ij} \delta u_j) dV. \quad (4.16)$$

The left hand side represents the internal energy and the right hand side the external work. By applying the Gauss divergence theorem, the third term volume integral is transformed into a surface integral

$$\int_V \delta \epsilon_{ij} \sigma_{ij} dV = \int_V \delta u_j b_j dV + \int_B \delta u_j \sigma_{ij} n_i dB, \quad (4.17)$$

which introduces the static boundary conditions of prescribed tractions ($\sigma_{ij} n_i$). For convenience, the matrix-vector notation is adopted so that eq. (4.17) can be written as

$$\int_V \delta \mathbf{\epsilon}^T \boldsymbol{\sigma} dV = \int_V \delta \mathbf{u}^T \mathbf{b} dV + \int_B \delta \mathbf{u}^T \mathbf{t} dB. \quad (4.18)$$

4.2.2 FINITE ELEMENT SOLUTION

In the FE method eq. (4.18) is assumed to apply to each finite element into which the structural geometry is subdivided. Furthermore, the displacements are approximated in each element by interpolation of the element nodal displacements $\hat{\mathbf{u}}$ as follows:

$$\mathbf{u}^e = \mathbf{N}^e \hat{\mathbf{u}}^e, \quad (4.19)$$

where the superscript e indicates that the variable applies to an element and N^e is a vector of interpolation functions that satisfy the element boundary conditions. By writing the kinematic relation (3.16) in matrix-vector notation

$$\boldsymbol{\epsilon}^e = \mathbf{L}^e \mathbf{u}^e = \mathbf{L}^e \mathbf{N}^e \hat{\mathbf{u}}^e = \mathbf{B}^e \hat{\mathbf{u}}^e, \quad (4.20)$$

eq. (4.18) becomes

$$\int_{V^e} \delta \hat{\mathbf{u}}^T \mathbf{B}^T \boldsymbol{\sigma} dV^e = \int_{V^e} \delta \hat{\mathbf{u}}^T \mathbf{N}^T \mathbf{b} dV^e + \int_{B^e} \delta \hat{\mathbf{u}}^T \mathbf{N}^T \mathbf{t} dB^e \quad (4.21)$$

where, for clarity, the superscripts have been retained only on the integration domains. The right hand side of eq. (4.21) comprises the virtual work done by body forces and boundary/surface tractions. These forces can be condensed into a vector of element forces

$$\mathbf{r}_e = \int_{V^e} \mathbf{N}^T \mathbf{b} dV^e + \int_{B^e} \mathbf{N}^T \mathbf{t} dB^e. \quad (4.22)$$

Considering that eq. (4.21) must hold for any kinematically admissible virtual displacement $\delta \hat{\mathbf{u}}$, the elemental equilibrium reads

$$\int_{V^e} \mathbf{B}^T \boldsymbol{\sigma} dV^e = \mathbf{r}_e. \quad (4.23)$$

Eq. (4.23) is the point of departure for the development of the solution algorithm. However, the numerical integration of the constitutive relation must be addressed first.

4.2.3 INTEGRATION OF THE VISCO-ELASTICITY CONSTITUTIVE EQUATION

For evaluation of the integral form of the relaxation or creep eq. (3.23) the implication of considering the total stress (or strain) history at each material point has inspired a reformulation into a differential or rate-type eq. (3.27), see section 3.2.1. However, further elaboration of the latter rate form is required to make it suitable for FE solution. For this purpose it is convenient to return to the second last step of the transformation, eq. (3.26), and evaluate it at time $t + \Delta t$, divided into two intervals $0 \rightarrow t$ and $t \rightarrow t + \Delta t$ as follows:

$$\begin{aligned} {}^{t+\Delta t}\boldsymbol{\sigma} &= \boldsymbol{\sigma}(t + \Delta t) \\ &= \int_0^t E_0(\tau) \mathbf{D} \dot{\boldsymbol{\epsilon}}_{ve}(\tau) d\tau + \sum_{n=1}^N \int_0^t E_n(\tau) e^{-\frac{t+\Delta t-\tau}{\zeta_n}} \mathbf{D} \dot{\boldsymbol{\epsilon}}_{ve}(\tau) d\tau \\ &\quad + \int_t^{t+\Delta t} E_0(\tau) \mathbf{D} \dot{\boldsymbol{\epsilon}}_{ve}(\tau) d\tau + \sum_{n=1}^N \int_t^{t+\Delta t} E_n(\tau) e^{-\frac{t+\Delta t-\tau}{\zeta_n}} \mathbf{D} \dot{\boldsymbol{\epsilon}}_{ve}(\tau) d\tau. \end{aligned} \quad (4.24)$$

Note that

$${}^t\sigma = \int_0^t E_0(\tau) D\dot{\epsilon}_{ve}(\tau) d\tau + \sum_{n=1}^N \int_0^t E_n(\tau) e^{-\frac{t-\tau}{\zeta_n}} D\dot{\epsilon}_{ve}(\tau) d\tau \quad (4.25)$$

which, upon substitution into eq. (4.24) enables writing

$$\begin{aligned} \Delta\sigma &= {}^{t+\Delta t}\sigma - {}^t\sigma \\ &= \int_t^{t+\Delta t} E_0(\tau) D\dot{\epsilon}_{ve}(\tau) d\tau + \sum_{n=1}^N \int_t^{t+\Delta t} E_n(\tau) e^{-\frac{t+\Delta t-\tau}{\zeta_n}} D\dot{\epsilon}_{ve}(\tau) d\tau \\ &\quad + \sum_{n=1}^N \int_0^t E_n(\tau) e^{-\frac{t+\Delta t-\tau}{\zeta_n}} D\dot{\epsilon}_{ve}(\tau) d\tau - \sum_{n=1}^N \int_0^t E_n(\tau) e^{-\frac{t-\tau}{\zeta_n}} D\dot{\epsilon}_{ve}(\tau) d\tau. \end{aligned} \quad (4.26)$$

This can be simplified to

$$\begin{aligned} \Delta\sigma &= \int_t^{t+\Delta t} E_0(\tau) D\dot{\epsilon}_{ve}(\tau) d\tau + \sum_{n=1}^N \int_t^{t+\Delta t} E_n(\tau) e^{-\frac{t+\Delta t-\tau}{\zeta_n}} D\dot{\epsilon}_{ve}(\tau) d\tau \\ &\quad - \sum_{n=1}^N \int_0^t E_n(\tau) e^{-\frac{t-\tau}{\zeta_n}} \left(1 - e^{-\frac{\Delta t}{\zeta_n}} \right) D\dot{\epsilon}_{ve}(\tau) d\tau \end{aligned} \quad (4.27)$$

and by recognising the state variable ${}^t\sigma_n$, eq. (3.28) in the last term

$$\begin{aligned} \Delta\sigma &= \int_t^{t+\Delta t} E_0(\tau) D\dot{\epsilon}_{ve}(\tau) d\tau + \sum_{n=1}^N \int_t^{t+\Delta t} E_n(\tau) e^{-\frac{t+\Delta t-\tau}{\zeta_n}} D\dot{\epsilon}_{ve}(\tau) d\tau \\ &\quad - \sum_{n=1}^N \left(1 - e^{-\frac{\Delta t}{\zeta_n}} \right) {}^t\sigma_n. \end{aligned} \quad (4.28)$$

The exponential nature of the integrand necessitates a higher-order numerical integration scheme for accurate calculation of the stress increment. However, the rate equations for plasticity can be integrated accurately by a linear scheme. It is therefore sensible, from a computational cost point of view, to reduce the creep equations further to a form which can be integrated with reasonable accuracy with a linear integration scheme. This is facilitated by assuming the strain rate to be constant over the time step:

$$\dot{\epsilon}_{ve} = \frac{\Delta\epsilon_{ve}}{\Delta t} \quad (4.29)$$

and the stiffness moduli $E_n(t^*)$ to be constant in the range $t \leq t^* \leq t + \Delta t$. Then (4.28) becomes

$$\Delta \sigma = E_0(t^*) D \Delta \epsilon_{ve} + \frac{1}{\Delta t} \sum_{n=1}^N \int_t^{t+\Delta t} E_n(\tau) e^{-\frac{t+\Delta t-\tau}{\zeta_n}} D d\tau \Delta \epsilon_{ve} - \sum_{n=1}^N \left(1 - e^{-\frac{\Delta t}{\zeta_n}} \right) {}^t \sigma_n \quad (4.30)$$

which can be integrated analytically to give

$$\Delta \sigma = D^{ve} \Delta \epsilon_{ve} + {}^t \tilde{\sigma} \quad (4.31)$$

with

$$D^{ve} = \left[E_0(t^*) + \sum_{n=1}^N \left(1 - e^{-\frac{\Delta t}{\zeta_n}} \right) \frac{E_n(t^*)}{\Delta t / \zeta_n} \right] D$$

$${}^t \tilde{\sigma} = - \sum_{n=1}^N \left(1 - e^{-\frac{\Delta t}{\zeta_n}} \right) {}^t \sigma_n. \quad (4.32)$$

The accuracy of the visco-elastic formulation above is determined by the assumption of the constant stiffnesses E_n of the individual springs and a constant strain rate (4.29) during each time increment. For non-aging material the first assumption is exact and, in the absence of cracks, the latter is reasonable. When cracks initiate or grow, the stress and strain rates can vary considerably, requiring small time steps to be taken for accurate time integration. Due to the sensitivity of the global solution at such stages this requirement is usually satisfied automatically in order to obtain a convergent solution.

4.2.4 INTEGRATION OF THE PLASTICITY CONSTITUTIVE EQUATION

The plasticity constitutive relation (3.46 and 3.49) can be integrated accurately with a linear scheme. To this end, the visco-elastic incremental stress given by eq. (4.31) can be supplemented to account for plastic flow, cf. (3.17), as

$$\Delta \sigma = D^{ve} \left(\Delta \epsilon - \Delta \epsilon_s - \Delta \epsilon_T - \Delta \lambda \frac{\partial g}{\partial \sigma} \right) + {}^t \tilde{\sigma}. \quad (4.33)$$

The current stress can be written as the incremental update

$${}^{t+\Delta t}\boldsymbol{\sigma} = {}^t\boldsymbol{\sigma} + \Delta\boldsymbol{\sigma} = {}^t\boldsymbol{\sigma} + \mathbf{D}^{ve} \left(\Delta\boldsymbol{\varepsilon} - \Delta\boldsymbol{\varepsilon}_s - \Delta\boldsymbol{\varepsilon}_T - \Delta\lambda \frac{\partial g}{\partial \boldsymbol{\sigma}} \right) + {}^t\tilde{\boldsymbol{\sigma}}. \quad (4.34)$$

Rewriting (4.33) in a standard plasticity predictor-corrector fashion and employing a fully implicit (Euler backward) integration scheme, the current stress becomes

$${}^{t+\Delta t}\boldsymbol{\sigma} = \mathbf{D}^s \left[\boldsymbol{\sigma}^{tr} - \mathbf{D}^{ve} \Delta\lambda \left(\frac{\partial g}{\partial \boldsymbol{\sigma}} \right) \right] \quad (4.35)$$

with, cf. eqs. (3.32, 3.34, 3.43)

$$\begin{aligned} \mathbf{D}^s &= [\mathbf{I} + \mathbf{D}^{ve} (\Delta\boldsymbol{\varepsilon}_{s,o} \mathbf{r}_s + \Delta\boldsymbol{\varepsilon}_{T,o} \mathbf{r}_T)]^{-1} \\ \boldsymbol{\sigma}^{tr} &= {}^t\boldsymbol{\sigma} + \mathbf{D}^{ve} (\Delta\boldsymbol{\varepsilon} - \Delta\boldsymbol{\varepsilon}_{s,o} \mathbf{P}_s - \Delta\boldsymbol{\varepsilon}_{T,o} \mathbf{P}_T) + {}^t\tilde{\boldsymbol{\sigma}}. \end{aligned} \quad (4.36)$$

Eq. (4.35) and the flow criterion (3.47) are written as a set of equations

$$\mathbf{F} = \begin{Bmatrix} {}^{t+\Delta t} \mathbf{F}_{\boldsymbol{\sigma}} \\ {}^{t+\Delta t} F_{\Delta\lambda} \end{Bmatrix} = \begin{Bmatrix} (\mathbf{D}^{ve})^{-1} \left[(\mathbf{D}^s)^{-1} {}^{t+\Delta t} \boldsymbol{\sigma} - \boldsymbol{\sigma}^{tr} \right] + \Delta\lambda \left(\frac{\partial g}{\partial \boldsymbol{\sigma}} \right) \\ {}^{t+\Delta t} f \end{Bmatrix} = 0 \quad (4.37)$$

which is solved for the stresses and plastic flow increment with a regular Newton Raphson iterative scheme

$$\begin{Bmatrix} {}^{t+\Delta t} \boldsymbol{\sigma} \\ \Delta\lambda \end{Bmatrix}_{i+1} = \begin{Bmatrix} {}^{t+\Delta t} \boldsymbol{\sigma} \\ \Delta\lambda \end{Bmatrix}_i - \mathbf{J}_i^{-1} \mathbf{F}. \quad (4.38)$$

The subscript i depicts the iteration number of this return-mapping scheme. The Jacobian is defined as:

$$\mathbf{J} = \begin{bmatrix} \frac{\partial \mathbf{F}_{\boldsymbol{\sigma}}}{\partial \boldsymbol{\sigma}} & \frac{\partial \mathbf{F}_{\boldsymbol{\sigma}}}{\partial \Delta\lambda} \\ \frac{\partial F_{\Delta\lambda}}{\partial \boldsymbol{\sigma}} & \frac{\partial F_{\Delta\lambda}}{\partial \Delta\lambda} \end{bmatrix}. \quad (4.39)$$

At convergence of this solution procedure the visco-elastic strain increment follows from

$$\Delta\boldsymbol{\varepsilon}_{ve} = \Delta\boldsymbol{\varepsilon} - \Delta\boldsymbol{\varepsilon}_s - \Delta\boldsymbol{\varepsilon}_T - \Delta\lambda \frac{\partial g}{\partial \boldsymbol{\sigma}} \quad (4.40)$$

enabling the state variables/internal stresses to be calculated from

$${}^{t+\Delta t}\boldsymbol{\sigma}_n = \begin{cases} {}^t\boldsymbol{\sigma}_n + D E_n(t^*) \Delta \boldsymbol{\epsilon}_{ve} & \text{for } n = 0 \\ {}^t\boldsymbol{\sigma}_n + \left[D \frac{E_n(t^*)}{\Delta t / \zeta_n} \Delta \boldsymbol{\epsilon}_{ve} - \boldsymbol{\sigma}_n \right] \left(1 - e^{-\frac{\Delta t}{\zeta_n}} \right) & \text{for } n = 1, 2, \dots, N. \end{cases} \quad (4.41)$$

For a Newton-Raphson incremental-iterative solution of the global set of nonlinear equations to be derived from eq. (4.23), a tangent stiffness matrix consistent with the return mapping algorithm is used, the importance of which was emphasised by Simo and Taylor (1985). Linearisation of eq. (4.37) gives

$$\mathbf{J} \begin{Bmatrix} d\boldsymbol{\sigma} \\ d\Delta\lambda \end{Bmatrix} = \begin{Bmatrix} d\boldsymbol{\epsilon} \\ 0 \end{Bmatrix}, \quad (4.42)$$

with \mathbf{J} the same Jacobian as for the stress-correction (4.39). The consistent tangent stiffness matrix is defined as

$$D^{vp} = \frac{d\boldsymbol{\sigma}}{d\boldsymbol{\epsilon}} \quad (4.43)$$

which, by condensation of eq. (4.42) reads

$$D^{vp} = \left[\frac{\partial \mathbf{F}_\sigma}{\partial \boldsymbol{\sigma}} - \frac{\partial \mathbf{F}_\sigma}{\partial \Delta\lambda} \left(\frac{\partial F_{\Delta\lambda}}{\partial \Delta\lambda} \right)^{-1} \frac{\partial F_{\Delta\lambda}}{\partial \boldsymbol{\sigma}} \right]^{-1}. \quad (4.44)$$

For the computation of the tangent operator $\frac{\partial F_{\Delta\lambda}}{\partial \Delta\lambda}$ must be non-singular. By ignoring the second term of eq. (4.44) this problem is avoided, while retaining a good approximation of the consistent tangent:

$$D^{vp} \approx \left(\frac{\partial \mathbf{F}_\sigma}{\partial \boldsymbol{\sigma}} \right)^{-1}. \quad (4.45)$$

The cracking rate dependence implied by the equation for cracking stress, eq. (3.56) and the yield function, eq. (3.47) is captured by the foregoing procedure and requires no further elaboration. The same linear integration employed for the rate law for viscoelasticity, section 4.2.3, and plasticity, section 4.2.4, implies that the rate term enters the yield function (4.37) in the incremental form:

$$\dot{\kappa} = \frac{\Delta \kappa}{\Delta t}. \quad (4.46)$$

4.2.5 INCREMENTAL-ITERATIVE SOLUTION PROCEDURE

The nonlinear, time-dependent equations are solved at discrete points in time to trace the evolution of stresses and strains. This leads to an incremental procedure, in which the time is incremented step-wise, indicated by superscripts combined with the time-dependent quantities

$$\begin{aligned} {}^{t+\Delta t}\boldsymbol{\epsilon} &= {}^t\boldsymbol{\epsilon} + \Delta\boldsymbol{\epsilon} \\ {}^{t+\Delta t}\boldsymbol{\sigma} &= {}^t\boldsymbol{\sigma} + \Delta\boldsymbol{\sigma} \\ {}^{t+\Delta t}\mathbf{r}_e &= {}^t\mathbf{r}_e + \Delta\mathbf{r}_e \end{aligned} \quad (4.47)$$

with \mathbf{r}_e the vector of all the external, nodal actions. For the solution at each time step an iterative solution procedure is employed, normally the regular Newton-Raphson method. The convergence iterations are denoted by the subscript j . The stress-update, eq. (4.47b), follows from the constitutive relation, eq. (4.34) which, upon linearisation, can be expressed as

$${}^{t+\Delta t}\boldsymbol{\sigma}_{j+1} = {}^{t+\Delta t}\boldsymbol{\sigma}_j + \mathbf{D}_j^{vp} (\mathrm{d}\boldsymbol{\epsilon} - \mathrm{d}\boldsymbol{\epsilon}_s - \mathrm{d}\boldsymbol{\epsilon}_T) + {}^t\tilde{\boldsymbol{\sigma}}. \quad (4.48)$$

By considering eq. (3.43), the current stress is given by

$${}^{t+\Delta t}\boldsymbol{\sigma}_{j+1} = \mathbf{D}_j^s \left[{}^{t+\Delta t}\boldsymbol{\sigma}_j + \mathbf{D}_j^{vp} (\mathrm{d}\boldsymbol{\epsilon} - \mathrm{d}\boldsymbol{\epsilon}_{s,o}\mathbf{P}_s - \mathrm{d}\boldsymbol{\epsilon}_{T,o}\mathbf{P}_T) + {}^t\tilde{\boldsymbol{\sigma}} \right], \quad (4.49)$$

with

$$\mathbf{D}_j^s = \left[\mathbf{I} + \mathbf{D}_j^{vp} (\mathrm{d}\boldsymbol{\epsilon}_{s,o}\mathbf{r}_s + \mathrm{d}\boldsymbol{\epsilon}_{T,o}\mathbf{r}_T) \right]^{-1}. \quad (4.50)$$

The equilibrium eq. (4.23) at time $t + \Delta t$ reads

$$\int_V \mathbf{B}^T {}^{t+\Delta t}\boldsymbol{\sigma}_{j+1} \mathrm{d}V = {}^{t+\Delta t}\mathbf{r}_e. \quad (4.51)$$

By substitution of the constitutive eq. (4.49) into the equilibrium eq. (4.51) and considering the linearised kinematic eq. (4.20)

$$\mathrm{d}\boldsymbol{\epsilon} = \mathbf{B} \mathrm{d}\mathbf{u}, \quad (4.52)$$

an expression for the vector of incremental displacement $\mathrm{d}\mathbf{u}_{j+1}$ is derived:

$$\begin{aligned} \mathbf{K}_j \mathrm{d}\mathbf{u}_{j+1} &= {}^{t+\Delta t}\mathbf{r}_e - \int_V \mathbf{B}^T \mathbf{D}_j^s {}^{t+\Delta t}\boldsymbol{\sigma}_j \mathrm{d}V + \\ &\quad \int_V \mathbf{B}^T \mathbf{D}_j^{ct} (\mathrm{d}\boldsymbol{\epsilon}_{s,o}\mathbf{P}_s + \mathrm{d}\boldsymbol{\epsilon}_{T,o}\mathbf{P}_T) \mathrm{d}V - \int_V \mathbf{B}^T \mathbf{D}_j^s {}^t\tilde{\boldsymbol{\sigma}} \mathrm{d}V, \end{aligned} \quad (4.53)$$

with

$$\begin{aligned} \mathbf{D}_j^{ct} &= \mathbf{D}_j^s \mathbf{D}_j^{vp} \\ \mathbf{K}_j &= \int_V \mathbf{B}^T \mathbf{D}_j^{ct} \mathbf{B} \, dV. \end{aligned} \quad (4.54)$$

Hereby, an iterative correction of the displacement increment vector is defined for the current time step as

$$\Delta \mathbf{u}_{j+1} = \Delta \mathbf{u}_j + d\mathbf{u}_{j+1}. \quad (4.55)$$

At the start of this algorithm ($j = 0$) the initial estimate of the displacement increment is given by, cf. eqs. (4.53,4.55)

$$\begin{aligned} \mathbf{K}_0 \Delta \mathbf{u}_1 &= {}^{t+\Delta t} \mathbf{r}_e - \int_V \mathbf{B}^T \mathbf{D}_0^s ({}^t \boldsymbol{\sigma} + {}^t \tilde{\boldsymbol{\sigma}}) \, dV + \\ &\quad \int_V \mathbf{B}^T \mathbf{D}_0^{ct} (\Delta \epsilon_{s,o} \mathbf{P}_s + \Delta \epsilon_{T,o} \mathbf{P}_T) \, dV. \end{aligned} \quad (4.56)$$

The subsequent iterations are driven by the unbalance in the equilibrium eq. (4.51)

$$\mathbf{K}_j d\mathbf{u}_{j+1} = {}^{t+\Delta t} \mathbf{r}_e - \int_V \mathbf{B}^T {}^{t+\Delta t} \boldsymbol{\sigma}_j \, dV. \quad (4.57)$$

This process is continued until equilibrium is achieved within an acceptable error. The consistent tangent modulus, eq. (4.54), ensures quadratic convergence to the equilibrium state.

4.2.6 ADAPTIVE TIME-STEPPING

An elegant way to trace the evolution of stresses and strains in quasi-static problems has been proposed by Van den Boogaard et al. (1994). It is similar to the arc-length methods for purely static cases, Riks (1972), Crisfield (1981), Ramm (1981). Hereby the need for interference by the analyst at sensitive stages of rapid crack growth or at limit points is reduced. Furthermore, as for the load increment in the standard arc-length method, the time increment can become negative. The physical interpretation of this phenomenon is that the problem becomes truly dynamic at this point. Inertia effects become significant. In this study inertia effects are not considered.

Unlike in the previous section, the time increment is not constant, but adaptable during the convergence iterations, denoted by

$$\Delta t_{j+1} = \Delta t_j + dt_{j+1} \quad (4.58)$$

similar to the iterative update of the displacement increment in eq. (4.55). As in the standard arc-length methods the external load vector is normalised with an adaptive load factor ρ_{j+1} , whereby eq. (4.51) becomes

$$\int_V \mathbf{B}^T \mathbf{\sigma}_{j+1} dV = \rho_{j+1} \mathbf{r}_e. \quad (4.59)$$

The stress and load factor at the end of the current time step ($t + \Delta t$) can be written in truncated Taylor series as

$$\begin{aligned} \mathbf{\sigma}_{j+1} &= \mathbf{\sigma}_j + \mathbf{D}^{ct} d\mathbf{\epsilon}_{j+1} + \mathbf{D}' dt_{j+1} \\ \rho_{j+1} &= \rho_j + \dot{\rho}_j dt_{j+1} \end{aligned} \quad (4.60)$$

where \mathbf{D}^{ct} is the consistent tangent modulus of the previous section, eq. (4.54a) and

$$\mathbf{D}' = \frac{\partial \Delta \mathbf{\sigma}}{\partial \Delta t}. \quad (4.61)$$

By substituting eq. (4.60) into the equilibrium equation and considering the kinematic relation eq. (4.52), an expression for the iterative displacement update is obtained as

$$\mathbf{K}_j d\mathbf{u}_{j+1} = \rho_j \mathbf{r}_e - \int_V \mathbf{B}^T \mathbf{\sigma}_j dV + dt_{j+1} \left(\dot{\rho}_j \mathbf{r}_e - \int_V \mathbf{B}^T \mathbf{D}'_j dV \right). \quad (4.62)$$

By defining

$$\begin{aligned} \mathbf{p}_j &= \rho_j \mathbf{r}_e - \int_V \mathbf{B}^T \mathbf{\sigma}_j dV - \Delta t_j \left(\dot{\rho}_j \mathbf{r}_e - \int_V \mathbf{B}^T \mathbf{D}'_j dV \right) \\ \mathbf{q}_j &= \dot{\rho}_j \mathbf{r}_e - \int_V \mathbf{B}^T \mathbf{D}'_j dV \end{aligned} \quad (4.63)$$

eq. (4.62) becomes

$$\mathbf{K}_j d\mathbf{u}_{j+1} = \mathbf{p}_j + \Delta t_{j+1} \mathbf{q}_j. \quad (4.64)$$

For the solution of the variable time step from this equation, the displacement increment is constrained to remain constant in the time by some norm. Here the linearised version of the L_2 norm of the displacement vector

$$\Delta \mathbf{u}_j^T d\mathbf{u}_{j+1} = 0 \quad (4.65)$$

is employed, which, upon combination with eq. (4.64) renders the time increment

$$\Delta t_{j+1} = - \frac{\Delta \mathbf{u}_j^T \mathbf{K}_j^{-1} \mathbf{p}_j}{\Delta \mathbf{u}_j^T \mathbf{K}_j^{-1} \mathbf{q}_j}. \quad (4.66)$$

To evaluate the stress increment time derivative \mathbf{D}^t , we write the stress increment cf. eqs. (4.47b), (4.49) and (4.50) as

$$\Delta \boldsymbol{\sigma} = \mathbf{D}^s (\mathbf{D}^{vp} \Delta \bar{\boldsymbol{\epsilon}} + {}^t \tilde{\boldsymbol{\sigma}}) \quad (4.67)$$

with

$$\Delta \bar{\boldsymbol{\epsilon}} = \Delta \boldsymbol{\epsilon} - \Delta \epsilon_{s,o} (\mathbf{P}_s + \mathbf{r}_s {}^t \boldsymbol{\sigma}) - \Delta \epsilon_{T,o} (\mathbf{P}_T + \mathbf{r}_T {}^t \boldsymbol{\sigma}). \quad (4.68)$$

Partial differentiation with respect to the time increment produces

$$\mathbf{D}^t = \frac{\partial \Delta \boldsymbol{\sigma}}{\partial \Delta t} = \frac{\partial \mathbf{D}^s}{\partial \Delta t} (\mathbf{D}^{vp} \Delta \bar{\boldsymbol{\epsilon}} + {}^t \tilde{\boldsymbol{\sigma}}) + \mathbf{D}^s \left(\frac{\partial \mathbf{D}^{vp}}{\partial \Delta t} \Delta \bar{\boldsymbol{\epsilon}} + \mathbf{D}^{vp} \frac{\partial \Delta \bar{\boldsymbol{\epsilon}}}{\partial \Delta t} + \frac{\partial {}^t \tilde{\boldsymbol{\sigma}}}{\partial \Delta t} \right) \quad (4.69)$$

with

$$\begin{aligned} \frac{\partial \mathbf{D}^s}{\partial \Delta t} &= -\mathbf{D}^s \frac{\partial}{\partial \Delta t} [(\mathbf{D}^s)^{-1}] \mathbf{D}^s \\ \frac{\partial}{\partial \Delta t} [(\mathbf{D}^s)^{-1}] &= \frac{\partial \mathbf{D}^{vp}}{\partial \Delta t} (\Delta \epsilon_{s,o} \mathbf{r}_s + \Delta \epsilon_{T,o} \mathbf{r}_T) + \mathbf{D}^{vp} \left(\frac{\partial \Delta \epsilon_{s,o}}{\partial \Delta t} \mathbf{r}_s + \frac{\partial \Delta \epsilon_{T,o}}{\partial \Delta t} \mathbf{r}_T \right) \\ \frac{\partial \Delta \bar{\boldsymbol{\epsilon}}}{\partial \Delta t} &= - \left(\frac{\partial \Delta \epsilon_{s,o}}{\partial \Delta t} \mathbf{P}_s + \frac{\partial \Delta \epsilon_{T,o}}{\partial \Delta t} \mathbf{P}_T \right) \\ \frac{\partial \Delta \epsilon_{s,o}}{\partial \Delta t} &= \alpha_s \frac{\partial \Delta h}{\partial \Delta t} \\ \frac{\partial \Delta \epsilon_{T,o}}{\partial \Delta t} &= \alpha_T \frac{\partial \Delta T}{\partial \Delta t} \\ \frac{\partial {}^t \tilde{\boldsymbol{\sigma}}}{\partial \Delta t} &= - \sum_{n=1}^N \frac{1}{\zeta_n} e^{-\Delta t / \zeta_n} {}^t \boldsymbol{\sigma}_n. \end{aligned} \quad (4.70)$$

The time derivative of the elasto-plastic consistent tangent stiffness modulus $\frac{\partial \mathbf{D}^{vp}}{\partial \Delta t}$ depends on the particular yield criterion employed and will be derived after elaboration thereof.

4.3 Finite element interpolation order

For the mechanical analysis, a displacement interpolation polynomial of one order higher than for the pore humidities in the hygral analysis (or temperatures in a thermal analysis) is needed to avoid oscillating stress fields. This is illustrated in Figure 4.1 for a one-dimensional, restrained, shrinking bar. The linear shrinkage field (ϵ_s) shown in the figure

can be represented by the two two-noded elements. However, by subsequently employing the same, linear interpolation order for the displacement field, a piece-wise constant total strain field (ϵ) is found, following from the kinematic equation. In the absence of cracking, the elastic strain is the difference between the total and shrinkage strain ($\epsilon_e = \epsilon - \epsilon_s$). Because the two terms on the right hand side are not of equal order, an oscillating elastic strain field and, therefore, stress field is found instead of a constant stress which satisfies equilibrium at each point in the bar.

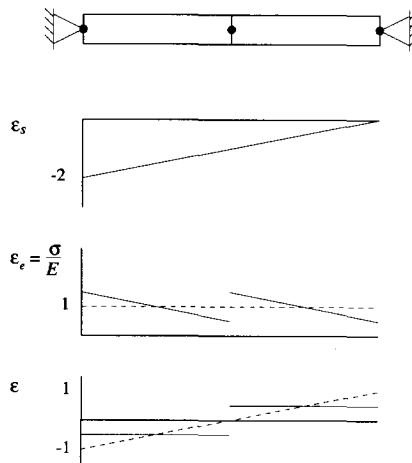


Figure 4.1: One-dimensional, restrained, shrinking bar, exhibiting oscillating stresses in case of equal-order interpolation of pore humidity and displacement fields.

This phenomenon is less pronounced in a multi-dimensional analysis, because then equal-order interpolation of the pore humidity and the displacements produces compatible shrinkage and total strain component fields in the orthogonal directions. For instance, the normal strain component ϵ_x is constant in the x -direction, but linear in the orthogonal directions when employing linear displacement interpolation.

Chapter 5

CRACK MODELLING STRATEGIES

As suggested by the features of masonry cracking in section 2.4, two alternative modelling approaches can be followed to model cracks in masonry, namely discrete or continuum modelling (eg. Rots 1994, Lourenço 1996). Here discrete modelling does not refer to the discretisation of the microstructure of a cementitious material, but rather to the way in which cracks are modelled. The general mathematical and numerical frameworks for the plasticity formulation, which is adopted here for capturing the crack initiation and growth, have been discussed in Chapters 3 and 4. In this chapter the particular choices of crack initiation criteria, which depend on the modelling strategy, are made and elaborated in the context of the numerical setting. Whereas the crack modelling strategies were verified and validated by Lourenço (1996), the enhancements made here to the interface model with respect to the dilatancy formulation and the stress-enhanced shear fracture energy, are validated. Subsequently, the extension of the interface model to three dimensions is described. Finally, the continuum approach is discussed and the regularisation of the crack localisation by the crack rate dependence is demonstrated by a simple example.

5.1 Discrete modelling

With the knowledge that the masonry joints are the weak link, they are modelled with interface elements, which capture debonding, shear-slipping and crushing between the two constituent phases in a discrete/discontinuous way, Figure 5.1a. The brick and mortar are discretised with continuous elements. This strategy can be simplified by discretising only the bricks, while interface elements account for the joint actions, Figure 5.1b. In some cases it is necessary to supplement the modelling strategy to include the cracking in the bricks. It usually suffices to model central, vertical brick cracks, by placing interfaces at these locations, Figure 5.1a,b. Furthermore, the creep, as well as the hygral and thermal shrinkage act on the continuum.

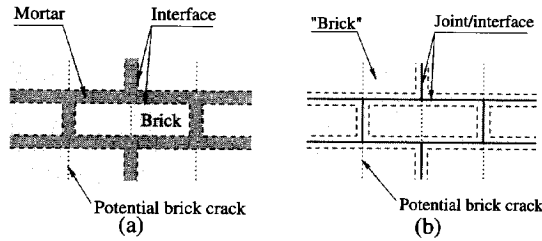


Figure 5.1: (a) A discrete modelling strategy and (b) a simplified discrete modelling strategy for masonry.

5.1.1 AN INTERFACE MODEL FOR 2-D MASONRY DISCRETE MODELLING

A plane stress interface model was formulated by Lourenço (1996). It is based on multi-surface plasticity, comprising a Coulomb friction model combined with a tension cut-off and an elliptical compression cap, Figure 5.2. Softening acts in all three modes and is preceded by hardening in the case of the cap mode. The model is described in detail by Lourenço (1996). This model is enhanced here to allow for the apparent stress dependence of the shear fracture energy, as found experimentally by Van der Pluijm (1992), Figure 2.15a, as well as to capture the observed dilatant behaviour of masonry joints, Figure 2.15b. This dilatancy, if confined externally, or by the surrounding masonry, contributes significantly to the strength and toughness of masonry and may determine the failure mode.

The tension cut-off and compression cap formulations by Lourenço remain unaltered, but the shear mode and its intersections with the former two modes are modified. To sketch a clear picture of the modifications to the model, the shear mode is elaborated in detail.

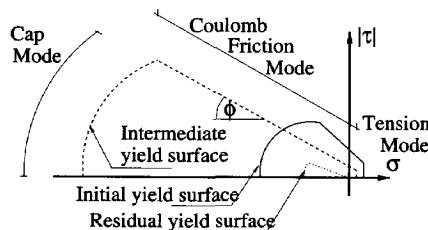


Figure 5.2: Interface model (Lourenço 1996).

The interface model is derived in terms of the generalised stress and strain vectors:

$$\begin{aligned}\boldsymbol{\sigma} &= \{ \sigma \ \tau \}^T \\ \boldsymbol{\varepsilon} &= \{ u \ v \}^T,\end{aligned}\quad (5.1)$$

with σ and u the stress and relative displacement respectively in the interface normal direction and τ and v the shear stress and relative displacement respectively. In the elastic regime the constitutive behaviour is described by

$$\boldsymbol{\sigma} = \mathbf{D}\boldsymbol{\varepsilon}, \quad (5.2)$$

with the stiffness matrix

$$\mathbf{D} = \text{diag} [k_n \ k_s]. \quad (5.3)$$

A Coulomb-friction yield/crack initiation criterion is an obvious choice, Figure 2.14. Thereby, shear-slipping occurs if the yield function

$$f = |\tau| + \sigma \Phi - c \quad (5.4)$$

becomes zero. Both adhesion softening and friction softening are apparent in Figure 2.14. The adhesion softening is described by

$$c(\sigma, \kappa) = c_o e^{-\frac{c_o}{G_f^H} \kappa}, \quad (5.5)$$

where c_o is the initial adhesion of the brick-mortar interface and G_f^H the shear-slip fracture energy. The friction softening is coupled to the adhesion softening via

$$\Phi(\sigma, \kappa) = \tan \phi_o + (\tan \phi_r - \tan \phi_o) \frac{c_o - c}{c_o}, \quad (5.6)$$

with ϕ_o the initial and ϕ_r the residual friction angle. The adhesion and friction parameters are found by linear regression of the micro-shear experimental data, Figure 2.14, while the fracture energy is determined by the appropriate integration of the stress-crack width response. Note that this integration produces the total energy dissipated by both the adhesion and the friction softening, which amounts to

$$G_f^{H*} = G_f^H \left[1 + \frac{\sigma}{c_o} (\tan \phi_r - \tan \phi_o) \right]. \quad (5.7)$$

The experimentally observed linear relation between the fracture energy and the normal confining stress, Figure 2.15a, is captured by letting

$$G_f^H = \begin{cases} a\sigma + b, & \sigma < 0 \\ b, & \sigma \geq 0 \end{cases} \quad (5.8)$$

with a and b constants to be determined by linear regression of the experimental data. If the contribution of the friction softening energy is significant, which is revealed upon evaluation of the second term between the square brackets of eq. (5.7), the regressed coefficients a and b should be adjusted to avoid a too high energy dissipation at high compressive stresses.

The flow rule

$$\dot{\boldsymbol{\epsilon}}_p = \left\{ \begin{array}{c} \dot{u}_p \\ \dot{v}_p \end{array} \right\} = \dot{\lambda} \frac{\partial g}{\partial \boldsymbol{\sigma}} \quad (5.9)$$

provides a way of describing the dilatancy, by choice of a suitable potential function

$$\frac{\partial g}{\partial \boldsymbol{\sigma}} = \left\{ \begin{array}{c} \Psi \\ \text{sign}(\tau) \end{array} \right\}, \quad (5.10)$$

$\Psi = \tan \psi$ being the mobilised dilatancy coefficient. Following directly from the flow rule

$$\Psi = \frac{\dot{u}_p}{\dot{v}_p} \text{sign}(\tau). \quad (5.11)$$

By integration the shear-slip induced normal uplift is found to be:

$$u_p = \int \Psi \, d|\Delta v_p|. \quad (5.12)$$

There is experimental evidence, Figure 2.15b, that dilatancy is dependent on the confining stress and the shear-slip. A dilatancy formulation of separate variables, i.e.

$$\Psi = \Psi_1(\sigma) \Psi_2(v_p) \quad (5.13)$$

simplifies curve fitting and ensures convexity of the potential function g :

$$g = \int \left(\frac{\partial g}{\partial \boldsymbol{\sigma}} \right)^T d\boldsymbol{\sigma} = |\tau| + \Psi_2(v_p) \int \Psi_1(\sigma) d\sigma. \quad (5.14)$$

Therefore, a description of the normal uplift upon shear-slipping is chosen as

$$u_p = \begin{cases} 0, & \sigma < \sigma_u \\ \frac{\tan \psi_o}{\delta} \left(1 - \frac{\sigma}{\sigma_u} \right) (1 - e^{-\delta v_p}), & \sigma_u \leq \sigma < 0 \\ \frac{\tan \psi_o}{\delta} (1 - e^{-\delta v_p}), & \sigma \geq 0, \end{cases} \quad (5.15)$$

which yields after differentiation

$$\Psi = \begin{cases} 0, & \sigma < \sigma_u \\ \tan \psi_o \left[1 - \frac{\sigma}{\sigma_u} \right] e^{-\delta v_p}, & \sigma_u \leq \sigma < 0 \\ \tan \psi_o e^{-\delta v_p}, & \sigma \geq 0. \end{cases} \quad (5.16)$$

The dilatancy at zero normal confining stress and shear slip ($\tan \psi_o$), confining (compressive) stress at which the dilatancy becomes zero (σ_u) and the dilatancy shear slip degradation coefficient (δ) are material parameters to be obtained by, for instance, a least squares fit of eq. (5.15) to experimental test data. Note that for tensile stress a stress-independent dilatancy coefficient is assumed.

The above relations are cast into the standard plasticity formulation next. A strain softening hypothesis is employed, where the softening is governed by shear-slipping, yielding

$$\Delta \kappa = |\Delta v_p| = \Delta \lambda \quad (5.17)$$

upon substitution of eqs. (5.9, 5.10). The stress-update, eq. 4.35, is here given by

$${}^{t+\Delta t} \boldsymbol{\sigma} = {}^t \boldsymbol{\sigma} + \mathbf{D} \left[\Delta \boldsymbol{\varepsilon} - \Delta \lambda \frac{{}^{t+\Delta t} \partial g}{\partial \boldsymbol{\sigma}} \right], \quad (5.18)$$

which reduces to

$${}^{t+\Delta t} \begin{Bmatrix} \sigma \\ \tau \end{Bmatrix} = \begin{Bmatrix} \sigma^{tr} - k_n \Delta \lambda \frac{{}^{t+\Delta t} \Psi}{\partial \sigma} \\ \tau^{tr} - k_s \Delta \lambda \text{sign}({}^{t+\Delta t} \tau) \end{Bmatrix} \quad (5.19)$$

in the standard plasticity predictor-corrector fashion, with the trial stresses defined as

$$\begin{Bmatrix} \sigma^{tr} \\ \tau^{tr} \end{Bmatrix} = \begin{Bmatrix} {}^t \sigma + k_n \Delta u \\ {}^t \tau + k_s \Delta v \end{Bmatrix}. \quad (5.20)$$

The remaining updating equations are:

$$\begin{aligned} {}^{t+\Delta t} \kappa &= {}^t \kappa + \Delta \kappa \\ {}^{t+\Delta t} f &= 0. \end{aligned} \quad (5.21)$$

By substitution of the stress and plastic strain-update eqs. (5.19, 5.21a) into the yield criterion (5.21b), a single, nonlinear equation with one independent variable $\Delta \lambda$ is produced. A Newton-Raphson iterative scheme is employed to find the solution:

$$\Delta \lambda_{i+1} = \Delta \lambda_i - \frac{{}^{t+\Delta t} \left[\left(\frac{df}{d\Delta \lambda} \right)^{-1} f \right]_i}{f_i}. \quad (5.22)$$

The derivation of the Jacobian $\left[\frac{d\epsilon}{d\Delta\lambda}\right]$ is elaborated by Van Zijl (1999a).

The consistent tangent stiffness modulus is given by

$$D^{ep} = \frac{\partial \sigma}{\partial \epsilon} = H^{-1} - \frac{H^{-1} \gamma \eta^T H^{-1}}{\eta^T H^{-1} \gamma - h} \quad (5.23)$$

with

$$\begin{aligned} H &= D^{-1} + \Delta\lambda \frac{\partial^2 g}{\partial \sigma^2} \\ \eta &= \frac{\partial f}{\partial \sigma} \\ \gamma &= \frac{\partial g}{\partial \sigma} + \Delta\lambda \frac{\partial^2 g}{\partial \kappa \partial \sigma} \\ h &= \left(\frac{\partial f}{\partial \Phi} \frac{\partial \Phi}{\partial c} + \frac{\partial f}{\partial c} \right) \frac{\partial c}{\partial \kappa}. \end{aligned} \quad (5.24)$$

See Van Zijl (1999a) for the detailed elaboration of all the derivatives above.

At each of the intersections of the Coulomb-friction criterion with the tension cut-off and compression cap the plastic strain increment is, cf. eq. (3.53)

$$\Delta \epsilon_p = \Delta \lambda_1 \frac{\partial g_1}{\partial \sigma} + \Delta \lambda_2 \frac{\partial g_2}{\partial \sigma} \quad (5.25)$$

where the subscripts 1 and 2 refer to the two intersecting criteria. Lourenço (1996) describes this procedure in detail. Here only the main features of the two corners are outlined.

The yield function for the tension cut-off (criterion number 2 of the interface model) is:

$$f_2 = \sigma - \sigma_t \quad (5.26)$$

with σ_t the tensile, or brick-mortar bond strength. The strength is assumed to soften exponentially

$$\sigma_t = f_t e^{-\frac{f_t}{G_f^I} \kappa_2} \quad (5.27)$$

with f_t the bond strength and G_f^I the mode I fracture energy. The softening is governed by a strain softening hypothesis:

$$\Delta \kappa_2 = |\Delta u_p| \quad (5.28)$$

which, upon consideration of an associated flow rule

$$\Delta \epsilon_p = \Delta \lambda_2 \frac{\partial f_2}{\partial \sigma}, \quad (5.29)$$

reduces to

$$\Delta \kappa_2 = \Delta \lambda_2. \quad (5.30)$$

In the shear/tension corner the stress corrections can be written as

$${}^{t+\Delta t} \begin{Bmatrix} \sigma \\ \tau \end{Bmatrix} = \begin{Bmatrix} \sigma^{tr} - k_n \Delta \lambda_1 {}^{t+\Delta t} \Psi - k_n \Delta \lambda_2 \\ \tau^{tr} - k_s \Delta \lambda_1 \end{Bmatrix} \quad (5.31)$$

where the trial stresses are as defined before in eq. (5.20). Upon substitution of these stress corrections into the yield functions (5.4) and (5.26), a set of two coupled, nonlinear equations arises, to be solved for the two plastic flow increments in an iterative Newton-Raphson algorithm as follows:

$$\begin{Bmatrix} \Delta \lambda_1 \\ \Delta \lambda_2 \end{Bmatrix}_{i+1} = \begin{Bmatrix} \Delta \lambda_1 \\ \Delta \lambda_2 \end{Bmatrix}_i - \begin{bmatrix} \frac{\partial f_1}{\partial \Delta \lambda_1} & \frac{\partial f_1}{\partial \Delta \lambda_2} \\ \frac{\partial f_2}{\partial \Delta \lambda_1} & \frac{\partial f_2}{\partial \Delta \lambda_2} \end{bmatrix}_i^{-1} {}^{t+\Delta t} \begin{Bmatrix} f_1 \\ f_2 \end{Bmatrix}_i. \quad (5.32)$$

The Jacobian above is elaborated in Van Zijl (1999a) along with the consistent tangent modulus for this corner regime.

The yield function for the compression cap (here referred to as criterion number 3, ₁ being the shear mode) is

$$f_3 = \sigma^2 + C_s \tau^2 - \sigma_c^2 \quad (5.33)$$

with C_s a parameter controlling the shear stress contribution to failure and σ_c the compressive strength. The latter is assumed to evolve according to the strain hardening hypothesis:

$$\Delta \kappa_3 = \sqrt{\Delta \epsilon_p^T \Delta \epsilon_p} \quad (5.34)$$

which, upon consideration of an associated flow rule

$$\Delta \epsilon_p = \Delta \lambda_3 \frac{\partial f_3}{\partial \sigma}, \quad (5.35)$$

becomes

$$\Delta\kappa_3 = 2 \Delta\lambda_3 \sqrt{\sigma^2 + (C_s \tau)^2}. \quad (5.36)$$

In the shear/compression corner the stress-corrections can be written as

$${}^{t+\Delta t} \begin{Bmatrix} \sigma \\ \tau \end{Bmatrix} = \begin{Bmatrix} \sigma^{tr} - k_n \Delta\lambda_1 {}^{t+\Delta t} \Psi - 2 k_n \Delta\lambda_3 {}^{t+\Delta t} \sigma \\ \tau^{tr} - k_s \Delta\lambda_1 - 2 k_s C_s \Delta\lambda_3 {}^{t+\Delta t} \tau \end{Bmatrix} \quad (5.37)$$

where the trial stresses are as defined before in eq. (5.20). Upon substitution of these stress-corrections into the yield functions (5.4) and (5.33), a set of two coupled, nonlinear equations arises. It is solved for the two plastic flow increments in an iterative Newton-Raphson algorithm as follows:

$$\begin{Bmatrix} \Delta\lambda_1 \\ \Delta\lambda_3 \end{Bmatrix}_{i+1} = \begin{Bmatrix} \Delta\lambda_1 \\ \Delta\lambda_3 \end{Bmatrix}_i - \begin{bmatrix} \frac{\partial f_1}{\partial \Delta\lambda_1} & \frac{\partial f_1}{\partial \Delta\lambda_3} \\ \frac{\partial f_3}{\partial \Delta\lambda_1} & \frac{\partial f_3}{\partial \Delta\lambda_3} \end{bmatrix}_i^{-1} {}^{t+\Delta t} \begin{Bmatrix} f_1 \\ f_3 \end{Bmatrix}_i. \quad (5.38)$$

The Jacobian above is elaborated in Van Zijl (1999a) along with the consistent tangent modulus for this corner regime.

5.1.2 VERIFICATION AND VALIDATION OF DISCRETE APPROACH

The discrete modelling approach has been verified and validated by numerical analyses (Lourenço 1996, Van Zijl 1996, Van Zijl et al. 1997) of micro-experiments performed by Van der Pluijm and Vermeltfoort (1991) and Van der Pluijm (1992) and meso-scale experiments on small masonry walls (Backes 1985, Vermeltfoort and Raijmakers 1993).

It should be noted that the clear distinction between mode I and II failure suggested by the tension cut-off of the Coulomb-friction criterion is an approximation of the real behaviour. The objective characterisation of the apex regime is virtually impossible due to stress nonuniformity in even the most carefully planned experimental set-up. For example, for normal tension and even for low normal compression in a specimen tested in the Van der Pluijm micro-shear test, Figure 2.14, mixed-mode failure may occur. The proposed material model thus presents a failure envelope which may, in some cases, predict the mode of failure incorrectly.

In this section the dilatant normal uplift upon shear and its influence on the masonry behaviour if it is constrained, are investigated. Van der Pluijm (1992,1998) performed a

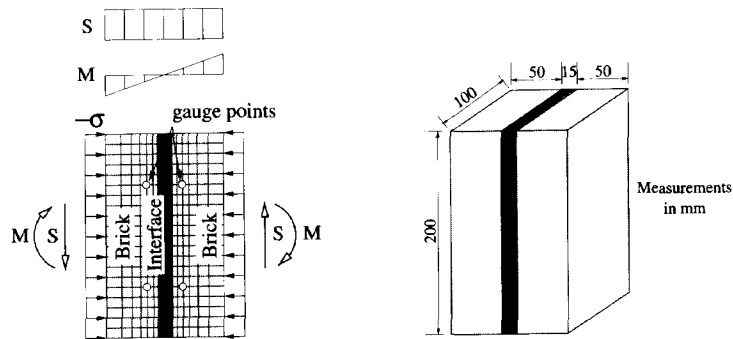


Figure 5.3: Schematic set-up of masonry shear tests (Van der Pluijm 1992, 1998).

	k_n $\frac{N}{mm^3}$	k_s $\frac{N}{mm^3}$	f_t $\frac{N}{mm^2}$	G_f^I $\frac{N}{mm}$	c_o $\frac{N}{mm^2}$	G_f^{II} $\frac{N}{mm}$	$\tan \phi_o$	$\tan \phi_r$	$\tan \psi_o$	σ_u $\frac{N}{mm^2}$	δ
(a)	825	345	0.4	0.012	0.87	$0.006 - 0.09\sigma$	1.1	0.70	0.74	-1.57	5.6
(b)	438	182	0.1	0.005	0.28	$0.02 - 0.03\sigma$	0.97	0.75	0.67	-1.22	17

Table 5.1: Parameters employed for the joint/interface in the (a) clay brick and (b) calcium silicate specimens.

series of shear tests on small masonry specimens, each containing a single joint. In the first part of the experimental program a constant confining pressure was maintained on the specimens, Figure 5.3. Typical results of these tests have been shown in section 2.4. By regression of these results, the model parameters have been obtained for a typical clay brick masonry and a calcium silicate masonry, Table 5.1. The tensile strength and fracture energy are exceptions. They are average values obtained from separate displacement-controlled tension tests of the respective masonry types (Van der Pluijm and Vermeltfoort 1991, Van der Pluijm 1998). Also, the employed Young's moduli $E = 17400$ and $E = 13400$ for the clay brick and calcium silicate unit respectively, as well as a Poisson's ratio $\nu = 0.2$ for both, are reported average values. The interface stiffnesses k_n , k_s have been calculated to match the observed initial elastic responses of the masonry shear specimens.

Figure 5.3 also shows the finite element mesh used for the analyses. Note that the simplified discrete analysis strategy, Figure 5.1b, is followed. The plane stress interface model outlined in the previous section is employed. This strategy has been shown to simulate the shear stress-deformational response accurately (Van Zijl 1996). Also, the normal uplift upon the shearing displacement along the joint for this experimental set-up, where a constant confining pressure is maintained, has been verified (Van Zijl et al. 1997). The

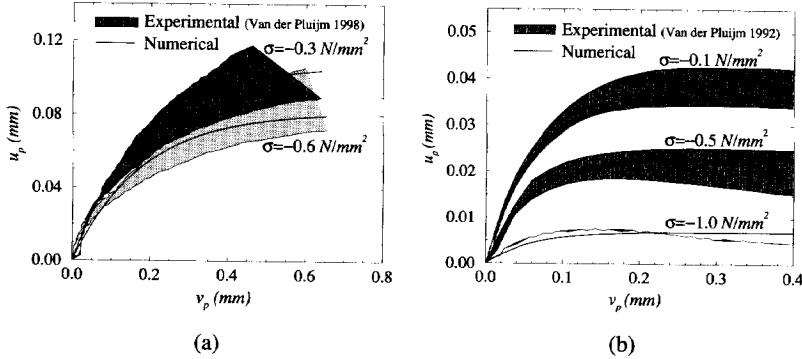


Figure 5.4: Comparison of the measured (Van der Pluijm 1992, 1998) and numerical dilatant normal displacement upon shear displacement of a (a) clay brick masonry and a (b) calcium silicate masonry.

experimental and numerical dilatancy responses are compared in Figure 5.4 for the two types of masonry investigated. Note that the joint normal and shear displacements are shown, which are calculated from the measurements at the gauge points and the elastic properties of the bricks (Van der Pluijm 1992). The agreement is not surprising, because the model parameters have been calculated from these experimental responses. Nevertheless, it shows that the chosen form of the dilatancy equation is appropriate.

A more severe test of the model is presented by the confinement of the dilatancy and the associated normal stress build-up. Van der Pluijm (1998) modified his experimental set-up to control the displacement normal to the joint. He performed shear tests on two specimens of the clay brick masonry type, Table 5.1. In the first test he applied an initial normal displacement to cause an average stress of -0.1 N/mm^2 . The normal boundaries were then fixed in this position, before the displacement-controlled shearing was commenced, as shown schematically in Figure 5.5a. The same procedure was followed for the second test, except that an initial average tensile stress, $\sigma_0 = +0.1 \text{ N/mm}^2$ was applied instead of the compression in the first test. In Figure 5.5b the normal force build-up upon shearing is shown. Van der Pluijm limited the normal force to 27.5 kN to protect the test apparatus, at which point he switched back to force control of the normal boundary to sustain the limit force. This has been simulated numerically, Figure 5.5b. However, the case of unrestricted normal force build-up has also been analysed. These numerical responses are shown in dotted lines. Due to the smoothing of the interface, a point is reached where no further dilatancy occurs and the normal force is arrested. This point coincides with the pressure at which the dilatancy becomes zero σ_u . The measured response

for the case of initial compression ($\sigma_0 = -0.1 \text{ N/mm}^2$) indicates that a limit point was approached just before the switch to force control was made, which confirms the numerical result. In Figure 5.5c the numerical and experimental shear force-deformation responses are compared. Reasonable agreement is found.

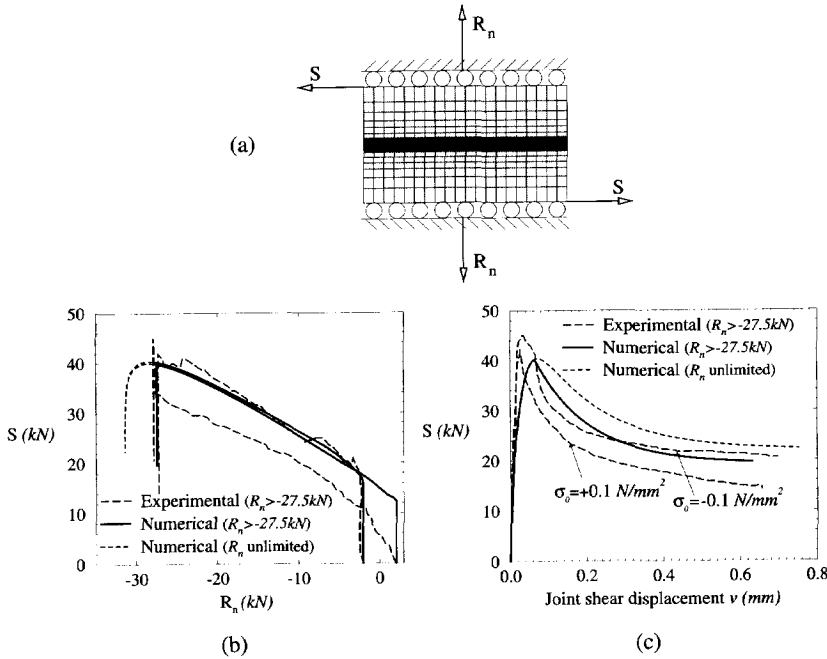


Figure 5.5: (a) Schematic set-up of the normal confined masonry shear tests (Van der Pluijm 1998). Comparison of experimental and numerical (b) shear force vs. normal reaction force and (c) shear force vs. joint shear displacement.

Whereas the agreement of the numerical responses with the measured responses is reasonable, the inappropriate dilatancy modelling can lead to large errors. This is illustrated in Figure 5.6. For even a small, constant dilatancy coefficient an unlimited strength is predicted for the shear specimen of Figure 5.5a. A dilatancy coefficient of zero reproduces the response under force control of the normal boundaries, Figure 5.3, in which case the initial confining pressure governs the response. The responses for $\sigma_o = -0.1 \text{ N/mm}^2$ are shown.

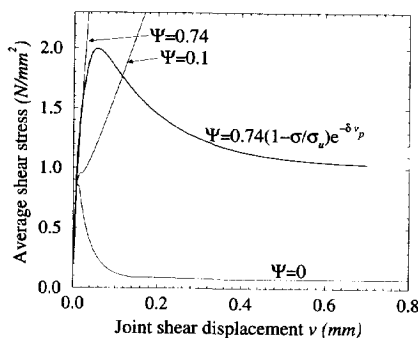


Figure 5.6: The response to inappropriate dilatancy modelling.

5.1.3 EXTENSION TO PLANE INTERFACE BEHAVIOUR FOR 3-D DISCRETE ANALYSIS

The two-dimensional interface model can be extended to a three-dimensional interface, which describes the delamination and relative shear-slipping of two planes. Now the generalised stress and strain vectors are:

$$\begin{aligned} \boldsymbol{\sigma} &= \{ \sigma \ \tau_s \ \tau_t \}^T \\ \boldsymbol{\epsilon} &= \{ u \ v \ w \}^T, \end{aligned} \quad (5.39)$$

where the shear stresses τ_s and τ_t act in the local plane of the interface, v and w are the relative shearing displacements in the interface plane and σ and u the stress and relative displacement respectively normal to the plane. The stiffness matrix is defined as

$$\mathbf{D} = \text{diag} [k_n \ k_s \ k_t]. \quad (5.40)$$

Here a tension cut-off and a Coulomb-friction yield criterion are combined, Figure 5.7. Apart from the added stress and strain component, the two-dimensional tension criterion

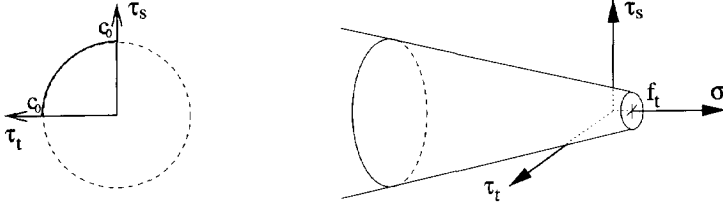


Figure 5.7: Three-dimensional interface yield function.

f_2 of section 5.1.1 remains unchanged. For the Coulomb-friction part the yield function becomes:

$$f = \sqrt{\tau_s^2 + \tau_t^2} + \sigma \Phi - c. \quad (5.41)$$

As for the two-dimensional case adhesion softening and friction softening is modelled as described by eqs. (5.5,5.6). A non-associated plastic potential is chosen, giving the flow rule

$$\Delta \epsilon_p = \Delta \lambda \frac{\partial g}{\partial \sigma} = \Delta \lambda \left\{ \begin{array}{c} \frac{\Psi}{\sqrt{\tau_s^2 + \tau_t^2}} \\ \frac{\tau_t}{\sqrt{\tau_s^2 + \tau_t^2}} \end{array} \right\}, \quad (5.42)$$

with the mobilised dilatancy Ψ defined as before by eq. (5.16). However, now the strain softening is governed by the equivalent shear displacement

$$\Delta \kappa = \sqrt{(\Delta v_p)^2 + (\Delta w_p)^2} = \Delta \lambda. \quad (5.43)$$

The stress corrections can be written as:

$${}^{t+\Delta t} \sigma = {}^t \sigma + D \left[\Delta \epsilon - \Delta \lambda {}^{t+\Delta t} \frac{\partial g}{\partial \sigma} \right] = \left\{ \begin{array}{c} \sigma^{tr} - k_n \Delta \lambda {}^{t+\Delta t} \Psi \\ \tau_s^{tr} - k_s \Delta \lambda {}^{t+\Delta t} \left(\frac{\tau_s}{\sqrt{\tau_s^2 + \tau_t^2}} \right) \\ \tau_t^{tr} - k_t \Delta \lambda {}^{t+\Delta t} \left(\frac{\tau_t}{\sqrt{\tau_s^2 + \tau_t^2}} \right) \end{array} \right\}. \quad (5.44)$$

By substituting these stress-updating equations into the yield function and assuming the same shearing stiffnesses in orthogonal directions ($k_s = k_t$), a single equation with unknown $\Delta \lambda$ can be derived

$${}^{t+\Delta t} f = 0 = \sqrt{(\tau_s^{tr})^2 + (\tau_t^{tr})^2} - k_s \Delta \lambda + {}^{t+\Delta t} [\sigma \Phi(\sigma, \Delta \lambda)] - {}^{t+\Delta t} c(\sigma, \Delta \lambda) \quad (5.45)$$

and is solved iteratively in a Newton-Raphson scheme as before, eq. (5.22). The Jacobian and consistent tangent stiffness matrix for this solution are given by Van Zijl (1999a).

In the shear/tension corner the stress-corrections can be written as

$$\begin{aligned}
 {}^{t+\Delta t}\boldsymbol{\sigma} &= \boldsymbol{\sigma}^{tr} - \mathbf{D} \left(\Delta\lambda_1 {}^{t+\Delta t} \frac{\partial g_1}{\partial \boldsymbol{\sigma}} - \Delta\lambda_2 {}^{t+\Delta t} \frac{\partial f_2}{\partial \boldsymbol{\sigma}} \right) \\
 &= \left\{ \begin{array}{l} \boldsymbol{\sigma}^{tr} - k_n \Delta\lambda_1 {}^{t+\Delta t} \Psi_s - k_n \Delta\lambda_2 \\ \tau_s^{tr} \left(1 + k_s \Delta\lambda_1 / \left[\sqrt{(\tau_s^{tr})^2 + (\tau_t^{tr})^2} - k_s \Delta\lambda_1 \right] \right)^{-1} \\ \tau_t^{tr} \left(1 + k_s \Delta\lambda_1 / \left[\sqrt{(\tau_s^{tr})^2 + (\tau_t^{tr})^2} - k_s \Delta\lambda_1 \right] \right)^{-1} \end{array} \right\}. \quad (5.46)
 \end{aligned}$$

As for the plane-stress case, a set of two coupled, nonlinear equations arise upon substitution of the stress-corrections into the two yield functions (5.26, 5.41). The Jacobian for the solution of the plastic flow increments from this set of equations has been elaborated by Van Zijl (1999a).

By differentiation of the updating equations the following consistent tangent modulus can be derived:

$$\mathbf{D}^{ep} = \mathbf{H}^{-1} - \mathbf{H}^{-1} \mathbf{U} (\mathbf{V}^T \mathbf{H}^{-1} \mathbf{U} - \mathbf{E})^{-1} \mathbf{V}^T \mathbf{H}^{-1} \quad (5.47)$$

with

$$\begin{aligned}
 \mathbf{H} &= \mathbf{D}^{-1} + \Delta\lambda \frac{\partial^2 g}{\partial \boldsymbol{\sigma}^2} \\
 d\boldsymbol{\Lambda} &= \begin{Bmatrix} d\lambda_1 \\ d\lambda_2 \end{Bmatrix} \\
 \mathbf{U} &= \left[\begin{array}{c|c} \frac{\partial g_1}{\partial \boldsymbol{\sigma}} + \Delta\lambda_1 \frac{\partial^2 g_1}{\partial \kappa_1 \partial \boldsymbol{\sigma}} \frac{\partial \kappa_1}{\partial \lambda_1} & \frac{\partial f_2}{\partial \boldsymbol{\sigma}} + \Delta\lambda_1 \frac{\partial^2 g_1}{\partial \kappa_1 \partial \boldsymbol{\sigma}} \frac{\partial \kappa_1}{\partial \lambda_2} \end{array} \right] \\
 \mathbf{V} &= \left[\begin{array}{c|c} \frac{\partial f_1}{\partial \boldsymbol{\sigma}} & \frac{\partial f_2}{\partial \boldsymbol{\sigma}} \end{array} \right] \\
 \mathbf{E} &= \left[\begin{array}{c|c} \left(\frac{\partial f_1}{\partial \Phi} \frac{\partial \Phi}{\partial c} + \frac{\partial f_1}{\partial c} \right) \frac{\partial c}{\partial \kappa_1} \frac{\partial \kappa_1}{\partial \lambda_1} & \left(\frac{\partial f_1}{\partial \Phi} \frac{\partial \Phi}{\partial c} + \frac{\partial f_1}{\partial c} \right) \frac{\partial c}{\partial \kappa_1} \frac{\partial \kappa_1}{\partial \lambda_2} \\ \frac{\partial f_2}{\partial \sigma_t} \frac{\partial \sigma_t}{\partial \kappa_2} \frac{\partial \kappa_2}{\partial \Delta\lambda_1} & \frac{\partial f_2}{\partial \sigma_t} \frac{\partial \sigma_t}{\partial \kappa_2} \frac{\partial \kappa_2}{\partial \Delta\lambda_2} \end{array} \right], \quad (5.48)
 \end{aligned}$$

the derivation of which is also given by Van Zijl (1999a).

5.2 Continuum modelling

An alternative, continuous modelling approach has become usual for concrete. However, the relation between the structural and “grain/particle” (brick) dimensions places masonry at, and in some cases beyond the limit of applicability of this approach. For instance, buildings of calcium silicate elements/blocks sometimes contain piers of the width of a single unit, which calls for the separate modelling of the elements/blocks and their connections. Yet, where the brick dimension is sufficiently small compared to the structural dimension, the continuum strategy may be followed to model large masonry structures in a compromise between computational accuracy and viability. Then the material can be considered to be homogeneous and continuous, in which a relation can be established between average stresses and strains.

5.2.1 AN ANISOTROPIC RANKINE-HILL MODEL

A plane-stress continuum model was formulated by Lourenço (1996). It is based on multi-surface plasticity, comprising of a Rankine yield criterion combined with a Hill criterion for compression, Figure 5.8. This choice was inspired by the form of the observed failure envelopes shown in Figure 2.16. This model is elaborated here to illuminate its interaction with the total mechanical model.

To account for the different strengths parallel and perpendicular to the bed joints in masonry, anisotropic versions of both the Rankine and Hill yield criteria are employed. Tension softening and compression hardening, followed by softening capture the total degradation process, governed by different values of the fracture energy along each material

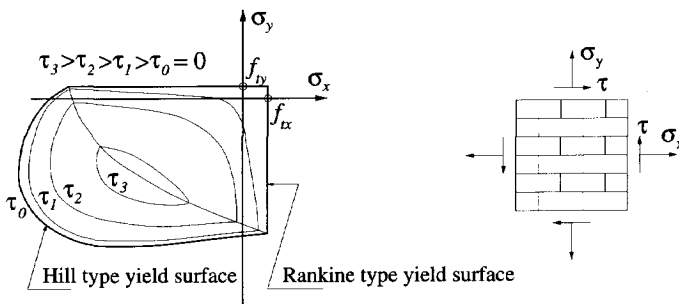


Figure 5.8: Continuum material model (Lourenço 1996).

axis in both compression and tension. The strength parameters are the tension (f_{tx}, f_{ty}) and compression (f_{cx}, f_{cy}) strengths in both directions, while the softening parameters are the tension (G_{fx}, G_{fy}) and the compression (G_{fcx}, G_{fcy}) fracture energies and the limiting equivalent plastic strain between initial parabolic hardening and subsequent softening in compression (κ_p). The parameters which determine the shape of the yield functions are α_τ , which controls the shear stress contribution to tensile failure ($\alpha_\tau = 1.0$ being the standard Rankine value), β , which couples the normal compressive stresses (typically $\beta = -1$ for masonry) and γ , which controls the shear stress contribution to compressive failure ($\gamma = 3.0$ for the isotropic Von Mises model).

Cracking due to eigenstressing and structurally restrained shrinkage is of particular importance here. Therefore, in the analyses reported in this report the Hill criterion is not activated. As the plasticity formulation is influenced by the combination with visco-elasticity, stress-dependent shrinkage and crack opening rate dependence, the Rankine formulation is elaborated in detail.

The yield criterion (3.47) for the Rankine model reads

$$f = \sqrt{\frac{1}{2} \xi^T P_t \xi} + \frac{1}{2} \pi^T \xi \quad (5.49)$$

with the projection matrix P_t and vector π given by

$$\begin{aligned} P_t &= \frac{1}{2} \begin{bmatrix} 1 & -1 & . \\ -1 & 1 & . \\ . & . & 4\alpha_\tau \end{bmatrix} \\ \pi^T &= \{ 1 \ 1 \ 0 \}. \end{aligned} \quad (5.50)$$

The parameter α_τ controls the shear stress contribution to failure and can be expressed as (Lourenço 1996)

$$\alpha_\tau = \frac{f_{tx} f_{ty}}{\tau_u^2} \quad (5.51)$$

where τ_u is the shear strength at zero normal stress. The normal Rankine value is $\alpha_\tau = 1$.

The reduced stress vector reads

$$\xi = \sigma - \Gamma \quad (5.52)$$

with

$$\begin{aligned} \sigma^T &= \{ \sigma_x \ \sigma_y \ \tau_{xy} \} \\ \Gamma^T &= \{ \sigma_{tx} \ \sigma_{ty} \ 0 \}. \end{aligned} \quad (5.53)$$

Exponential softening is assumed in the orthogonal directions, described by

$$\begin{aligned}\sigma_{tx} &= f_{tx} e^{-\frac{f_{tx}}{g_{fx}} \kappa} \\ \sigma_{ty} &= f_{ty} e^{-\frac{f_{ty}}{g_{fy}} \kappa}.\end{aligned}\quad (5.54)$$

A simple way of including the rate contribution to cracking resistance, eq. (3.56), is by adding it to the "static" strength

$$\begin{aligned}\sigma_{tx} &= \left(f_{tx} + m \frac{\Delta \kappa}{\Delta t} \right) e^{-\frac{f_{tx}}{g_{fx}} \kappa} \\ \sigma_{ty} &= \left(f_{ty} + m \frac{\Delta \kappa}{\Delta t} \right) e^{-\frac{f_{ty}}{g_{fy}} \kappa}.\end{aligned}\quad (5.55)$$

Lourenço (1996) does not include the second, crack mouth opening rate term. To ensure that the results are objective with regard to mesh refinement, he relates the energy released per unit crack area G_f to a representative mesh dimension l_m , following Bažant and Oh (1983), Crisfield (1984), Rots (1988) and Feenstra (1993). If it is assumed that the inelastic work g_f is uniformly distributed over l_m , this relation is given by

$$g_f = \frac{G_f}{l_m}. \quad (5.56)$$

The softening is governed by the maximum principal plastic strain as follows

$$\Delta \kappa = \Delta \epsilon_{1,p} = \sqrt{\frac{1}{2} (\Delta \epsilon_p)^T \mathbf{P} \Delta \epsilon_p} + \frac{1}{2} \boldsymbol{\pi}^T \Delta \epsilon_p \quad (5.57)$$

with

$$\mathbf{P} = \frac{1}{2} \begin{bmatrix} 1 & -1 & . \\ -1 & 1 & . \\ . & . & 1 \end{bmatrix}. \quad (5.58)$$

The plastic strain follows from the flow rule

$$\Delta \epsilon_p = \Delta \lambda \frac{\partial g}{\partial \boldsymbol{\sigma}} \quad (5.59)$$

with the plastic potential given by

$$g = \sqrt{\frac{1}{2} \boldsymbol{\xi}^T \mathbf{P}_g \boldsymbol{\xi}} + \frac{1}{2} \boldsymbol{\pi}^T \boldsymbol{\xi} \quad (5.60)$$

and

$$\mathbf{P}_g = \frac{1}{2} \begin{bmatrix} 1 & -1 & . \\ -1 & 1 & . \\ . & . & 4 \end{bmatrix}. \quad (5.61)$$

By substitution of the plastic strains into eq. (5.57) the equivalent strain increment reduces to

$$\Delta\kappa = \Delta\lambda. \quad (5.62)$$

For the solution of the stresses and plastic flow increment the stress-update eqs. (4.35,4.36) and yield function eq. (5.49) are solved simultaneously, as described by eqs. (4.37 - 4.39). The Jacobian (4.39) required is

$$\mathbf{J} = \left[\begin{array}{c|c} (\mathbf{D}^{ve})^{-1} + \Delta\epsilon_{s,o} \mathbf{r}_s + \Delta\epsilon_{t,o} \mathbf{r}_t + \Delta\lambda \frac{\partial^2 g}{\partial \sigma^2} & \frac{\partial g}{\partial \sigma} + \Delta\lambda \frac{\partial^2 g}{\partial \sigma \partial \kappa} \\ \hline \left(\frac{\partial f}{\partial \sigma} \right)^T & \frac{\partial f}{\partial \kappa} \end{array} \right] \quad (5.63)$$

with

$$\begin{aligned} \frac{\partial f}{\partial \sigma} &= \frac{\mathbf{P}_t \xi}{2\sqrt{\frac{1}{2}\xi^T \mathbf{P}_t \xi}} + \frac{1}{2} \pi \\ \frac{\partial f}{\partial \kappa} &= - \left(\frac{\partial f}{\partial \sigma} \right)^T \frac{\partial \Gamma}{\partial \kappa} \\ \frac{\partial \Gamma}{\partial \kappa} &= \left\{ \frac{\partial \sigma_{tx}}{\partial \kappa} \frac{\partial \sigma_{ty}}{\partial \kappa} 0 \right\}^T \\ \frac{\partial g}{\partial \sigma} &= \frac{\mathbf{P}_g \xi}{2\sqrt{\frac{1}{2}\xi^T \mathbf{P}_g \xi}} + \frac{1}{2} \pi \\ \frac{\partial^2 g}{\partial \sigma^2} &= \frac{\mathbf{P}_g}{2\sqrt{\frac{1}{2}\xi^T \mathbf{P}_g \xi}} - \frac{\mathbf{P}_g \xi \xi^T \mathbf{P}_g}{4(\frac{1}{2}\xi^T \mathbf{P}_g \xi)^{3/2}} \\ \frac{\partial^2 g}{\partial \sigma \partial \kappa} &= - \frac{\partial^2 g}{\partial \sigma^2} \frac{\partial \Gamma}{\partial \kappa}. \end{aligned} \quad (5.64)$$

For treatment of the apex the reader is referred to Lourenço (1996).

The approximate tangent modulus excluding the stress-induced shrinkage and thermal strain is, cf. eqs. (4.45, 5.63):

$$\mathbf{D}^{vp} = \frac{\partial \boldsymbol{\sigma}}{\partial \boldsymbol{\epsilon}} = \left[(\mathbf{D}^{ve})^{-1} + \Delta \lambda \frac{\partial^2 g}{\partial \boldsymbol{\sigma}^2} \right]^{-1}, \quad (5.65)$$

which is to be substituted into eq. (4.54a) to obtain the consistent tangent \mathbf{D}^{cf} .

The time derivative (4.69) needed for adaptive time-stepping discussed in section 4.2.6 can now be completed by deriving

$$\frac{\partial \mathbf{D}^{vp}}{\partial \Delta t} = -\mathbf{D}^{vp} \frac{\partial}{\partial \Delta t} \left[(\mathbf{D}^{ve})^{-1} + \Delta \lambda \frac{\partial^2 g}{\partial \boldsymbol{\sigma}^2} \right] \mathbf{D}^{vp}. \quad (5.66)$$

The first term is completed by elaborating

$$\frac{\partial}{\partial \Delta t} \left[(\mathbf{D}^{ve})^{-1} \right] = (\mathbf{D}^{ve})^{-1} \frac{\partial \mathbf{D}^{ve}}{\partial \Delta t} (\mathbf{D}^{ve})^{-1} \quad (5.67)$$

with, by differentiation of eq. (4.32)

$$\frac{\partial \mathbf{D}^{ve}}{\partial \Delta t} = \sum_{n=1}^N \frac{E_n}{\Delta t / \zeta_n} \left[\frac{1}{\zeta_n} e^{-\Delta t / \zeta_n} - \frac{1}{\Delta t} \left(1 - e^{-\Delta t / \zeta_n} \right) \right] \mathbf{D}. \quad (5.68)$$

The second term is dependent upon the time increment due to the crack mouth opening rate dependence and reads

$$\begin{aligned} \frac{\partial}{\partial \Delta t} \left(\frac{\partial^2 g}{\partial \boldsymbol{\sigma}^2} \right) = & \frac{2\mathbf{P}_g \left(\frac{\partial \boldsymbol{\xi}}{\partial \Delta t} \boldsymbol{\xi}^T + \boldsymbol{\xi} \frac{\partial \boldsymbol{\xi}^T}{\partial \Delta t} \right) \mathbf{P}_g - \left(\frac{\partial \boldsymbol{\xi}^T}{\partial \Delta t} \mathbf{P}_g \boldsymbol{\xi} - \boldsymbol{\xi}^T \mathbf{P}_g \frac{\partial \boldsymbol{\xi}}{\partial \Delta t} \right) \mathbf{P}_g}{8 \left(\frac{1}{2} \boldsymbol{\xi}^T \mathbf{P}_g \boldsymbol{\xi} \right)^{3/2}} \\ & - \frac{3 \left(\frac{\partial \boldsymbol{\xi}^T}{\partial \Delta t} \mathbf{P}_g \boldsymbol{\xi} + \boldsymbol{\xi}^T \mathbf{P}_g \frac{\partial \boldsymbol{\xi}}{\partial \Delta t} \right) \mathbf{P}_g \boldsymbol{\xi} \boldsymbol{\xi}^T \mathbf{P}_g}{16 \left(\frac{1}{2} \boldsymbol{\xi}^T \mathbf{P}_g \boldsymbol{\xi} \right)^{9/2}}. \end{aligned} \quad (5.69)$$

5.2.2 THE REGULARISATION OF THE LOCALISATION PROBLEM

As mentioned in the previous section, the equivalent length l_m may be related to a representative FE mesh dimension to strive at objective results upon mesh refinement, following the crack band model by Bažant and Oh (1983). However, this does not prevent the

loss of well-posedness in softening solids (Sluys 1992), which is associated with mesh-dependent crack spacing and alignment. In this study the simplest form of regularisation of the problem in terms of implementation ease is employed, by including a rate term, of which a physical rationale has been given in section 3.2.4. As an illustration of the regularisation the one-dimensional tension bar shown in Figure 5.9a is analysed.

The bar has a linearly increasing cross section area A such that $A(L)/A(0) = 1.5$ to avoid a homogeneous solution. It is discretised into 10, 20 and 40 elements, respectively, along the length. If no rate term is included, as is simulated by setting $m=0$, an inobjective response is obtained. This is reflected by the plastic strain localisation, Figure 5.9b for $m=0$. For each mesh the plasticity is restricted to a single element at the left support. Furthermore, a reduced energy dissipation upon mesh refinement can be seen in Figure 5.9c for $m=0$. Note that if the energy dissipation is related to the element size, the stress-deformational response may be corrected, but the localisation zone remains mesh dependent.

For the case of crack rate dependence three viscosities, $m = 1, 2, 5 \text{ Ns/mm}^2$, are employed. From Figure 5.9b it is evident that a mesh-objective localisation width is produced in each of the three cases. Now also the energy dissipation is objective upon mesh refinement, Figure 5.9c.

Note that the divergence in stress-displacement responses for the different meshes after some degradation (in the case of $m = 1 \text{ Ns/mm}^2$ for $u \geq 0.2 \text{ mm}$, Figure 5.9c) is caused by the exponentially diminishing rate term contribution, eq. (5.55).

The same bar is analysed employing the crack mouth opening rate model proposed by Bažant (1993), eq. (3.55). The offset parameter is chosen as $k_1=0.1$. The remaining two parameters k_0 and $\dot{\kappa}_r$ are estimated to obtain the same approximate 20% peak strength increase as computed with the simple cracking rate model for $m=1 \text{ Ns/mm}^2$, Figure 5.9c. However, with this criterion a unique combination of these parameters does not exist. Three pairs, $(k_0=0.03, \dot{\kappa}_r=5 \cdot 10^{-4} \text{ s}^{-1})$, $(k_0=0.14, \dot{\kappa}_r=0.1 \text{ s}^{-1})$ and $(k_0=1.0, \dot{\kappa}_r=1.0 \text{ s}^{-1})$, are employed. Figure 5.10 shows the stress-deformation responses. An approximate 20% increase in the peak strength is indeed computed for all three cases. However, for the first case and, except for the initial part of the localisation process, for the second case this formulation does not regularise sufficiently, because in the post-peak regime a mesh-dependent solution response prevails, Figure 5.10a,b. This is due to the strong damping nature of the inverse hyperbolic operator in the formulation for large values of $\dot{\kappa}/\dot{\kappa}_r$, or small values of the reference cracking strain $\dot{\kappa}_r$. Note that the first set of parameters, Figure 5.10a, is the more appropriate choice proposed by Wu and Bažant (1983), which produces a realistic strength increase upon an increased loading rate, section 3.2.4.

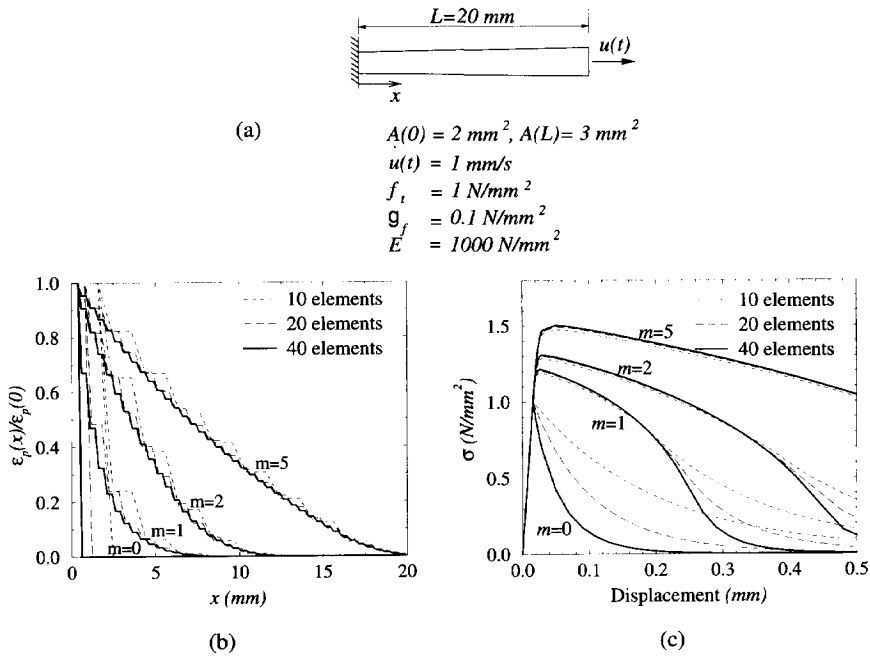


Figure 5.9: (a) Tension bar example for illustration of the regularisation by considering the crack mouth opening rate dependence. (b) Plastic strain localisation with various crack mouth opening viscosities m at a bar end displacement $u = 0.21 \text{ mm}$. (c) Stress in the bar at the constraint vs. bar end displacement.

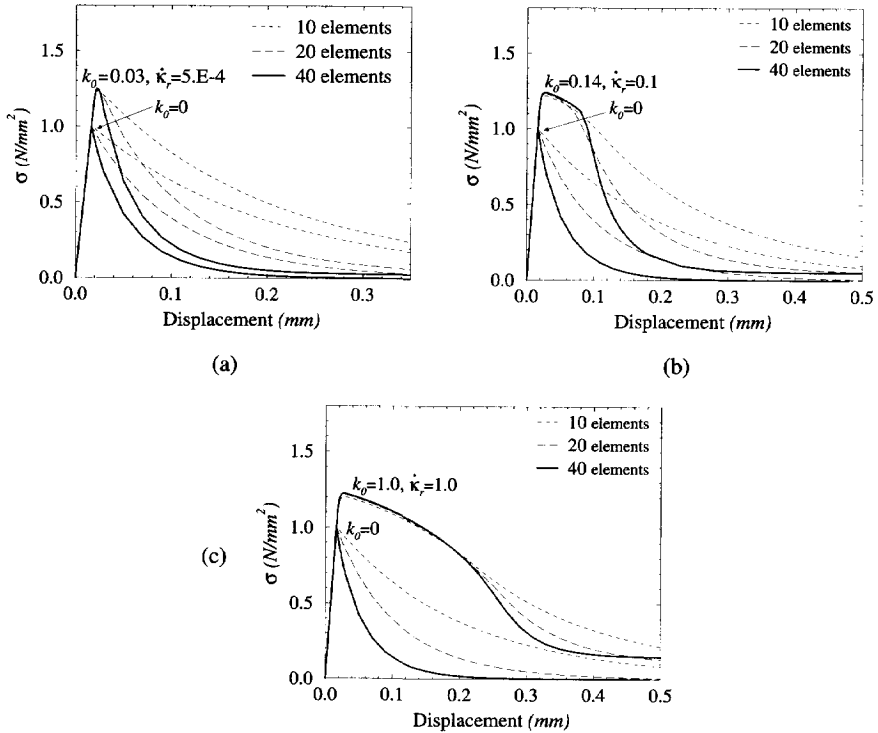


Figure 5.10: Stress in the bar at the constraint when employing the crack mouth opening formulation of eq. (3.55) by Wu and Bažant (1993) with: (a) $k_0=0.03, \dot{\kappa}_r=5.10^{-4} \text{ s}^{-1}$, (b) $k_0=0.14, \dot{\kappa}_r=0.1 \text{ s}^{-1}$ and (c) $k_0=1.0, \dot{\kappa}_r=1.0 \text{ s}^{-1}$.

Chapter 6

VALIDATION OF THE MECHANICAL MODEL: FAILURE UNDER SUSTAINED LOAD

It makes sense to validate and verify the model in a modular fashion. In this chapter only the mechanical part is activated to study its ability to simulate the interaction between fracture and creep. The three-point bending creep tests performed by Zhou (1992) are analysed. During these experiments the drying of the specimens was prevented, which avoids the further complication introduced by the simultaneous drying shrinkage. If the intricate mechanical behaviour is captured by the model satisfactorily, the next level of complication can be entered with confidence. This is done in Chapter 7, where transient creep experiments are analysed.

The creep tests by Zhou relate to concrete. Tensile creep experiments on masonry appear to be very scarce. However, despite the obvious difference in the microstructural scale, the shared cementitious nature of both materials is of dominant importance in governing their behaviour. For the model to correctly simulate creep and cracking in masonry, the ability to do so for concrete seems a prerequisite.

The creep deformation as well as the time to failure under the sustained creep load is investigated. The role of the cracking rate dependence is brought out. Also, new light is shed on the long term behaviour, which brings about an increased deformability and requires a new definition of the creep failure envelope. This chapter ends with a brief discussion of the requirement of a nonuniform stress field for the correct description of creep failure with a macroscopic approach.

6.1 Description of three-point bending tests

The geometry of the 100 mm thick notched concrete beams which were tested by Zhou (1992), is shown in Figure 6.1a. He performed both displacement-controlled and force-controlled experiments, the results of which are shown in Figure 6.1b. With the first type of tests the total load-deformation response from elastic behaviour, through the peak load and the degradation up to zero resistance was found. Force control enabled the load to be increased to a predefined level, which was subsequently sustained. A sustained load of larger than about 60% of the peak load eventually led to failure of the beams. In these cases sufficient micro-cracking was initiated to eventually coalesce into a macro-crack and to subsequently propagate until failure. The displacement-controlled response seems to form a failure envelope, which determines the deformation at failure under the sustained load. Typical results of total load-deformation response under displacement control at 5 $\mu\text{m/s}$, as well as the results of sustained load tests at 92%, 85%, 80% and 76% of the average of the peak loads obtained in the former tests are shown in Figure 6.1b. Both the load versus the crack mode opening displacement (CMOD) and the load versus the deflection at midspan are shown in the figure. The CMODs at failure under sustained loads are indicated by an X.

The finite element mesh employed for the analyses is also shown in Figure 6.1a. It consists of plane-stress, four-noded quadrilateral elements. Symmetry is exploited, enabling one half of the model only to be modelled.

The Rankine plasticity formulation is employed to capture the crack initiation and propa-

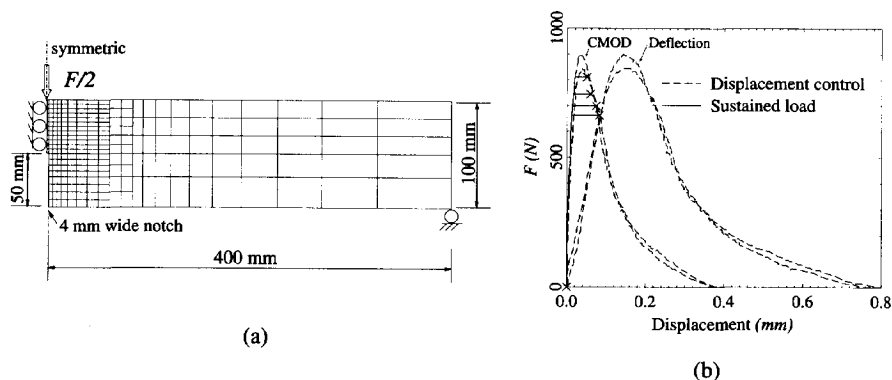


Figure 6.1: Three-point bending tests by Zhou (1992). (a) Specimen geometry, set-up and FE model, (b) force-CMOD and force-deflection results (Zhou 1992).

gation in a smeared fashion. A crack band width $l_m = 4 \text{ mm}$ is assumed, which is equal to the notch width. To study the cracking rate dependence, the formulation proposed by Wu and Bažant (1993), eq. (3.55), as well as the simple cracking viscosity model, eq. (3.56), are employed. Bulk creep is considered by activating the Maxwell chain incorporated in the constitutive model. The own weight is compensated for by applying a volume load of mass density 2400 kg/m^3 in an initial step in each analysis.

6.2 Characterisation of the model parameters

Separate tests were performed to determine the material parameters, yielding a Young's modulus 36 kN/mm^2 and the tensile strength $f_t = 2.8 \text{ N/mm}^2$ (Zhou 1992). Also, relaxation tests were performed on cylindrical, notched tensile specimens, providing information for determining the bulk creep parameters, Figure 6.2. Unfortunately, the relaxation was measured over short times (maximum 1 hour), calling for extrapolation. Two such extrapolations were made to give creep coefficients of $\phi = \epsilon_c/\epsilon_e = 2$ and 5 respectively after 100 days, considered to be the limiting cases for concrete. A 10-element Maxwell chain model was fitted by a least squares method to each relaxation curve - Figure 6.2. The initial load on the specimens was about 75% of the strength, so inevitably micro-cracking must have occurred and influenced the amount of relaxation.

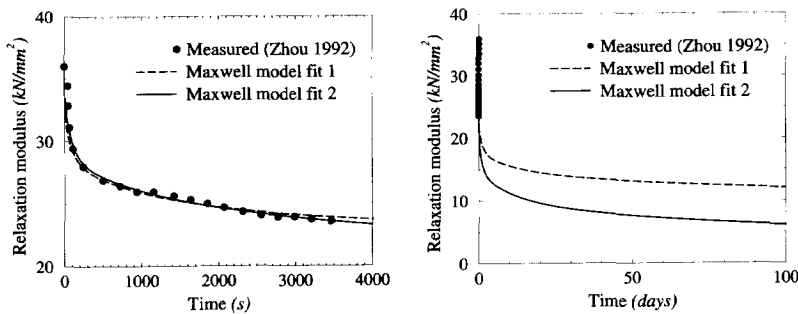


Figure 6.2: Maxwell chain fits to the extrapolated relaxation data.

Zhou (1992) also performed three-point bending tests under displacement control on smaller beams (600 mm long by $50 \times 50 \text{ mm}^2$ section) to determine the fracture energy G_f . By varying the deflection rate from slow ($0.05 \text{ }\mu\text{m/s}$ - peak load after about 80 minutes) to fast ($50 \text{ }\mu\text{m/s}$ - peak load after about 5 s) he studied the rate influence on the fracture energy, Figure 6.3a, and peak strength, Figure 6.3b.

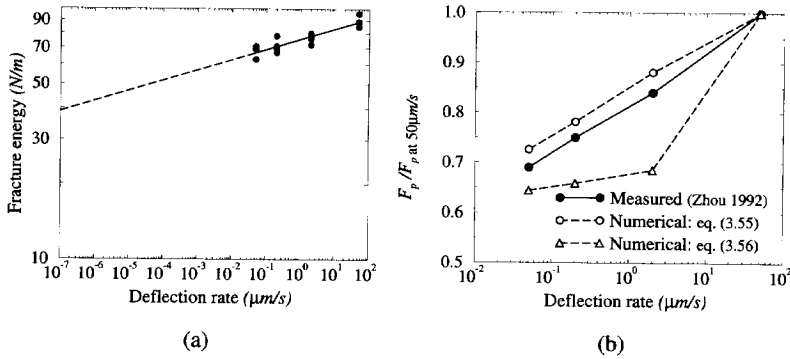


Figure 6.3: Rate effect on (a) fracture energy and (b) peak strength (Zhou 1992).

To derive the parameters for the crack mouth opening rate (CMOR) dependence models, eqs. (3.55,3.56), a process of inverse fitting has been followed. For these analyses the smaller beam has been modelled with the same mesh shown in Figure 6.1a, scaled to the small beam geometry. The parameters which have been obtained in this way are, for eq. (3.55): $k_0 = 0.05$, $k_1 = 0.1$, $\dot{\kappa}_r = 10^{-7} s^{-1}$ and for eq. (3.56): $m = 1500 Ns/mm^2$. In figure 6.3b the normalised numerical peak strengths are compared with the measured values. Reasonable agreement is found with the three parameter model, but with the simple one parameter model it is impossible to fit the strength increase over the total range of loading rates. A possible remedy is to employ a rate-dependent viscosity $m(\dot{\kappa})$. This has not been attempted. Instead, the three parameter model has been employed for the subsequent analyses in this Chapter. In all cases localisation has occurred over the prescribed crack band width $l_m = 4 mm$, which indicates that the correct amount of cracking energy has been dissipated.

With regard to the apparent increase in fracture energy with loading rate, it must be noted that it follows from the numerical model while employing a prescribed constant fracture energy. This value can be estimated by extrapolation to the deflection rate at the reference CMO strain rate $\dot{\kappa}_r$, Figure 6.3a. A constant value of $G_f = 0.035 N/mm$ has been used.

6.3 The failure envelope by displacement control

The experimental results indicate that the displacement-controlled response forms an envelope for failure under a sustained load, Figure 6.1b. Therefore, this case is analysed first,

with the deflection rate $5 \mu\text{m/s}$, as employed in the experiment. Note that the Maxwell model fit 2, Figure 6.2, is employed. Figure 6.4 compares the numerical response with the experimental responses. To obtain this agreement a 5% lower tensile strength than the reported $f_t = 2.8 \text{ N/mm}^2$ (Zhou 1992) and a Young's modulus 30 kN/mm^2 have been used. On the one hand these adjustments have been made to give reasonable agreement with the experimental responses, in order to make possible the subsequent comparison between the responses under sustained load. On the other hand the strength and stiffness are rate dependent. Thus, the reduction of the measured parameters is in line with the determination of the "rate-independent" values, as has been done in the previous section for the fracture energy.

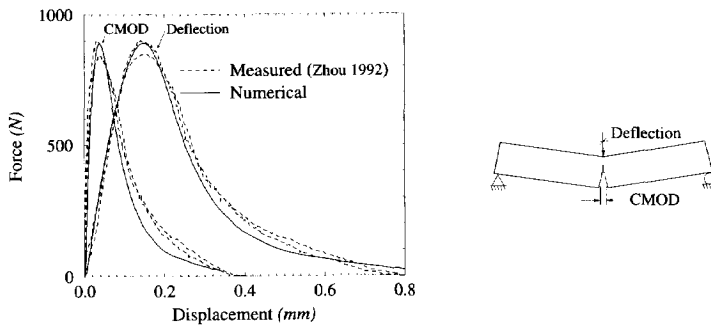


Figure 6.4: Displacement-controlled ($5 \mu\text{m/s}$) experimental and numerical force-deflection and force-CMOD responses.

6.4 Sustained load response

Next, the sustained load cases are analysed. As for the displacement-controlled analyses of the previous section, the Maxwell model fit 2 is employed. Figure 6.5 shows the results. Following the experiments (Zhou 1992), the load is increased to a certain portion of the peak load F_p of the displacement-controlled analysis. Four cases are considered, namely load levels of $0.76F_p$, $0.80F_p$, $0.85F_p$ and $0.92F_p$. As was attempted in the experiments (Zhou 1992), the initial, ascending loading rate is the same as for the displacement-controlled case. Beyond this ascending branch the load level is kept constant and the creep behaviour is analysed. During this stage the crack propagates and the deflection and CMOD increase up to a point where equilibrium can no longer be achieved for the sustained load level. Here, the load bearing capacity of the beam is exceeded. To

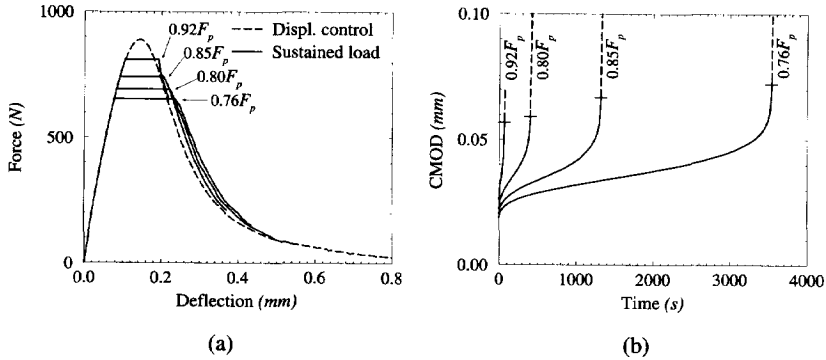


Figure 6.5: Three-point bending numerical results. (a) Force-deflection responses and (b) CMOD evolutions.

ensure that failure under the sustained load is indeed imminent, the analyses are continued, by replacing the force control with displacement control at this point. This results in the subsequent softening responses, Figure 6.5a, which prove that failure would have occurred under continued load control. The CMOD evolutions are shown in Figure 6.5b. The points of failure are marked, with dashed lines indicating the subsequent continued crack mouth opening under displacement control.

These results confirm the experimental observation that the displacement-controlled response serves as an envelope for failure under sustained loads. Also, reasonable agreement is found with the measured times between reaching the sustained load level and failure t_f . Figure 6.6a shows these times for the experiments and for the analyses. Also, the agreement between the measured and computed CMOD values at the point of failure is reasonable. This is quantified in Figure 6.6b.

6.5 The failure envelope for long term, rate-independent response

It is interesting to study the sustained load numerical response when the crack rate dependence is ignored. In the first place, it illustrates that the crack rate dependence is more than a numerical regularisation tool, sections 3.3, 5.2.2. Secondly, it reveals that the failure envelope should be modified in the case of very slow load application, where the cracking rate becomes negligible.

To illustrate these issues, the displacement-controlled and sustained load analyses are

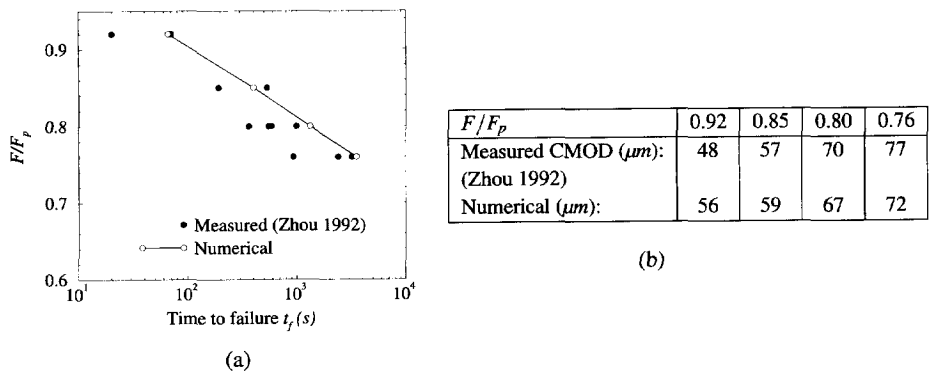


Figure 6.6: Three-point bending (a) time to failure and (b) CMOD at the point of failure under sustained load.

repeated, but now with the CMOR contribution deactivated. Once again the Maxwell model fit 2 shown in Figure 6.2 is employed to capture the bulk creep. For these crack rate-independent analyses the model parameters applicable at the $5\text{ }\mu\text{m/s}$ loading rate, namely $G_f\!=\!0.08\text{ N/mm}$, $f_t\!=\!2.8\text{ N/mm}^2$ and $E\!=\!36\text{ kN/mm}^2$, are employed. This is done to obtain agreement with the measured behaviour under displacement control, Figure 6.7, so as to allow subsequent comparison of the experimental and numerical sustained load responses.

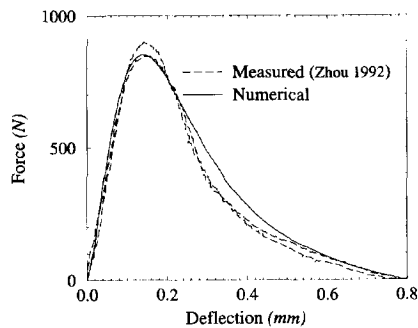


Figure 6.7: Displacement-controlled ($5\text{ }\mu\text{m/s}$) experimental and numerical force-deflection responses when the crack rate dependence is deactivated in the analysis.

Figure 6.8a shows the numerical load-deflection responses for both the displacement-controlled and the sustained load analyses. For the former various deflection rates have been employed, with times to peak approximately 30 s (the $5\text{ }\mu\text{m/s}$ case), 10 hours , 75

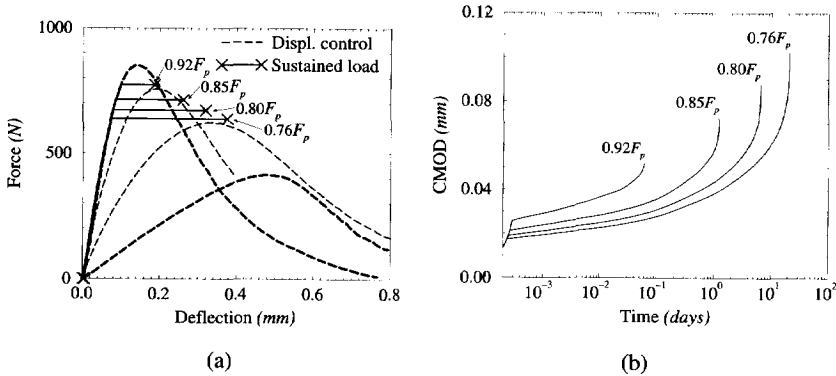


Figure 6.8: Numerical three-point bending results when only the bulk creep is considered. (a) Force-deflection response for four levels of sustained loads and for displacement control at four deflection rates. (b) CMOD evolutions under sustained load.

days and several years respectively. The X symbols denote the point after which no further convergence can be found under the sustained load, which indicates a reduced load carrying capacity and thus failure. The vertical slope of the CMOD responses shown in Figure 6.8b confirms that failure is due in each case.

Now, unlike in the previous section, a single displacement-controlled response does not define the displacement at which failure occurs under sustained load. Instead, the envelope which is formed by the responses to the two extreme loading rates, serves this role. The upper limit is found when loading is so fast that there is no time for relaxation, but the crack rate dependence is still negligible. This case can be simulated by considering an instantaneous response, i.e. a time-independent analysis with $E = E_o + \sum_{n=1}^N E_n = 36 \text{ kN/mm}^2$. The lower limit is defined by the response when only the Maxwell element without dashpot resists extension, thus the elastic-cracking response with $E = E_o$.

In Figure 6.9 it can be seen that the time between reaching the sustained load level and failure is greatly overestimated if only the bulk creep is considered. In the figure the predicted times are shown also for the lower bulk creep, which is obtained by employing the Maxwell model fit 1, Figure 6.2. From the insignificant reduction in the times to failure brought along by the higher bulk creep, it is clear that by considering the bulk creep only, the time to failure can not be predicted correctly. This provides strong evidence of the validity of the inclusion of the cracking rate dependence.

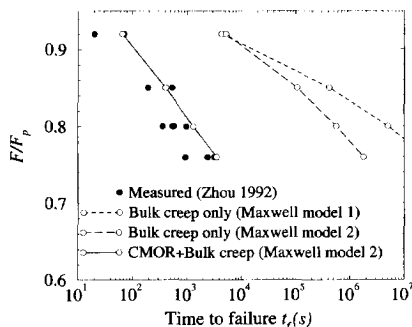


Figure 6.9: Comparison of measured and computed times to failure of three-point bending beams under sustained loads.

6.6 Discussion

The ability to reasonably simulate the experimentally observed interaction between creep and fracture in concrete goes a long way in verifying and validating the mechanical part of the model. It has been demonstrated that the inclusion of the crack rate dependence is essential. As a bonus, the numerical tool enables the investigation of the long term behaviour and the failure under sustained loading of such specimens, which is probably too time consuming and expensive to do physically. In this manner the increased deformational capacity of concrete has been revealed.

Based on the knowledge that the displacement-controlled response forms the envelope for failure under sustained load, it seems natural to formulate a crack initiation criterion based on stresses and strains, De Borst and Van den Berg (1986). This would enable the analysis of creep failure for specimens with uniform stress distributions, such as the dog-bone concrete specimens tested by Cornelissen and Siemes (1984), Figure 6.10. Limited life of their specimens was observed at tensile creep loads in the range $0.6\text{--}0.9F_p$. However, through the redistribution of stresses in a general stress state, the current model represents the crack growth and eventual structural failure correctly, which renders the above mentioned reformulation of the local cracking criterion unnecessary.

Furthermore, due to imperfection and asymmetry, a homogeneous stress state hardly ever occurs. This is illustrated in Figure 6.11, where notches cause the nonuniformity of the stress distribution at the plane of failure. Also, in a discrete modelling approach, section 5.1, the geometrical arrangement of bricks and joint interfaces ensures a nonuniform stress distribution even under uniform loading and without the introduction of imperfections,

Figure 6.12.

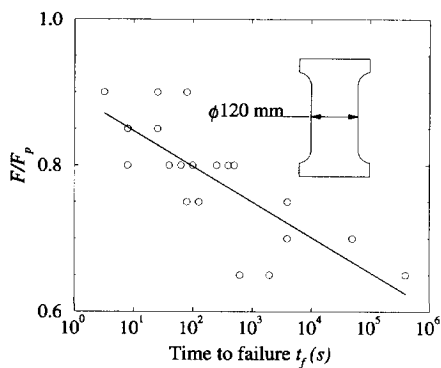


Figure 6.10: Times to failure under sustained, uniaxial load, for specimens with an approximate uniform stress distribution (Cornelissen and Siemes 1984).

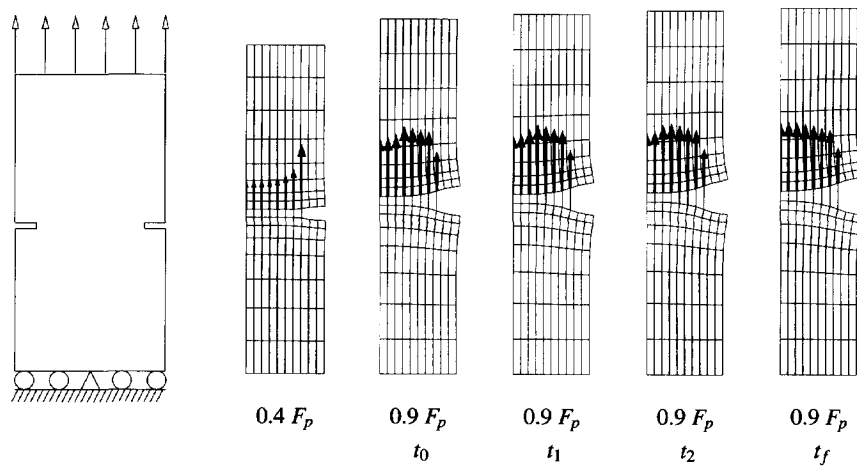


Figure 6.11: Stress evolution in a geometrically imperfect tensile specimen under a sustained uniaxial tensile load.

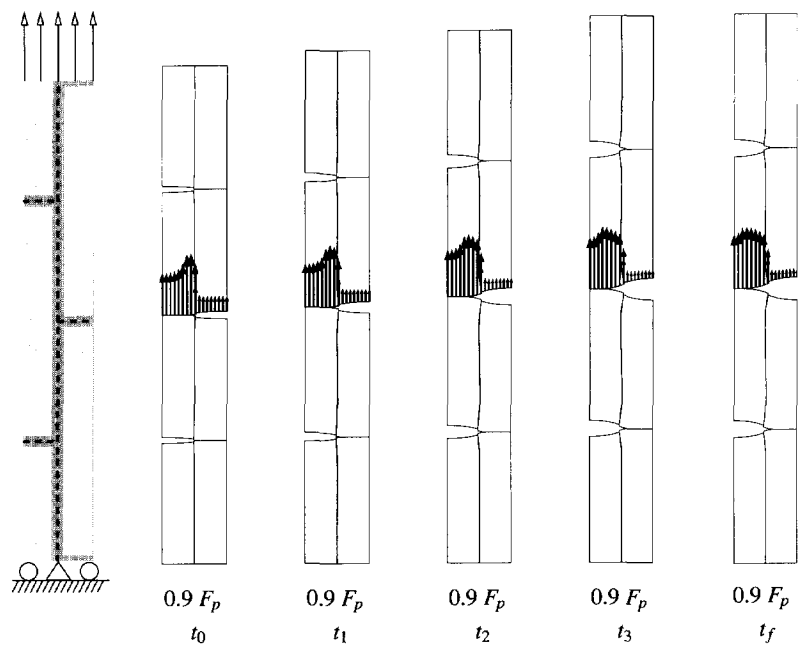


Figure 6.12: Stress evolution in a masonry specimen under a sustained uniaxial tensile load.

Chapter 7

VALIDATION OF THE TOTAL MODEL: MASONRY TRANSIENT CREEP

After the validation for the mechanical part of the model in the previous chapter, the free shrinkage and the creep of masonry specimens are analysed in this chapter. This provides a particularly demanding challenge to the model, because of the intricate interaction of the moisture migration, shrinkage, creep and cracking.

Two typical Dutch masonry combinations tested by Van der Pluijm and Wubs (1996) are studied, namely a large block calcium silicate specimen, which will be referred to as the CS-block specimen, and a small brick (200 mm long, 100 mm wide and 50 mm high) calcium silicate specimen, referred to as CS-brick, Figure 7.1. They are modelled in three dimensions to capture the important out-of-plane hygral gradient and the associated eigenstressing. The discrete modelling approach is followed, because the ratio of the brick/block size to the specimen size renders these specimens beyond the applicability of the continuum approach. The model parameters are estimated from experimental data and, after the analyses with the initial choice of parameter values, the influence of the parameters deemed to be the most important is investigated in a sensitivity study. Special attention is given to the coefficient of stress-induced shrinkage, because of its crucial role in the Pickett effect, which refers to the significant overestimation of the bulk creep.

7.1 Modelling approach

Two masonry specimens tested by Van der Pluijm and Wubs (1996), Figure 7.1a, are analysed. They are modelled in three dimensions, due to the deficiency of plane (two-dimensional) modelling in capturing the slow drying response of a typical cementitious material (Van Zijl 1999b). Due to the slow drying, out-of-plane gradients of moisture content exist before hygral equilibrium is established, which causes nonuniform shrinkage

and associated eigenstressing in the specimens, which can only be captured in a three-dimensional representation.

The discrete modelling approach, Figure 5.1a, is followed, whereby both the bricks/blocks and mortar are discretised. A continuum approach is not valid here, because of the dominating micro-structure of the relatively small specimens, especially in the case of the CS-block specimen. Besides, no simple extension of the anisotropic Rankine model to three dimensions exists. The bricks and mortar are modelled with eight-noded brick elements, which account for the shrinkage, elastic response and bulk creep. The cracking is concentrated at the brick/mortar interfaces, where eight-noded plane interface elements are used, which obey the three-dimensional interface material model described in section 5.1.3. The use of the pore humidity as potential in the diffusion analyses offers the convenience of no special treatment of these interfaces, if they are assumed to be hydraulically perfect, section 3.1.2. However, special eight-noded plane interface elements are needed to account for the interaction with the environment at the exposed faces of the specimens in the pore humidity analyses. There, surface convection is modelled, eq. (3.11c).

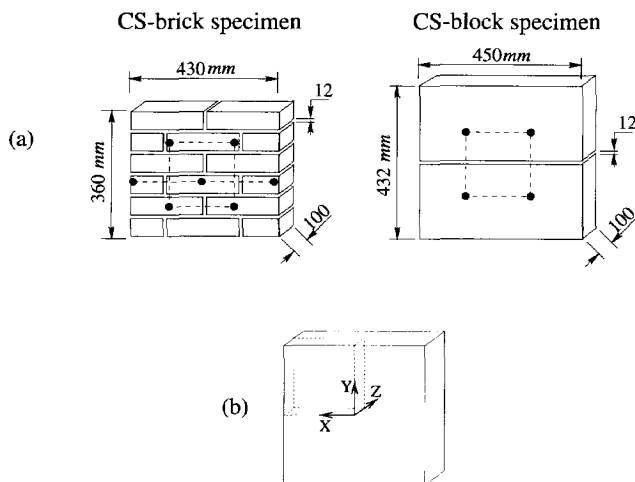


Figure 7.1: (a) Masonry shrinkage specimens investigated. (b) One eighth of each specimen modelled by assumption of symmetry.

Note that symmetry is assumed, requiring only one-eighth of the specimens to be modelled, Figure 7.1b. This is clearly not the case for CS-brick, but the reduced computational effort justifies this simplification. It is believed that the error in the global response introduced by this simplification is insignificant compared with the crudeness of the parameter estimation enforced here by insufficient experimental data. This matter will be discussed next.

7.1.1 CHARACTERISATION OF THE MODEL PARAMETERS

No single, complete set of experimental data exists from which all the model parameters can be derived. The next best option is taken here, by performing parameter estimation with data from different experiments, but on similar materials. Hereby, the introduction of an error is unavoidable, because of the different experimental conditions involved. A further complication is presented by the discrete approach, which requires test data of the constituents separately. This specifically hampers the characterisation of the shrinkage coefficient α_s and the bulk creep parameters, E_n , ζ_n , because only shrinkage and creep data of masonry as a composite are available, requiring some assumptions to be made. Furthermore, no data exist from which the masonry stress-induced shrinkage coefficient matrix r_s can be calculated. All these issues have inspired the proposal of an experimental program (Van Zijl 1999b). For the time being, the crude estimates found along the lines described above are employed, as discussed in the following sections.

7.1.1.1 Model parameters: moisture migration

Pel (1995) performed NMR measurements of moisture profiles during drying of sand-lime specimens, similar to the calcium silicate material bricks/blocks used for the specimens tested by Van der Pluijm and Wubs (1996). The diffusion coefficient derived from the moisture profiles by solution of the one-dimensional moisture diffusion differential equation, as well as by the receding drying front method (Pel 1995) is assumed for the current analyses. The required hygroscopic relation $\theta(h)$ is also obtained from Pel (1995).

Furthermore, Pel measured moisture profiles in a typical masonry mortar, but cured in and subsequently taken from baked clay brick masonry. This procedure ensures that the mortar properties, as significantly influenced by the particular brick/block it is contact with, are measured. As no other mortar drying data are currently available, the diffusivity and hygroscopic curves measured by Pel are employed here. With regard to moisture loss this assumption is justifiable, because the total mortar volume in especially the CS-block

specimen is relatively small. However, the influence on the nonuniform shrinkage field and, accordingly, eigenstressing and cracking in the shrinking masonry specimen, is not easy to predict. The diffusion coefficient and hygroscopic curves employed are shown in Figure 7.2a,b respectively.

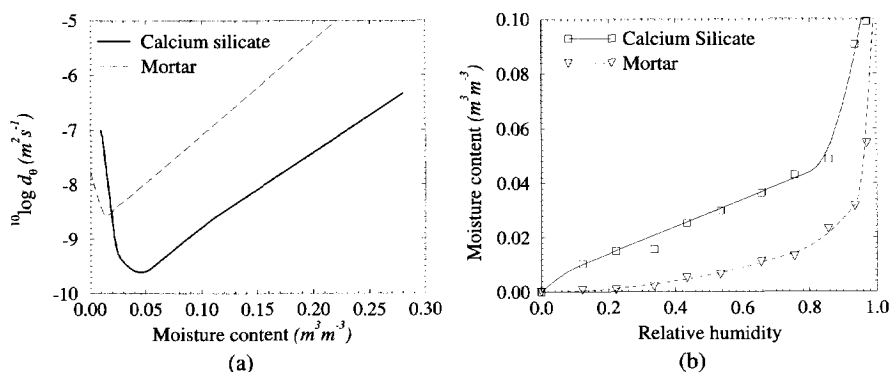


Figure 7.2: (a) Diffusion coefficient variation with moisture content and (b) isothermal desorption curves (Pel 1995).

The surface convection coefficient (also known as film coefficient) is assumed as 5 mm/day for zero air speed (Tammes and Vos 1984). It turns out that the global drying response is insensitive to this coefficient in the range $0.5 \leq \beta < \infty \text{ mm/day}$ - see section 7.4.1. However, the finite value is employed, because it helps to prevent numerical overshoot (Van Zijl 1999b). Note that surface convection is modelled only at the wall face, because the edges of each specimen were sealed in the experiments.

7.1.1.2 Model parameters: mechanical behaviour

The parameters needed to describe the mechanical behaviour are summarised in Tables 7.1 and 7.2. These parameters are based on the experimental studies by Van der Pluijm and Vermeltoort (1991) and Van der Pluijm (1992) and have recently been verified thoroughly (Van Zijl 1996, Van Zijl et al. 1997).

The Maxwell creep model parameters have been obtained by least squares curve fitting of measured compressive creep data of Van der Pluijm and Wubs (1996) - Figure 7.3.

Their transient creep specimens were subjected to a constant load, with an average compressive stress of 2.5 N/mm^2 . They measured shrinkage strains on free shrinkage speci-

Brick		Mortar	
E	ν	E	ν
$\frac{N}{mm^2}$		$\frac{N}{mm^2}$	
11500	0.2	3300	0.2

Table 7.1: Mechanical model parameters employed for bricks and mortar.

k_n	k_s	f_t	G_f^I	c_o	G_f^{II}	$\tan \phi_o$	$\tan \phi_r$	$\tan \psi_o$	σ_u	δ
$\frac{N}{mm^3}$	$\frac{N}{mm^3}$	$\frac{N}{mm^2}$	$\frac{N}{mm}$	$\frac{N}{mm^2}$	$\frac{N}{mm}$				$\frac{N}{mm^2}$	
1.0×10^6	1.0×10^6	0.1	0.005	0.28	$0.02 - 0.03\sigma$	0.97	0.75	0.67	-1.22	17

Table 7.2: Mechanical interface model parameters employed.

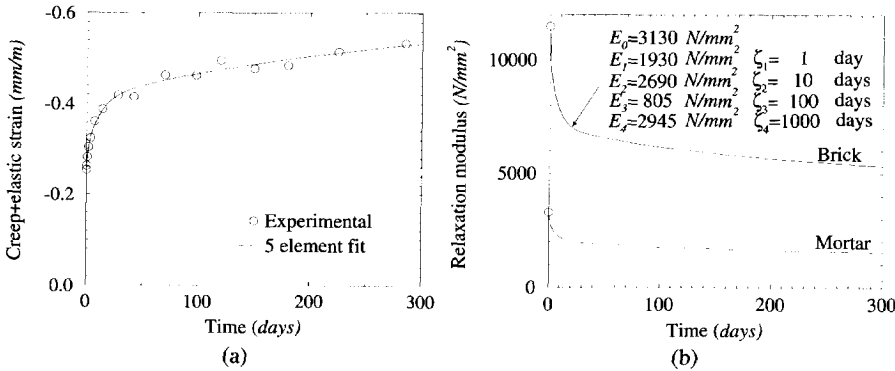


Figure 7.3: (a) Measured creep and fitted five-element Dirichlet function. (b) Relaxation function derived from (a).

mens and approximated the basic creep ϵ_c , i.e. creep on non-drying specimens, by subtracting the free shrinkage ϵ_s and elastic strains ϵ_e as follows:

$$\epsilon_c = \epsilon - \epsilon_e - \epsilon_s \quad (7.1)$$

with ϵ the total strain measured on the transient creep specimens and ϵ_s the total strain measured on the drying, non-loaded specimens. This method ignores not only the influence of the stress level on the shrinkage strain, but also the influence of cracking due to eigenstressing in the free shrinkage specimens. Nonetheless, these data are used for a first estimate of the bulk creep parameters here.

Nearly equal creep coefficients, defined as

$$\phi_c = \frac{\epsilon_c}{\epsilon_e}, \quad (7.2)$$

were reported for the CS-block and CS-brick specimens. Therefore, equal creep coefficients are assumed for the bricks, blocks, as well as the mortar. This means that the same relaxation times ($\zeta_1, \zeta_2, \dots, \zeta_N$) are used for both constituents and, once the Maxwell spring stiffnesses (E_1, E_2, \dots, E_N) have been found for one constituent, those for the other are obtained by mere factorisation:

$$E_{n,m} = \frac{\sum_{n=1}^N E_{n,m}}{\sum_{n=1}^N E_{n,b}} E_{n,b} = \frac{E_m}{E_b} E_{n,b} \quad (7.3)$$

where the subscripts m and b refer to mortar and brick respectively. Aging is not considered, despite evidence of masonry compressive creep aging (Shrive et al. 1997).

The measurement of true shrinkage, i.e. the volume reduction of a material element at zero stress, is virtually impossible, hampered by the slow drying process in cementitious materials which causes humidity gradients, eigenstresses and cracking. Furthermore, tests by Alvaredo et al. (1995) indicate that for cement paste of various water/cement (w/c) ratios, the coefficient depends on the relative humidity, as will be discussed in detail in section 7.4.2. As a first approach constant shrinkage coefficients are assumed. If, in addition, one ignores the influences of cracking and stress-dependence of shrinkage ($r = 0$ in eq. 3.43a), the coefficients can be estimated from the "final" shrinkage strain (ϵ_s^∞). This is done by solving the differential equation (3.43a) with initial condition $\epsilon_s(0) = 0$:

$$\epsilon_{s,i} = \alpha_s P_i (h - h_o) \quad (7.4)$$

and substituting ϵ_s^∞ and environmental humidity (h_E) as follows:

$$\alpha_s P_i = \frac{\epsilon_s^\infty}{(h_E - h_o)}. \quad (7.5)$$

The shrinkage parameters calculated in this manner are listed in Table 7.3. Note that, due to the absence of separate shrinkage data for the mortar and the bricks, the coefficients derived from the masonry data are assumed and employed for each constituent in the discrete analyses.

The coefficients which reflect the apparent stress dependence of shrinkage, r_s , eq. (3.43a, 3.44a), should be determined by performing simultaneous *transient creep*, *basic creep*

and *free shrinkage* tests. The discrepancy between transient creep on the one hand and the superposition of basic creep and free shrinkage on the other hand, quantifies r . In the absence of such data, these coefficients are set to zero.

7.1.2 SPATIAL AND TIME DISCRETISATION

It is well known that care should be taken with spatial and time discretisation, with regard to the numerical solution of both the diffusion equation and the mechanical behaviour. To avoid numerical *overshoot* of the pore humidity, time steps should be not too small, while the elements should be small close to surface and other phase boundaries. At the same time step sizes should be limited to avoid large humidity-time gradients. Here, time steps are chosen to restrict increments in humidity to $\Delta h \approx 0.025$. This gives time steps for the diffusion analyses of one half hour initially and up to 20 days towards the end of the test period (200-300 days). For the mechanical analyses the time steps are roughly one quarter of those for the diffusion analyses to ensure accuracy and to avoid convergence problems.

The spatial discretisation is equally important. The overshoot is attenuated by a too coarse mesh. The non-smoothness of the diffusion equation coefficients contributes to the requirement for dense FE meshes, (Van Zijl 1999b). Furthermore, by intelligent discretisation in areas of large shrinkage strain gradients, i.e. in the thickness direction, the gradient per element can be minimised, ensuring the most accurate representation of the stress and strain fields for a given mesh density. This is illustrated by Figure 7.4, where the pore humidity evolution is shown at points through the specimen thickness for uniform, Figure 7.4a, and nonuniform discretization, Figure 7.4b, through the thickness. In the nonuniform case element sizes in the thickness direction increase with a factor two from the surface inwards.

specimen	α_s	P_x	P_y	P_z
CS-block	0.000525	1.0	1.2	1.0
CS-brick	0.0007	1.0	1.08	1.0

Table 7.3: Shrinkage coefficients derived from final shrinkage strain values of masonry shrinkage specimens.

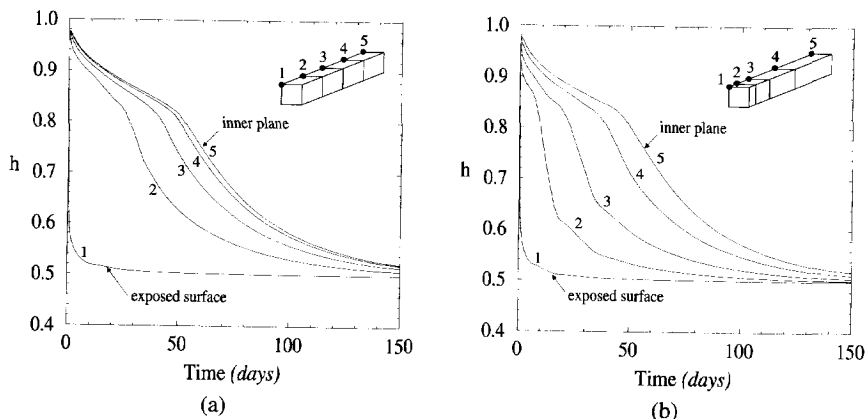


Figure 7.4: Humidity evolution at points through the masonry specimen thickness for (a) uniform and (b) nonuniform spatial discretisation in the thickness direction.

7.1.3 BOUNDARY CONDITIONS AND INITIAL VALUES

The experiments were conducted in a controlled climate of 50% humidity and 20°C. For a zero air flow velocity a surface convection transfer coefficient (3.12) of $\beta = 0.025 \text{ s}/\mu\text{m}$ is appropriate (Tammes and Vos 1984). This gives a film coefficient of:

$$\beta = \frac{\beta^* p_s}{\rho_l} = \frac{0.025 \cdot 10^{-6} \times 2338}{1000} = 0.058 \mu\text{m/s or } 5 \text{ mm/day}$$

The calcium silicate bricks and blocks were pre-wetted to a moisture content of between 6% and 8% by weight, according to standard building procedure for this material (Van der Pluijm and Wubs 1996). The total weight was measured at each time of shrinkage and creep strain measurement. After the experiments the dry weight of the specimens was measured, enabling the average moisture content at any time during the experiment to be calculated. In this manner the initial moisture content in the CS-block and CS-brick specimens was calculated to be 6.5% and 8.0% respectively. To convert the initial moisture content to initial pore humidity two assumptions need to be made. Firstly, the interfaces between brick and mortar are assumed to be hydraulically perfect, meaning that the pore humidity is continuous across them. Secondly, the pore humidity is assumed to be uniform initially in the mortar and bricks in each specimen. This initial value can then be calculated which, by considering the respective hygroscopic curves, corresponds with the total initial moisture content. This calculation leads to $h_o = 0.96$ for the CS-block

specimen and $h_o = 1.0$ for the CS-brick specimen.

7.2 Shrinkage and transient creep response

7.2.1 LARGE BLOCK (CS-BLOCK) SPECIMEN RESPONSE

Figures 7.5a-d show the numerical pore humidity contours at various stages of drying of the CS-block specimen. Good agreement is obtained with the measured moisture content in time, Figure 7.5e.

By inspection of the humidity contours, it can be seen that the exposed surface is nearly in equilibrium with the environment after one day. However, due to the low diffusivity the bulk of the specimen remains saturated, causing large gradients through the depth, especially close to the exposed surface. The gradients gradually reduce until equilibrium is reached with the environment after about 100 days of drying.

Figures 7.6a-d show the maximum principal eigenstresses accompanying the hygral gradients in the free drying specimen. In the early stages high tensile stresses occur at the surface, causing initiation of debonding. The brick strength (2 N/mm^2) is also slightly exceeded in the brick faces, so that some drying cracks could initiate and grow there, but this fact is ignored in our modelling strategy. As time passes the peak stresses reduce along with the hygral gradients until a virtually (eigen)stress-free state is reached after 100 days. Note that the deformations have been scaled up by a factor of 1000. The maximum crack width is in the order of $7 \mu\text{m}$, reached after ten days.

Figure 7.6e shows that reasonable agreement is obtained between the measured and numerical average strains in the gauge length in the x direction, as well as in the y direction. The dashed line shows the numerical result if the debonding at the interfaces is not modelled.

When a vertical (y-direction) compressive creep pressure of -2.5 N/mm^2 is applied simultaneously in order to simulate the transient creep experiment, the tensile eigenstresses are offset sufficiently to prevent cracking. In Figure 7.7 the numerical transient and basic creep strains are compared with the experimental data. The basic creep is obtained by subtracting the free shrinkage strain, Figure 7.6e, from the total strain in the gauge length on the transient creep specimen. Note that the creep experiments were only performed in the y-direction.

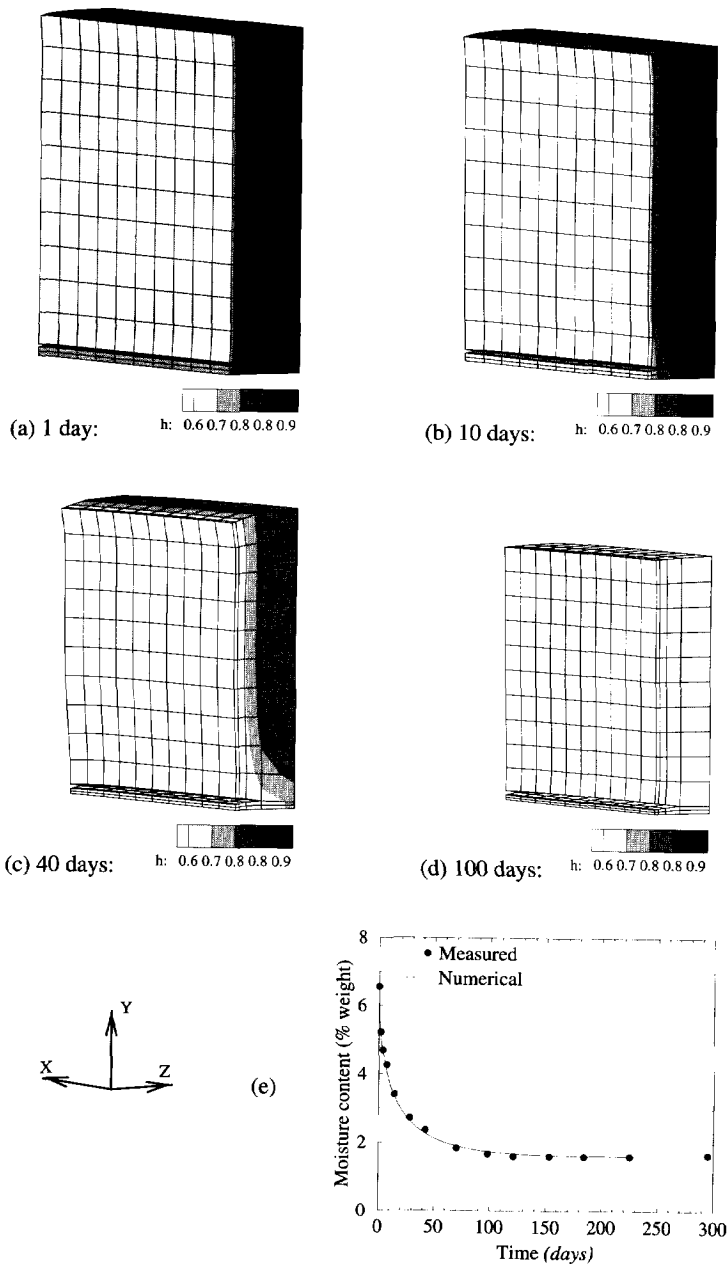


Figure 7.5: (a-d) Pore humidity contours and (e) moisture content (% by weight) evolution in drying single joint calcium silicate (CS-block) specimen.

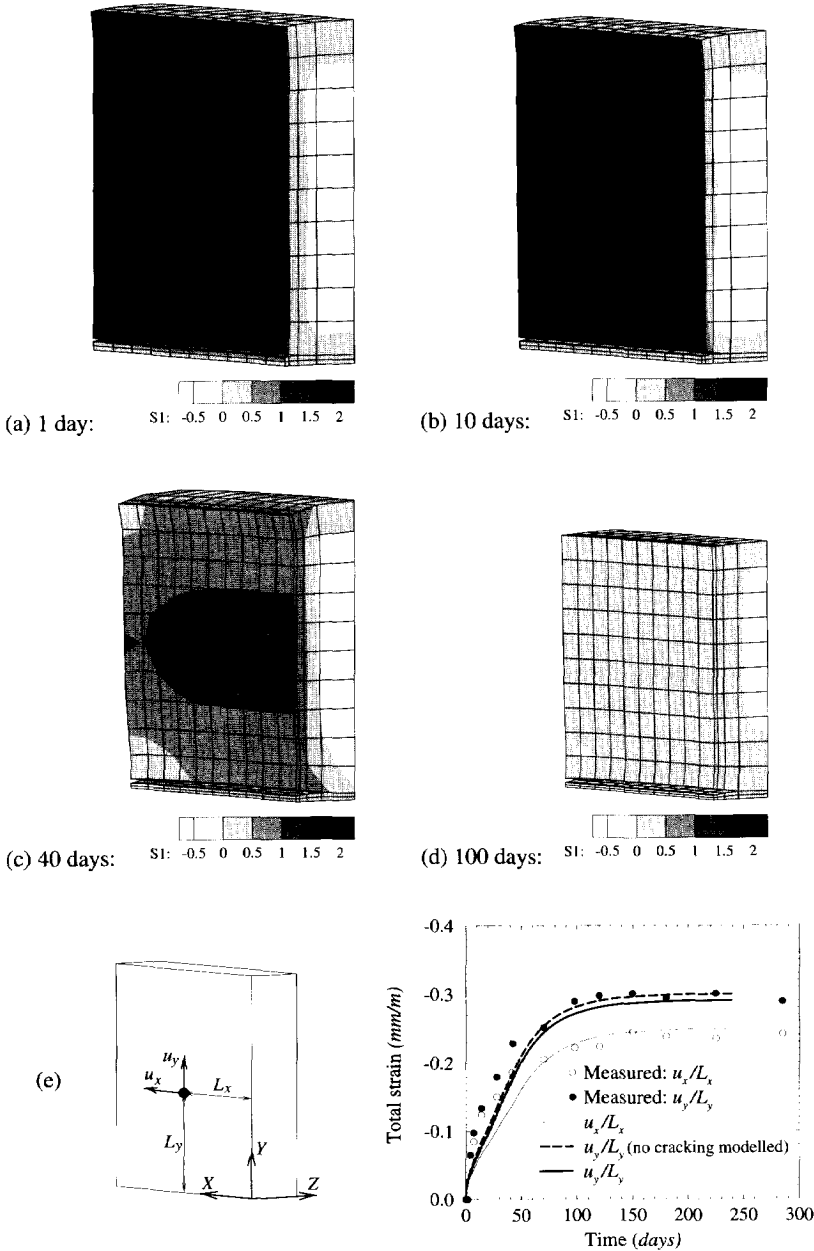


Figure 7.6: (a-d) Contours of maximum principal stress (N/mm^2) and (e) total strain in the gauge length in free drying single joint calcium silicate (CS-block) specimen.

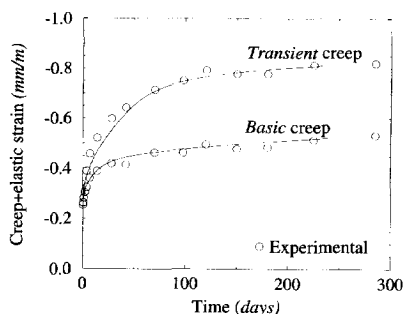


Figure 7.7: CS-block transient and basic creep response.

7.2.2 SMALL BRICK (CS-BRICK) SPECIMEN RESPONSE

7.2.2.1 Assumed moisture migration parameters

It is well known that the calcium silicate blocks and the small bricks exhibit quite different behaviour (Van der Pluijm and Wubs 1996). In the above section it has been shown that the parameters taken from Pel (1995) give reasonable agreement with the CS-block measured moisture loss and shrinkage response. This is not so for the CS-brick specimen. Having no experimental data for this specimen, the Pel (1995) parameters are simply modified to obtain better agreement to allow subsequent comparison of the experimental and numerical shrinkage and creep responses. Firstly, the desorption curve is adjusted, Figure 7.8a, to give the same residual moisture content (2% by weight) in the CS-brick specimen at the environmental humidity (50%) as measured by Van der Pluijm and Wubs (1996). Secondly, the diffusion coefficient is taken as one tenth of the measured value, Figure 7.8b, to fit the drying rate better.

7.2.2.2 CS-brick response for the assumed moisture migration parameters

In Figure 7.9 the hygral response of the CS-brick specimen is summarised. Figure 7.9e shows the significant difference in the measured moisture content evolution between the CS-block and CS-brick specimens. Also, the numerical responses with and without the modifications to the model parameters have been drawn. A large discrepancy is found if the differences in hygral properties are ignored between the small brick and large block calcium silicate units.

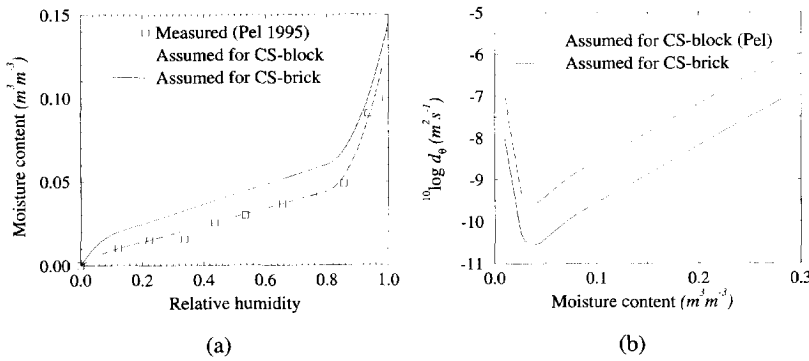


Figure 7.8: Assumed (a) desorption curve and (b) diffusion coefficient for the CS-brick specimen.

Also shown in Figure 7.9 are the pore humidity profiles at various stages of drying. After one day large gradients exist through the depth close to the exposed surface. Large humidity gradients also occur between the mortar and bricks, due to the different hygroscopic relations of the two constituents. Because of the higher diffusivity, the mortar dries quicker than the bricks, yet the pore humidity in the mortar reduces at a lower rate. The gradients reduce until equilibrium is reached with the environment after about 100 days of drying.

Figures 7.10a-d show the maximum principal eigenstresses accompanying the hygral gradients. In the early stages high tensile stresses occur at the surface, causing initiation of debonding. The brick strength ($2 N/mm^2$) is also slightly exceeded in the brick faces, so that drying cracks could develop there, but this fact is ignored in our modelling strategy. As time passes the peak stresses reduce along with the hygral gradients until a virtually (eigen)stress-free state after 100 days. Note that the deformations have been scaled up by a factor of 500. The maximum crack width is in the order of $7 \mu m$, reached after ten days.

Figure 7.10e shows that reasonable agreement is obtained between the measured and numerical average strains in the gauge length in the x direction, as well as in the y direction. If the debonding at the interfaces is not included in the model, a significantly larger shrinkage, the dashed line in Figure 7.10e, is obtained in the y direction, where 3 delaminating interfaces are included in the gauge length. As the shrinkage parameters have been estimated ignoring the influence of cracking, the uncracked numerical response represents the experimental response well.

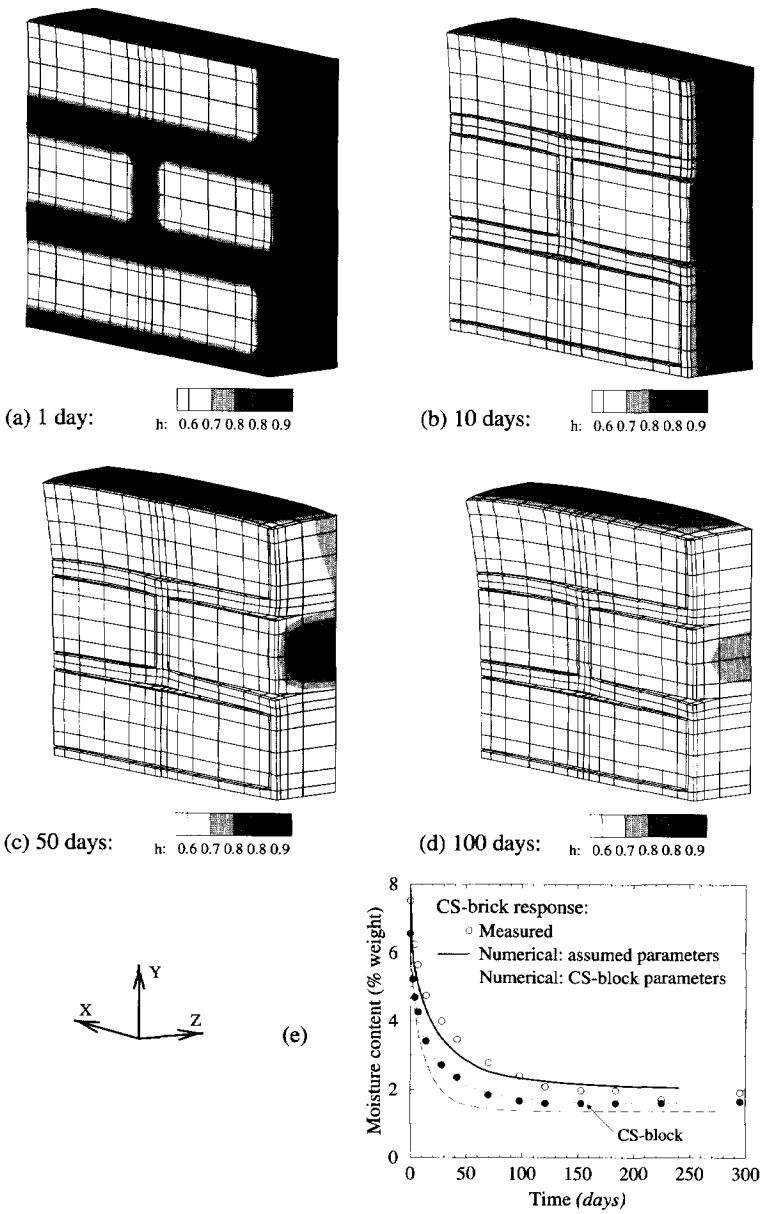


Figure 7.9: (a-d) Pore humidity contours and (e) moisture content (% by weight) evolution in drying CS-brick specimen.

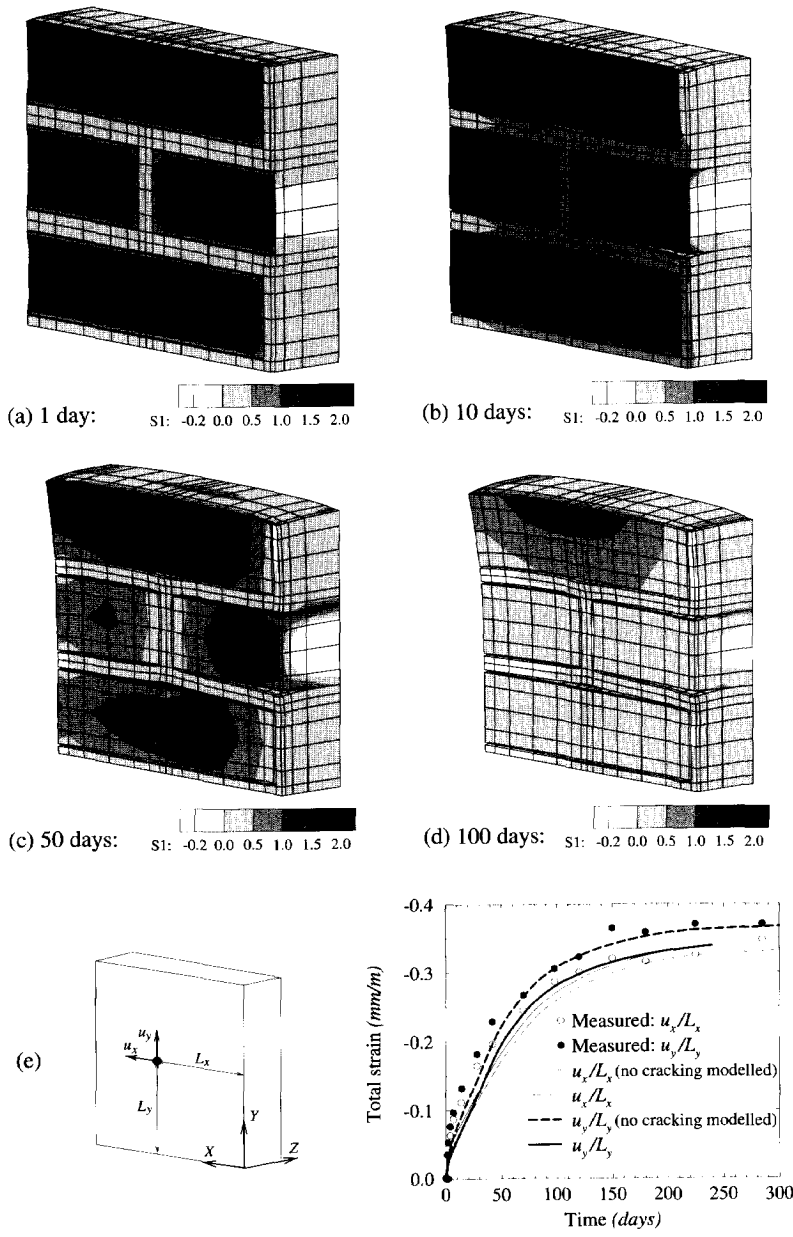


Figure 7.10: (a-d) Contours of maximum principal stress (N/mm^2) and (e) total strain in the gauge length in free drying CS-brick specimen.

The response to the 2.5 N/mm^2 compressive creep load is shown in Figure 7.11, where the deformations have been scaled up with a factor of 375. Splitting is initiated along the vertical interfaces in response to the creep load, which is assumed to be applied linearly over a period of 5 minutes. Subsequently the superimposed eigenstresses cause the splitting cracks to open wider, while the debonding along the horizontal interfaces seen in the case of the free drying CS-brick specimen is prevented by the compressive creep load. The basic creep strains are obtained by subtracting the free shrinkage strain, Figure 7.10e, from the total strain in the gauge length on the transient creep specimen, Figure 7.11e.

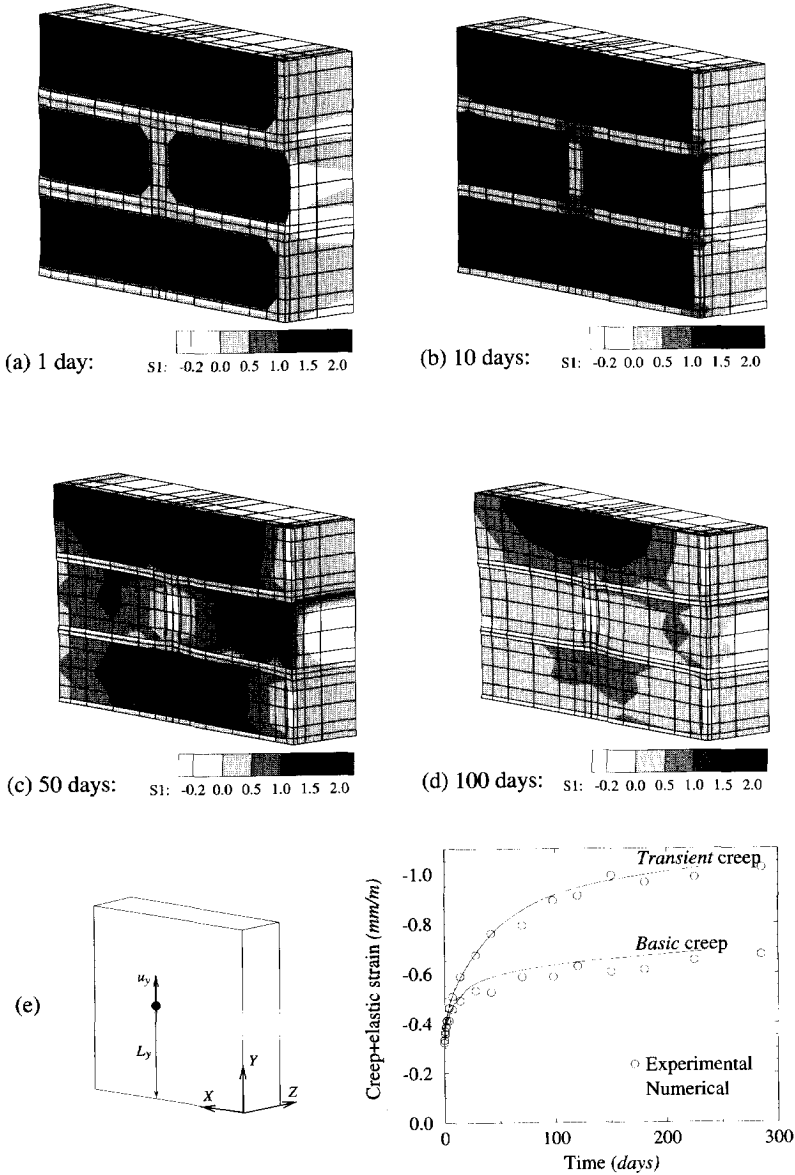


Figure 7.11: (a-d) Contours of maximum principal stress (N/mm^2) in CS-brick transient creep specimen. (e) Total strain (y direction) in the gauge length in CS-brick creep specimen subjected to shrinkage (transient creep) and with free shrinkage subtracted (basic creep).

7.3 Mesh objectivity

The free shrinkage CS-brick specimen has been analysed with the three meshes shown in Figure 7.12. The global behaviour, as reflected by total moisture content (by weight) and total strain, as calculated from the total displacement at the gauge point at the surface, see for example Figure 7.11e, is shown in Figure 7.13. The response converges with mesh refinement.

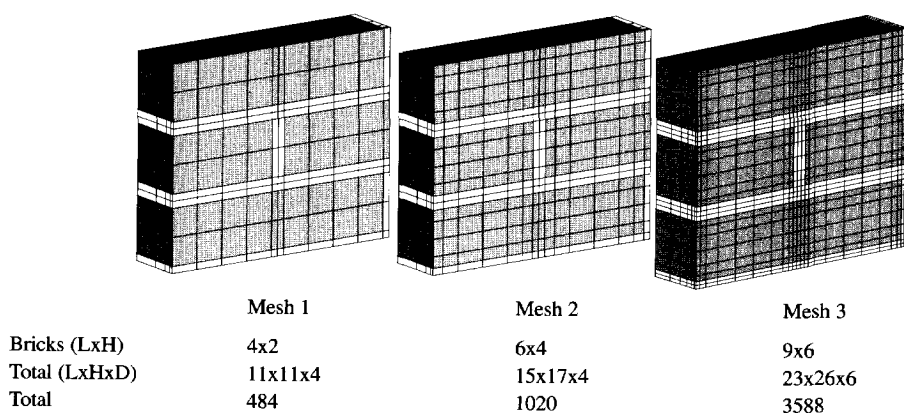


Figure 7.12: Finite element meshes employed to investigate mesh objectivity of the numerical simulation of the CS-brick shrinkage specimen.

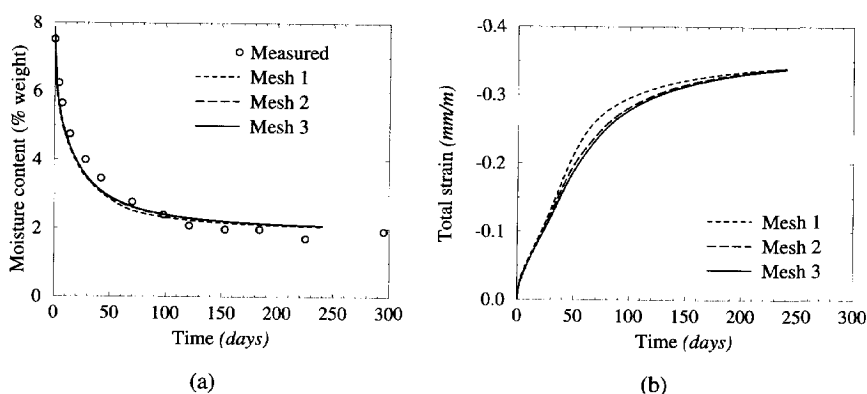


Figure 7.13: (a) Moisture content (% by weight) and (b) total strain in the gauge length for the three meshes employed, Figure 7.12.

Furthermore, oscillating stress fields may occur when employing the same interpolation order for pore humidity and displacement, as has been done in the above analyses. This is because the linear shrinkage strain variation in each eight-noded brick element obtained from the diffusion analysis, has to be represented by the constant strain capacity of this element in the mechanical analysis. However, in the three-dimensional analyses performed here, equal-order interpolation of pore humidity and displacements produces compatible strain fields in the orthogonal directions. For instance, the normal strain component ϵ_x is constant in the x-direction, but linear in the orthogonal directions in the eight-noded brick. To verify that a multi-dimensional analysis with equal-order interpolation does indeed cause less pronounced disturbance in the stress fields, the CS-brick free shrinkage case has been re-analysed with mesh 2, but employing twenty-noded bricks. In terms of contours of principle stresses no significant difference between the linear element and quadratic element results has been found. A more detailed study of stress component fields should be performed to investigate the existence and extent of stress oscillations. However, the global deformational response matches the eight-noded mesh 2 response, Figure 7.12, with an insignificant improvement in the early stages. To avoid excessive computational effort mesh 2 with eight-noded elements has been employed for all the CS-brick analyses reported.

7.4 Sensitivity study

Having only experimental data on the meso-scale available for estimation of the model parameters, some quantification of the sensitivity to the estimation error is required.

7.4.1 MOISTURE CONTENT DEPENDENCE ON SURFACE CONVECTION COEFFICIENT

The film coefficient β is dependent mostly on wind speed and surface roughness. As mentioned in section 7.1.1.1 a coefficient of 5 mm/day has been assumed to simulate the zero wind velocity in the experimental environment. To evaluate the sensitivity to this parameter, two extreme cases were analysed additionally, namely for $\beta = 0.5$ and $\beta = \infty \text{ mm/day}$. The infinite film coefficient is modelled by setting the surface humidity equal to the environmental humidity. In Figure 7.14 the evolution of the total moisture content by percentage of weight is shown for the three cases. The global drying response is clearly insensitive to the film coefficient, but, a finite value sufficiently slows down surface drying to prevent overshoot near the surface (Van Zijl 1999b).

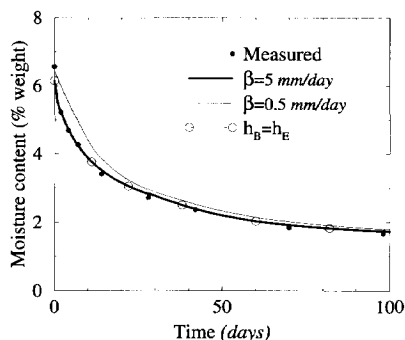


Figure 7.14: Influence of surface convection coefficient on masonry moisture content.

7.4.2 SHRINKAGE COEFFICIENT DEPENDENCE ON HUMIDITY

As discussed in section 7.1.1.2, a constant coefficient of shrinkage α_s has been estimated from the “final” shrinkage strain obtained from the drying tests. However, a strong dependence on the relative humidity has been reported by Alvaredo et al. (1995). Their tests indicate that for cement pastes of various water/cement (w/c) ratios, the coefficient depends on the relative humidity, as summarised in Table 7.4. To study the sensitivity of masonry shrinkage to the variation of α_s with humidity, also a linear and a parabolic relation have been employed. The relations reflect the “final” shrinkage strain, as derived from:

$$\int \dot{\epsilon}_s dt = \int \alpha_s(h) h dt + \text{constant} \quad (7.6)$$

with

	$\alpha_s (\times 10^{-3})$	
	w/c=0.4	w/c = 0.5
$0.75 < h < 1.00$	1.5	2.3
$0.60 < h \leq 0.75$	0.7	0.2
$0.45 < h \leq 0.60$	0.1	0.5

Table 7.4: Shrinkage coefficients derived from final shrinkage values of cement pastes at different environmental humidities (Alvaredo et al 1995).

$$\alpha_s(h) = \begin{cases} a \\ a h \\ a h^2 \end{cases} \Rightarrow a = \begin{cases} \frac{\epsilon_s^\infty}{h_E - h_o} \\ \frac{2\epsilon_s^\infty}{h_E^2 - h_o^2} \\ \frac{3\epsilon_s^\infty}{h_E^3 - h_o^3} \end{cases} \quad (7.7)$$

Figure 7.15 shows that better agreement is obtained with the measured shrinkage when considering humidity dependence of the shrinkage coefficient.

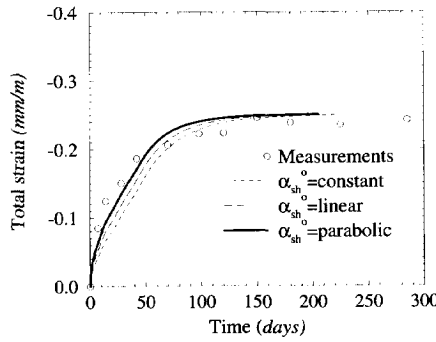


Figure 7.15: Influence of shrinkage coefficient dependence on humidity on free shrinkage.

7.4.3 PICKETT EFFECT

No experimental data are available from which the shrinkage stress-dependence coefficients r_x, r_y and r_z in eq. (3.44a) can be estimated. They have been shown to be in the range $0.2/f_t \leq r_i \leq 0.8/f_t$ for concrete (Bažant and Chern 1985). The CS-block specimen is re-analysed for the two extreme, isotropic cases. Figure 7.16a shows the free shrinkage strain distribution through the thickness at the gauge point after 30 and 120 days of drying. The corresponding vertical stress components are shown in Figure 7.16b, revealing a relaxation effect of the stress-dependence coefficient. Whereas cracking is expected also in the blocks and bricks for $r_i f_t = 0$ (sections 7.2.1, 7.2.2.2), the maximum coefficient ($r_i f_t = 0.8$) reduces the stresses to within the calcium silicate block and the small brick

tensile strength. However, it has only an insignificant influence on the observed strain of both the free drying CS-block and CS-brick specimens. When the creep load acts, a significant influence is seen, Figure 7.17. The total compressive strain is increased by up to 30%, which means that, if such a dependence does exist, the experimentally measured basic creep is overestimated, because it contains the stress-dependent shrinkage strain component not reflected by the free shrinkage. Only by testing similar, but non-drying creep specimens the error can be quantified.

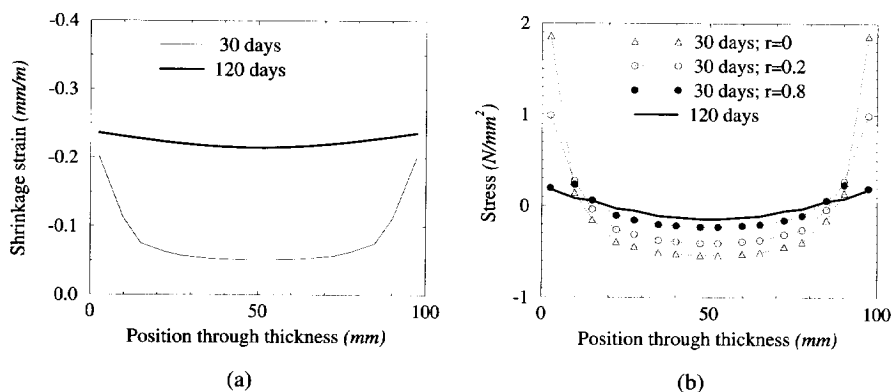


Figure 7.16: (a) "Free" shrinkage evolution and (b) stress distribution through the thickness at the gauge point in the CS-block specimen.

7.4.4 CREEP/RELAXATION

A variation in the creep modelled is obviously directly translated into increased or decreased total deformation in creep analyses. However, if the free shrinkage response is sensitive to the assumed creep parameters, an inverse process of parameter determination becomes more difficult. To investigate this sensitivity, both CS-block and CS-brick specimens are re-analysed with no bulk creep. The case of $r = 0$, i.e. zero Pickett effect, is chosen. Figure 7.18 shows the influence of bulk creep on the free drying shrinkage. If bulk creep is included in the model, a significantly larger total vertical deformation is found at the gauge point (CS-block +3%, CS-brick +9%), but a decrease in maximum crack width is computed (CS-brick, from $8.7\mu\text{m}$ to $7.5\mu\text{m}$). Also, the maximum principal stress is relaxed by up to 20% in CS-block and 12% in CS-brick.

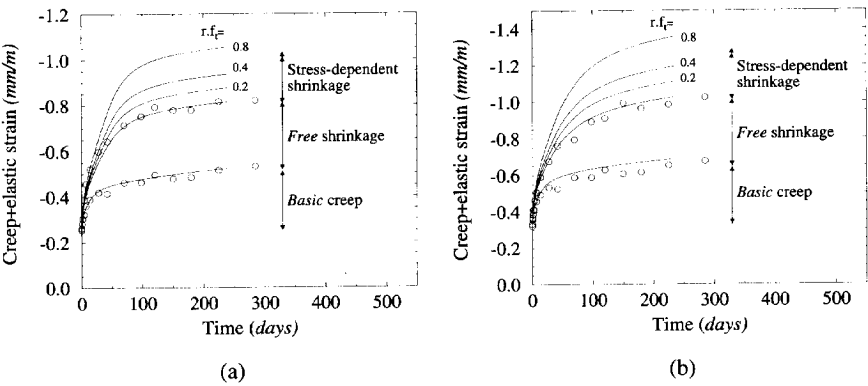


Figure 7.17: Illustration of Pickett-effect in (a) CS-block and (b) CS-brick creep specimen.

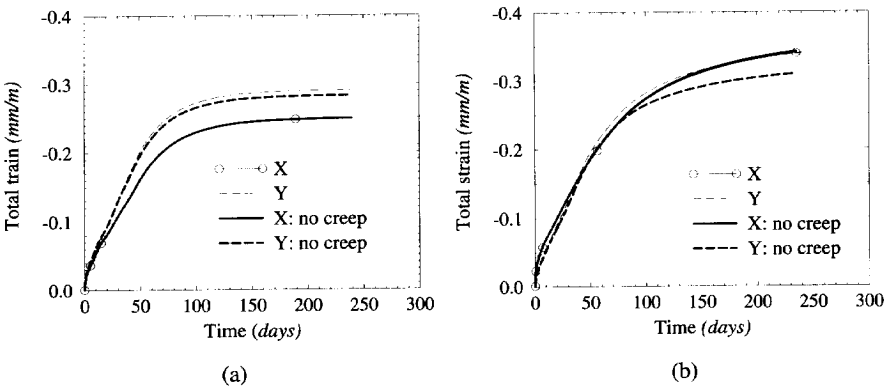


Figure 7.18: Influence of bulk creep on (a) CS-block and (b) CS-brick masonry free shrinkage.

7.5 Discussion

From the numerical results presented in the above sections it is clear that the model parameters for time dependent behaviour cannot be derived directly from the available experimental data. The good agreement obtained with the measured moisture loss in the CS-block specimen can be considered as coincidental, because the moisture migration parameters were obtained from measurements by a different research group on sand-lime material not unlike the blocks in the CS-block specimens, but probably subjected to a different manufacturing process. This argument is strengthened by the large difference in moisture loss evolution found for the CS-brick specimen when employing the same (CS-block) diffusion and hygroscopic parameters. Experimental determination of these material parameters for the large block and small calcium silicate units is necessary. Also, the moisture migration in the mortar taken from CS-block and CS-brick type specimens should be characterised experimentally, because, although exactly the same mortar is used for manufacturing CS-block and CS-brick, the units strongly influence the properties of the cured mortar.

With regards to the mechanical behaviour, the difficulty in deriving the material parameters from the experimental data is due to the tests being carried out on the meso scale and, even more importantly, not carefully designed to distinguish between the various mechanisms. No information about stress-induced shrinkage (ϵ) can be derived from the data. It has been argued in section 7.4.3 that this leads to an overestimation of the basic creep if derived by subtracting the free shrinkage strain from the (compressive) transient creep. This is illustrated in Figure 7.19. Note that, for the purpose of illustration, the lower limit of $r = 0.2/f_i$ published for concrete has been employed to analyse the transient creep response. The stress-induced shrinkage should be subtracted to obtain a better estimate of the basic creep.

An additional source of error is also unveiled in the figure. Cracking reduces the material (stress-free) shrinkage in the free drying specimen, but does not occur in the creep specimen, the tensile stresses being offset sufficiently by the creep load. This effect should also be quantified to derive the basic creep. It can be done numerically by comparing the numerical results of the free shrinkage specimen with the response if the cracking criterion is ignored, i.e. no cracking is modelled. However, also in these analyses the basic creep modelled influences the response significantly, Figure 7.18 section 7.4.4, calling for an inverse approach.

Two alternative ways can be followed to find better approximations of the model parameters. The first involves an iterative numerical approach of adjustment of the model

parameters and re-analysis until a satisfactory agreement between the numerical and experimental results has been obtained. In the above sections only the first iteration has been done. The second iteration would involve selection of:

- an increased shrinkage coefficient to allow for the reduction of the free shrinkage strain caused by cracking,
- smaller bulk creep, by selecting increased stiffnesses for the Maxwell elements, to allow for stress-induced shrinkage in the transient creep specimen and cracking in the free shrinkage specimen.

However, information about the stress dependence of shrinkage is lacking. Also, the moisture migration in the different comprising materials must be characterised, calling for a new set of experiments. This causes the second approach, a carefully designed experimental program, which addresses all known mechanisms, to be favoured. Such a program is proposed in Van Zijl (1999b).

Here, tensile creep is of importance. In tensile creep tests cracking may occur in all three specimens (the free shrinkage, basic creep and transient creep specimens), but to a varying degree. It is possible to design the experiments and specimens that avoid cracking in the gauge area (Van Zijl 1999b). Bazant and Xi (1993) have proposed bending experiments from which results the contribution of cracking can be distinguished. However, bending tests introduce additional difficulties, especially when dealing with masonry.

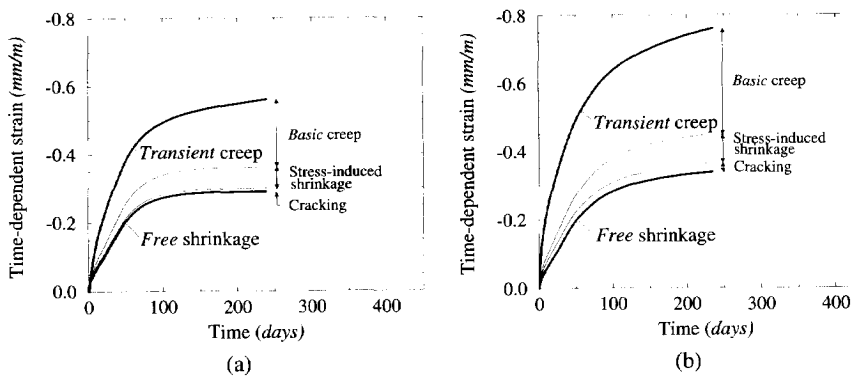


Figure 7.19: Determination of basic creep for (a) CS-block and (b) CS-brick masonry.

Chapter 8

MASONRY WALLS UNDER RESTRAINED SHRINKAGE

Moving away from the verifying and validating analyses of small to medium size laboratory specimens, large masonry walls are analysed in this chapter. In particular, walls subjected to drying, but restrained at the base by a non-shrinking foundation are studied. This choice is motivated by the wide-spread occurrence of unsightly and, in some cases, serviceability impairing cracks in masonry buildings in The Netherlands, due to restrained shrinkage (De Jong 1992). Limited measurement data exist (Berkers and Rademaker 1992), but the quantitative verification of the numerical results is frustrated by the lack of experimental data from which the material/model parameters can be characterised, a matter addressed in the previous chapter. Also, the need for three-dimensional analysis to capture the moisture gradient-induced eigenstressing and associated cracking renders the quantitative verification unviable. This *internal* restraint to shrinkage and the initial damage it causes may significantly reduce the resistance to the *external* restraint. Instead, the focus is on a qualitative study to gain insight in the wall response to the external restraint through two-dimensional analyses. The ability of the numerical model to capture the initiation and propagation of the primary and secondary cracks realistically is demonstrated. Finally, it is shown that the objectivity of the numerical response in terms of an unique crack spacing and alignment irrespective of the finite element type and size, requires the inclusion of the viscosity of the cracking process.

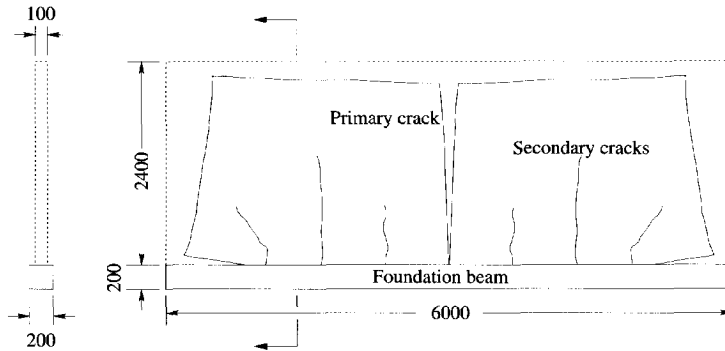


Figure 8.1: Observed crack pattern in base-restrained shrinkage wall. Dimensions in *mm*.

8.1 Modelling approach

The single leaf wall shown in Figure 8.1 is modelled as a two-dimensional, homogeneous plane, in a compromise between computational accuracy and viability. A plane stress formulation is adopted, which captures the response to mechanical in-plane actions accurately (Rots 1994, Lourenço 1996). By employing the anisotropic Rankine yield criterion, section 5.2, the different strengths and softening characteristics of masonry in the direction normal and parallel to the bed joints are accounted for. However, this is the only representation of the microstructure, here to be understood as the two constituents of masonry and their arrangement in the wall, as a detailed representation of the stress and strain fields in the wall is not possible. Yet, this modelling strategy has been shown to reasonably capture the global behaviour of masonry structures, which are subjected to in-plane, mechanical actions (Lourenço 1996). With regard to drying shrinkage, the conclusion was made in the previous chapter that only a three-dimensional representation of the wall can capture the moisture gradients and associated *internal* restraint, which causes the eigen-stressing and debonding at the interfaces between the constituents. The influence of such “initial”, three-dimensional cracking, which is neglected in the two-dimensional model, on the resistance to the *external* restraint has not yet been investigated. However, a simple way of accounting for the partial debonding is to employ a reduced tensile strength in the two-dimensional analysis. Often, the tensile strength is measured on specimens which have been allowed to dry to a particular relative humidity. In these cases, the measured strength already reflects the reduced, average strength.

Only one half of the wall is modelled, because of symmetry. Both the wall and the foundation beam are modelled as homogeneous continua with four-noded quadrilateral ele-

ments. Four-noded interface elements are employed to model the interface between the foundation and the wall. The dimensions are shown in Figure 8.1.

8.1.1 MOISTURE MIGRATION ANALYSIS

The wall faces are assumed to be exposed to the environment. This causes a dilemma in the light of the two-dimensional modelling strategy, because in a large, thin wall the moisture flux is essentially normal to the wall plane. However, by the following reasoning the drying process can be modelled in a simple way. For low diffusivity, a moisture content gradient will exist in that direction before hygral equilibrium is reached with the environment. Thereby the surface convection at the wall face is delayed. If, however, the diffusivity is sufficiently high, the surface convection governs the drying process (Van Zijl 1999b). A wall fabricated of such material can be modelled as a plane. As in the three-dimensional models of the previous chapter, plane interfaces parallel to the wall plane capture for the out-of-plane surface convection. The model of the drying process can be simplified even more, if one assumes equal surface convection properties for the masonry constituents and ignores the spatially random nature of the material properties and the environmental humidity. The former is not so far-fetched, keeping in mind that the film coefficient is mainly dependent on the wind speed (Tammes and Vos 1984). The latter has no implication for the main focus of gaining insight into externally restrained masonry wall behaviour. With these assumptions, the moisture content, or the pore humidity is spatially uniform. This justifies the homogeneous representation of the wall, but also renders numerical analysis for determining the pore humidity evolution unnecessary. This can be seen by inspection of eqs. (4.6,4.7) which, in one dimension and for the case of surface convection domination, reduce to

$$c L_d \dot{h} + 2 \beta h = 2 \beta h_E, \quad (8.1)$$

with L_d the wall thickness. After solution of this differential equation, with the initial uniform pore humidity h_o , the pore humidity evolution

$$h = h_E + (h_o - h_E) e^{-2 \frac{\beta t}{c L_d}} \quad (8.2)$$

is found, which occurs at each point in the wall. This equation is shown in Figure 8.2 for $c = 1$, $L_d = 100 \text{ mm}$, $\beta = 5 \text{ mm/day}$, $h_o = 1.0$ and $h_E = 0.6$.

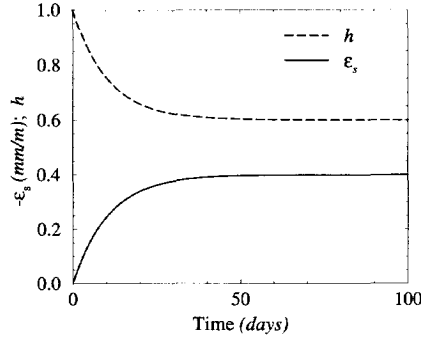


Figure 8.2: Humidity and free shrinkage strain in the wall.

Since no experimental data exist from which to calculate the coefficients of the matrix of stress-induced shrinkage \mathbf{r}_s , eqs. (3.43,3.44), they are set to zero. Isotropic shrinkage is assumed ($\mathbf{P}_s = [1 \ 1 \ 0]$). For this case the shrinkage strain is given by, cf. eqs. (3.43,8.2):

$$\epsilon_s = \alpha_s (h_E - h_o) \left(1 - e^{-2 \frac{\beta t}{c L_d}} \right). \quad (8.3)$$

This evolution is also shown in Figure 8.2 for $\alpha_s = 0.001$ and is assumed to act at each point in the wall.

8.1.2 MECHANICAL ANALYSIS

Apart from the drying shrinkage, the own weight and an in-plane load of eight times the own weight, which bears on the upper edge of the wall, are modelled. To capture the crack initiation and propagation in the wall, the Rankine plasticity formulation is employed. Material parameters typical for calcium silicate masonry are chosen, Table 8.1. Tensile strengths and fracture energies that are 10% higher than those tabulated are employed for the wall away from the central column of elements in order to simulate material property variation in a simple way and to fix the primary crack location.

The interface elements between the base and the wall obey the interface material model outlined in section 5.1.1. The model parameters employed are given in Table 8.2. Note

that due to the lack of experimental data a constant dilatancy angle, $\tan \phi = 0.2$, is employed. This choice facilitates wall cracking, instead of mere shear slipping along the bottom joint upon differential shrinkage. The foundation beam has a Young's modulus $E = 30000 \text{ N/mm}^2$ and a Poisson's ratio $\nu = 0.2$.

The Maxwell chain is activated to capture the bulk creep, as it is incorporated in the constitutive model, section 3.2.1. Because of the lack of tensile creep measurements, a typical compressive creep behaviour of calcium silicate masonry (Van der Pluijm and Wubs 1996) is employed for the least-squares fitting of a five-element Kelvin-Voigt chain, Figure 8.3a. For the same reason aging is not considered, despite evidence of masonry compressive creep aging (Shrive et al. 1997). By a constant strain analysis the five-element Maxwell chain shown in Figure 8.3b is derived. Initially no cracking rate term is included ($m=0$ in eq. (5.55)). Instead, a crack band width l_m , eq. (5.56), is assumed to be related to the area of an element (Feenstra 1993, Lourenço 1996) to achieve a mesh-objective energy dissipation.

8.2 Base-restrained shrinkage response

In the analyses, the wall is subjected the shrinkage evolution of Figure 8.2, while accounting for creep and cracking. The crack patterns and the maximum primary crack width development with the free shrinkage evolution are shown in Figure 8.4. Some limited debonding occurs at the foundation beam interface. The Coulomb-frictionally enhanced shear resistance, which is caused by the top load, prevents shear-slipping there.

Different finite elements and mesh densities have been employed to discretise the wall,

E $\frac{N}{mm^2}$	ν	f_{tx} $\frac{N}{mm^2}$	f_{ty} $\frac{N}{mm^2}$	G_{ftx} $\frac{N}{mm}$	G_{fty} $\frac{N}{mm}$	α_τ
5000	0.2	0.4	0.3	0.04	0.02	1.0

Table 8.1: Masonry wall mechanical material parameters employed.

f_t $\frac{N}{mm^2}$	G_f^I $\frac{N}{mm}$	c_o $\frac{N}{mm^2}$	$\tan \phi_o$	$\tan \phi_r$	G_f^{II} $\frac{N}{mm}$	$\tan \psi$
0.3	0.02	0.6	0.75	0.75	0.1	0.2

Table 8.2: Mechanical parameters employed for the interface between the masonry wall and the foundation.

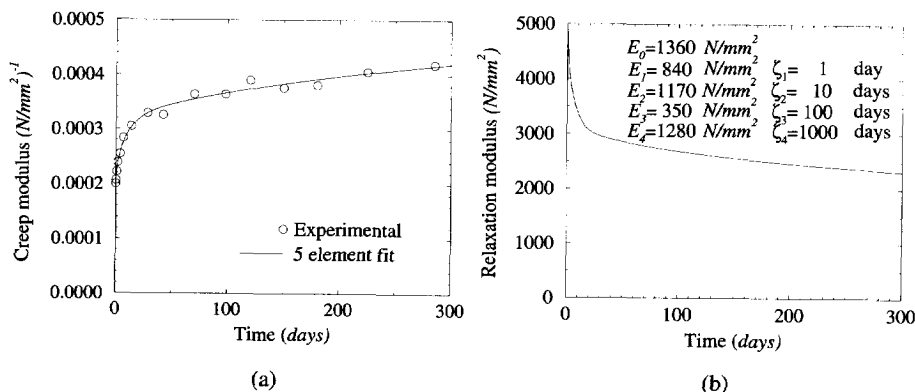


Figure 8.3: (a) Measured creep and fitted five-element Dirichlet function. (b) Relaxation function derived from (a).

Figure 8.4a. Figure 8.4b shows the computed responses in terms of the width of the primary crack versus the applied shrinkage. The wall behaves elastically up to a shrinkage of approximately 0.13 mm/m . Then the primary crack is initiated at the bottom centre of the wall. Subsequently the primary crack propagates upward and widens, while also secondary cracking occurs. The momental/incremental displacements, the tensile principal stresses and the principal plastic/crack strains are shown in Figure 8.4b at the final stage of Figure 8.4a. The analyses have been terminated just before the primary crack reaches the top surface. This snap-through behaviour will be investigated in Chapter 9. Here, the focus is on the (in)objectivity of the pre-snap results with respect to the finite element mesh.

The secondary crack spacing and alignment are clearly inobjective with regard to the element size and shape. Different secondary crack patterns are found, with persistent vertical secondary cracking when the quadrilateral elements are employed, as opposed to a 45° inclined secondary crack obtained with the crossed triangular mesh. Despite these differences with regard to the secondary cracking, no significant difference in the primary crack width evolution has been found, Figure 8.4b.

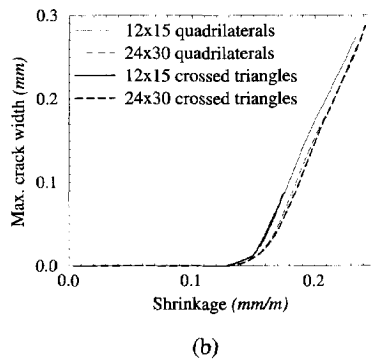
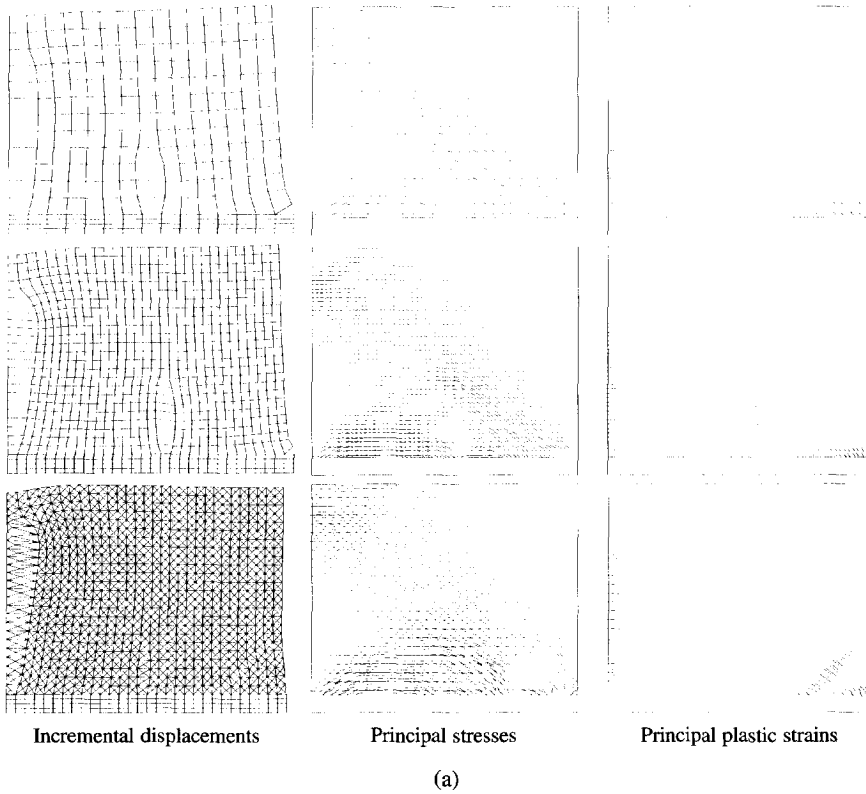


Figure 8.4: Base-restrained shrinking masonry wall response showing (a) the mesh-dependent pattern of secondary cracks, but (b) the mesh-independent primary crack evolution.

The rate dependence of the restrained shrinkage behaviour is briefly studied next with the mesh of 12x15 quadrilateral elements. For this purpose, either the bulk creep characteristics, or the shrinkage rate can be varied. Both approaches are followed here. Firstly, the analysis is repeated for the low, constant shrinkage rate shown in Figure 8.5a. Obviously, now a smaller maximum crack width is obtained for the same amount of shrinkage, Figure 8.5b. Conversely, a higher maximum crack width is computed when imposing a high shrinkage rate. The limiting case of an infinite shrinkage rate is simulated next, via an analysis in which creep is set to zero, Figure 8.5b. It can be concluded from these results that the bulk creep enhances the constrained shrinkage resistance. The omission of the bulk creep in the modelling strategy, as was done in previous studies (Rots 1994, Lourenço 1996) is, therefore, a conservative approach.

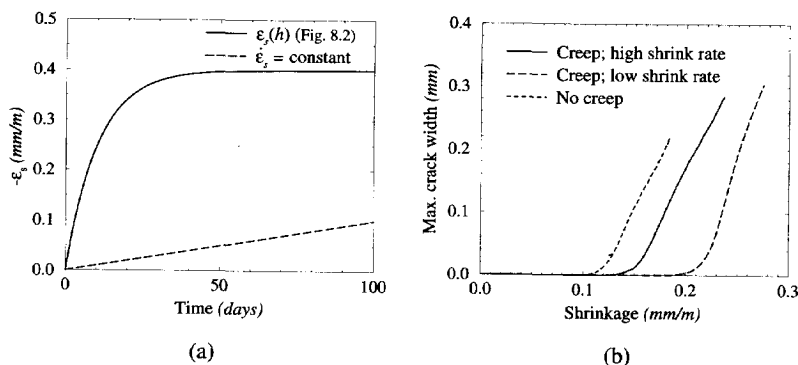


Figure 8.5: The influence of bulk creep and (a) different shrinkage rates on (b) the primary crack width in a base-restrained shrinking masonry wall.

8.3 Regularisation through the cracking rate dependence

The inobjectivity with regard to the crack pattern has been shown in the previous section, where no cracking rate term has been included. Yet, the primary crack width evolution has been unaffected. This is not always the case, as is shown in Figure 8.6 for a slight change in the model parameters. This significant difference in the primary crack growth has been brought about by employing a 5% difference instead of the previous 10% difference in the strength and fracture energies between the primary crack region and the rest of the wall. Now the secondary crack becomes dominant in the quadrilateral mesh, as can be seen from the arrest of the primary crack at a width of 0.1 mm when the shrinkage strain exceeds 0.2 mm/m, Figure 8.6b.

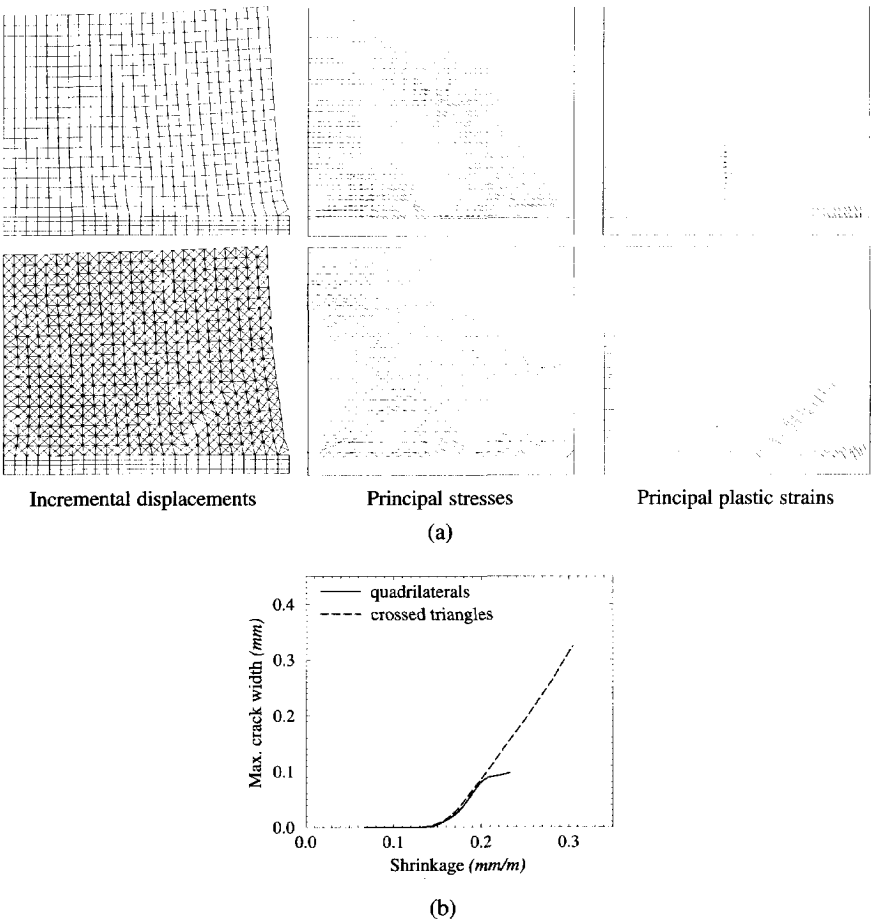


Figure 8.6: Base-restrained shrinking masonry wall with slightly altered material model parameters, showing the (a) mesh-dependent crack pattern and (b) mesh-dependent global response in terms of the primary crack evolution.

Next the crack rate term, section 3.2.4, is activated by employing the simple cracking viscosity model, eq. (3.56). No direct way of determining the dashpot viscosity m exists. In Chapter 6 it has been shown how an inverse process can be employed for this purpose. Since no experimental data exists from which it can be characterised, a numerical investigation has been made of the influence of the viscosity on the mechanical response of a uniaxially restrained masonry specimen, which is fabricated of the same material as the wall under investigation. Because of the low rate of the shrinkage process ($\epsilon_{s,o} \approx 2 \times 10^{-5} / \text{day}$ during the first 10 days, Figure 8.2), it requires a high viscosity to modify the mechanical response. A value of $m = 2000 \text{ Nday/mm}^2$ produces a slight increase in strength compared to the rate-independent response, Figure 8.7, which is the minimum requirement for the rate effect to modify the base-restrained shrinking wall response. Furthermore, a 50% increase in peak strength is achieved by a 10^4 -fold increase in the shrinkage rate, which is in agreement with the increase reported by Zhou (1992), Figure 6.3b. However, there is an excessive strength increase beyond this loading range ($\epsilon_{s,o} > 2 \times 10^{-4} / \text{day}$). This does not mean that the viscosity is invalid, but rather that either a rate-dependent viscosity should be used, or that a logarithmic-type formulation such as eq. (3.55) should be considered for application in loading ranges beyond the current loading range. In the latter case care must be taken to preserve the regularisation ability.

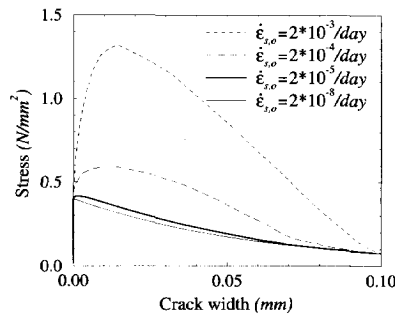


Figure 8.7: The mechanical response of uniaxially restrained masonry subjected to various, constant shrinkage rates for $m = 2000 \text{ Nday/mm}^2$.

By the inclusion of the rate term with $m = 2000 \text{ Nday/mm}^2$, the crack patterns shown in Figure 8.8 are obtained. The primary crack evolution and the secondary crack location and orientation are now captured objectively.

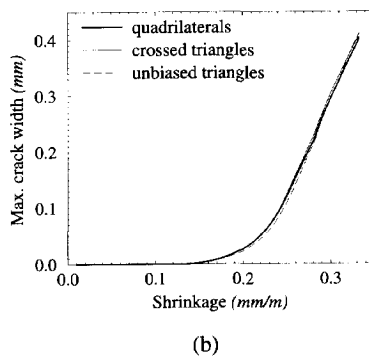
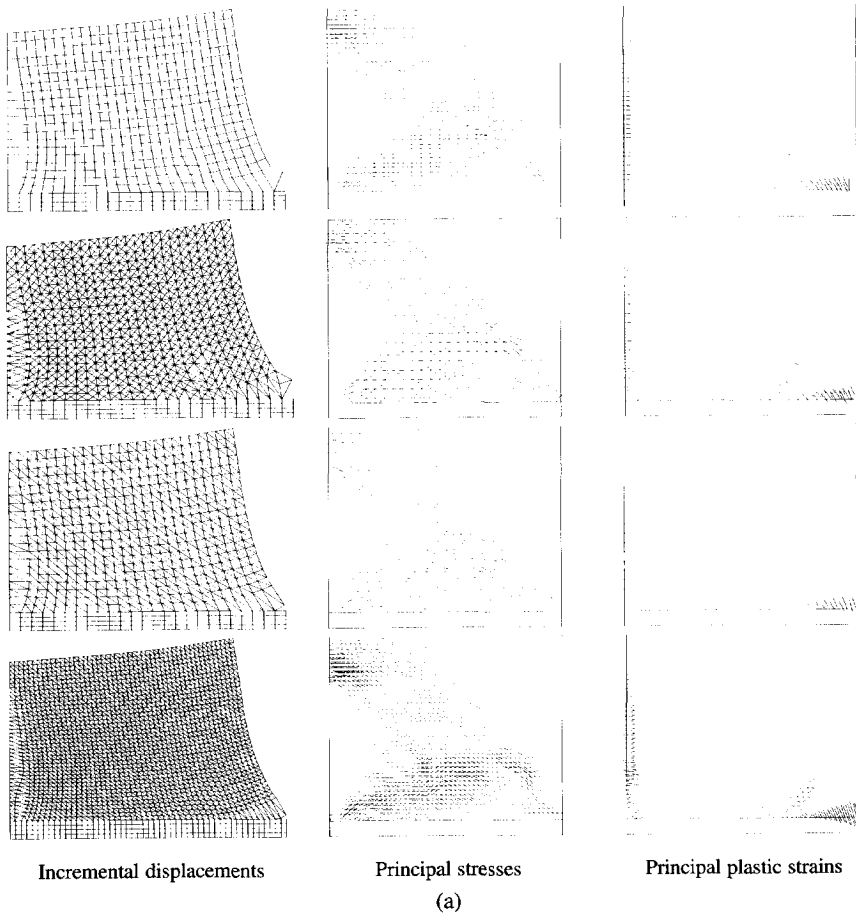


Figure 8.8: Base-restrained shrinking masonry wall (a) crack pattern and (b) primary crack evolution objectivity when including the crack growth rate term, with $m = 2000 \text{ mm/day}$.

Chapter 9

TOWARDS RATIONAL DESIGN RULES

The value of the numerical model can be increased considerably if its application is extended from the analyses of experimental specimens and existing designs to include the design of engineering structures. In this Chapter a step in this direction is made. It is illustrated how, through numerical analyses, design rules can be derived. A particularly lean design aspect, namely the spacing of movement joints in masonry walls, which controls cracking due to differential thermal and hygral movement, is taken as illustrative example. This choice is inspired by the claim that cracking due to restrained shrinkage is the dominant cause of damage in masonry buildings in The Netherlands (De Jong 1992). Although the damage investigated in this chapter does not jeopardise structural safety, the serviceability in terms of moisture impermeability, thermal and acoustic characteristics, and aesthetics are impaired.

The purpose of this chapter is to demonstrate a simplified modelling strategy, which makes the repetitive analyses of shrinking walls viable. The strategy is verified with reference behaviour, which is obtained from the discrete analyses of the walls. Subsequently, the step to derive design rules is described.

9.1 Current status of movement joint spacing design

The design of movement joints in masonry buildings remains an art, guided by empirical rules, which differ from design office to design office (Rots 1996). Semi-analytical rules have been proposed by Copeland (1957), Hageman (1968) and Schubert (1988) for walls without openings, such as the base-restrained wall analysed in the previous chapter and shown again in Figure 9.1a for ease of reference. The omission of a movement joint has led to the cracking and eventual separation of the wall at the location of the primary crack. The analytical rules are based on the linear elastic stress distribution in walls, which are considered to be homogeneous continua, Figure 9.1b.

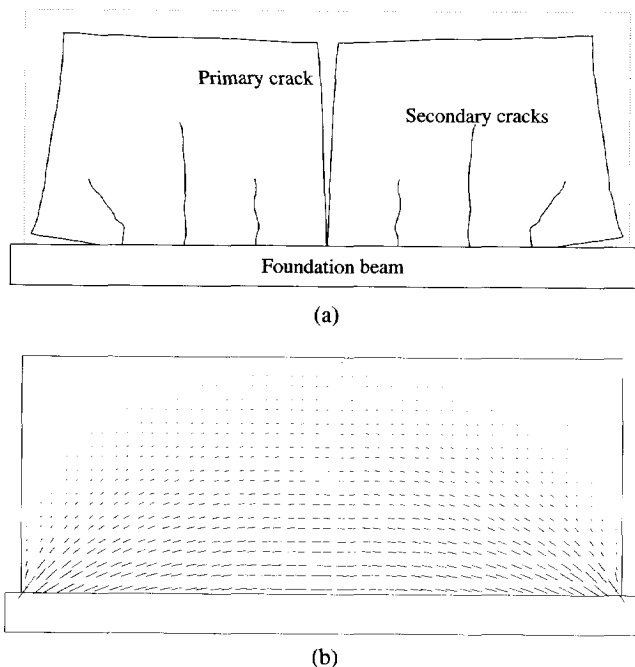


Figure 9.1: (a) Crack pattern and in base-restrained shrinking wall. (b) Principal tensile stresses for linear elastic behaviour and a homogeneous wall.

Furthermore, these rules employ strength-based criteria. A certain *average* tensile stress in the wall should not exceed a strength limit. Such a criterion does not include fracture mechanics, which partly explains the large differences in the proposed joint spacing by these rules. This is illustrated in Figure 9.2, where the semi-analytical design curves for movement joint spacing (L) to height (H) ratios for single leaf, masonry walls, which are restrained at the foot by a concrete beam of different hygral and thermal properties, are shown for two different types of masonry.

Another shortcoming of the existing design rules is that no indication of crack width can be given. By a numerical approach it is possible to get rid of some of the simplifying assumptions necessary for analytical derivations. Also, a numerical approach allows for a realistic simulation of the cracking that occurs in a wall. Hereby, the occurrence of cracks of maximum width deemed to be unacceptable for a particular structural application, can be established, which enables the derivation of rational design rules. However, some simplification has to be accepted in order to circumvent the high demand on modelling

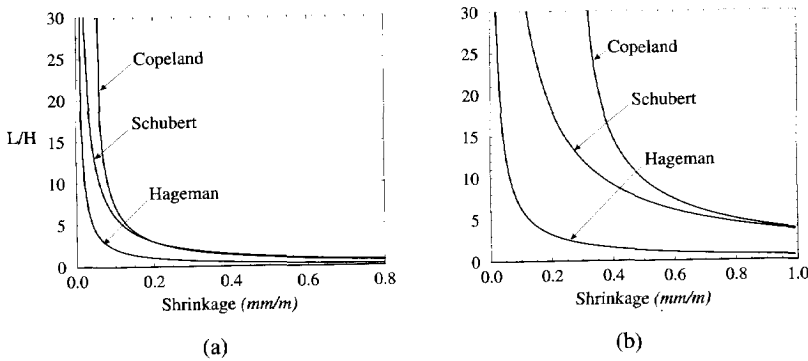


Figure 9.2: Discrepancy in semi-analytically derived spacing of movement joints in base-restrained shrinking walls. Figure (a) and (b) represent wall types of different stiffness modulus, tensile strength and foundation rigidity.

and computing time. In the following sections a simplified modelling strategy is discussed and verified.

9.2 Modelling approach

The same modelling approach is followed as introduced by Rots (1994), Figure 9.3. This approach considers a plane-stress representation of the wall and assumes that all nonlinear behaviour concentrates at the primary crack. There interface elements are employed, obeying the interface material model described in section 5.1. The continuum away from the central, primary crack is assumed to behave linear elastically. As has been demonstrated in Chapter 8, secondary cracking and creep can be captured by activating the Rankine yield criterion combined with visco-elasticity, section 5.2. However, the inclusion of smeared secondary cracking complicates the analyses. Due to the almost homogeneous stress state in long walls, many integration points will crack simultaneously, often leading to numerical difficulties caused by several, hardly distinguishable equilibrium paths, indicated by multiple negative eigenvalues of the stiffness matrix. To continue an analysis beyond such a point of bifurcation calls for some branch switching capability (Van der Veen 1998). Alternatively, the homogeneous situation can be avoided by the adequate modelling of imperfections in the walls. Here, a conservative approach is adopted by neglecting the secondary cracking. Also, the effect of bulk creep has been ignored for simplicity. In section 8.2 this has been explained to give a base-restrained shrinkage re-

sponse which is on the safe side. Furthermore, these simplifications do not render the verification of the equivalent mode I crack modelling strategy, Figure 9.3, invalid, neither so the illustration of the derivation of design rules from the results of numerical analyses, which are the two major goals of this chapter. Moreover, it enables direct comparison with the simplified analytical design rules, which neglect these phenomena.

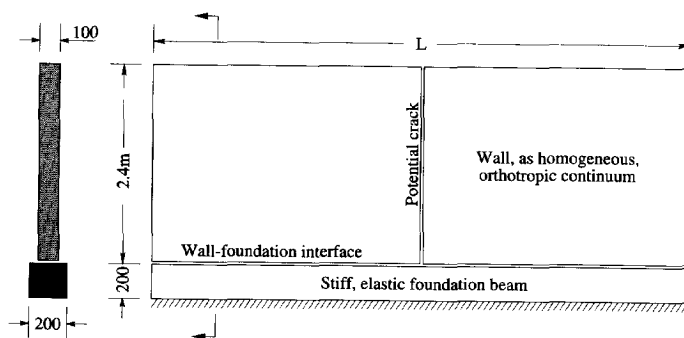


Figure 9.3: Modelling approach for analysis of base-restrained shrinking walls.

A stiff, elastic concrete foundation is modelled with a Young's modulus $E = 30000 \text{ N/mm}^2$ and a Poisson's ratio $\nu = 0.2$. Slipping along the wall/base interface is not included for lack of experimental data, but also to demonstrate the worst case scenario. For all the analyses quadratically interpolated finite elements are employed. Eight-noded quadrilateral elements discretise the continuous parts and six-noded interface elements capture the (potential) discrete cracks.

The own weight is included, by initially applying a vertical volume load of the density of the particular masonry type, multiplied by the gravitational acceleration. The same simplified shrinkage and thermal strain evolutions are assumed as by the analysts (Copeland 1957, Hageman 1968, Schubert 1988). This entails a combined hygral and thermal shrinkage, which is spatially uniform and increases linearly in time. The proper investigation of a stochastically varying environmental conditions and the accompanied hygral and thermal distributions and gradients, see for instance Chapter 7, lies beyond the scope of this study.

9.2.1 CHARACTERISATION OF THE EQUIVALENT VERTICAL CRACK

To characterise the equivalent vertical crack for the simplified modelling strategy, Figure 9.3, an appropriate constitutive law is sought for the interface elements which represent

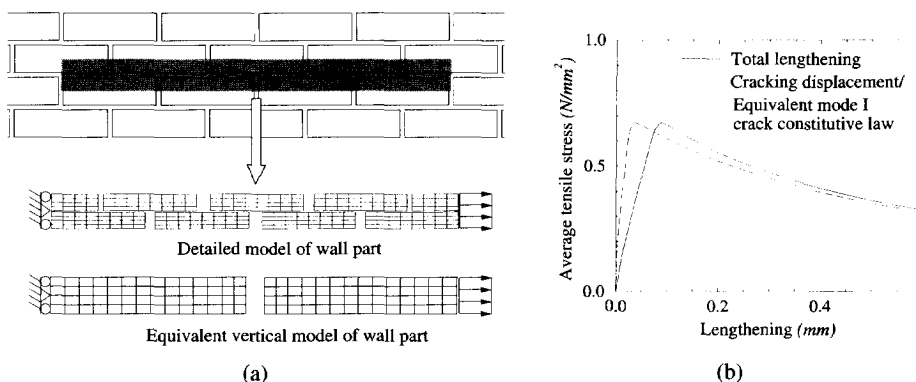


Figure 9.4: Illustration of determination of the equivalent vertical crack constitutive behaviour. (a) The periodic wall part analysed with the discrete approach, also showing the simplified strategy of a single mode I crack. (b) The stress-deformational response of the discrete model. By subtraction of the elastic deformation, the constitutive law for the equivalent crack is found.

the crack. For this purpose a periodic wall part is analysed, Figure 9.4. By studying the behaviour of such a representative wall part under conditions which reasonably simulate those in the actual wall in the area of the primary crack, a constitutive law for the equivalent crack can be derived.

Figure 9.4 illustrates the characterisation process. A discrete analysis is performed of the periodic part, Figure 9.4a, to determine its deformational response, Figure 9.4b. By subtraction of the elastic deformation, the cracking deformation is found, which defines the constitutive behaviour of the equivalent mode I crack in the simplified modelling strategy. The elastic response is captured by the homogeneous, continuous part of the simplified model.

The important issues which should be captured with reasonable accuracy in this characterisation process are the loading conditions, the failure mechanism and the level of confinement, or boundary conditions. If one assumes that the main actions in the base-restrained shrinkage wall are horizontal, as the principal stresses indicate for the case of the homogeneous wall of Figure 9.1b, the response of such a periodic part under uniaxial tension should represent the behaviour of the wall in the vicinity of the primary crack. The correct failure mechanism can be captured by employing the discrete modelling approach,

section 5.1. The third issue, namely the simulation of the in-situ confinement, is not trivial. This will be demonstrated by studying two extreme cases of vertical confinement in the next section.

The choice of the specimen length is governed by two criteria. Firstly, a sufficient number of head joints should be included to capture all the significant cracking in the area of the primary crack. Secondly, the influence of the tensile load introduction should be limited according to the *St. Venant principle*.

9.2.2 TYPICAL DUTCH MASONRY CHARACTERISATION

Two typical Dutch masonry types have been investigated, namely a clay brick ($210\text{mm} \times 52\text{mm} \times 100\text{mm}$) with 10mm thick 1:2:9 volume cement:lime:sand mix mortar joints (JOB) and a calcium silicate unit with 10mm joints of $1:\frac{1}{2}:4\frac{1}{2}$ mortar (KZC). The total set of material model parameters is given in Tables 9.1 and 9.2.

All parameters have been obtained by averaging, regression or least square fits to experimental data (Van der Pluijm and Vermeltfoort 1991, Van der Pluijm 1992). Imperfection is simulated in both the JOB and KZC specimens by employing the above parameters in the central area, where the primary crack is expected, while the remainder is assumed to be 10% stronger and 33% tougher (higher fracture energies). This spread lies within the coefficients of variation found for these parameters.

To obtain the correct wall part response found in the structure of interest, the influence of boundary conditions is important. A simple simulation of the confining effect of sur-

	E $\frac{N}{mm^2}$	ν	Potential brick crack			
			k_n $\frac{N}{mm^3}$	k_s $\frac{N}{mm^3}$	f_t $\frac{N}{mm^2}$	G_f^I $\frac{N}{mm}$
(a)	16700	0.28	1.0×10^6	1.0×10^6	2.0	0.08
(b)	13400	0.20	1.0×10^6	1.0×10^6	2.0	0.06

Table 9.1: Parameters for bricks in (a) JOB and (b) KZC specimens.

	k_n $\frac{N}{mm^3}$	k_s $\frac{N}{mm^3}$	f_t $\frac{N}{mm^2}$	G_f^I $\frac{N}{mm}$	c_o $\frac{N}{mm^2}$	G_f^{II} $\frac{N}{mm}$	$\tan \phi_o$	$\tan \phi_r$	$\tan \psi_o$	σ_u $\frac{N}{mm^2}$	δ
(a)	825	355	0.6	0.012	0.88	$0.06 - 0.13\sigma$	1.01	0.75	1.06	-1.42	5
(b)	438	182	0.1	0.005	0.28	$0.02 - 0.03\sigma$	0.97	0.75	0.67	-1.22	17

Table 9.2: Parameters for head and bed joints in (a) JOB and (b) KZC specimens.

rounding masonry on the wall part is obtained by forcing the upper and lower edges to remain horizontal. The left and right edges are kept vertical, but due to the chosen wall part length, which now includes four bricks, no influence from these edges exist. Two levels of such vertical confinement are applied, namely:

boundary (1): free vertical translation of the horizontal upper and lower edge and

boundary (2): zero vertical translation of the horizontal upper and lower edge.

The respective wall part responses are shown in Figure 9.5. JOB exhibits unit cracking irrespective of the confinement. This is due to the relatively strong adhesion of the JOB joints, Table 9.1, which prevents shearing along the bed joints. KZC is sensitive to the confinement, failing in stepwise fashion for unconfined boundaries and vertical crack mode when confined. The KZC joints are relatively weak when no confining pressure exists, Table 9.1, allowing the bed joints to fail in the case of *boundary (1)*. However, when the vertical dilation upon shearing is prevented, *boundary (2)*, wedging occurs and the Coulomb-frictional strength of the bed joints increases so that the units become the weak link. Quite different global load-deformational responses accompany the two failure modes, Figure 9.5b. This inhomogeneous primary cracking behaviour complicates the simplified modelling approach. A pragmatic solution is to employ both constitutive relations for the equivalent crack in the large, base-restrained shrinking wall analyses and subsequently choose the global behaviour which requires the most conservative movement joint spacing.

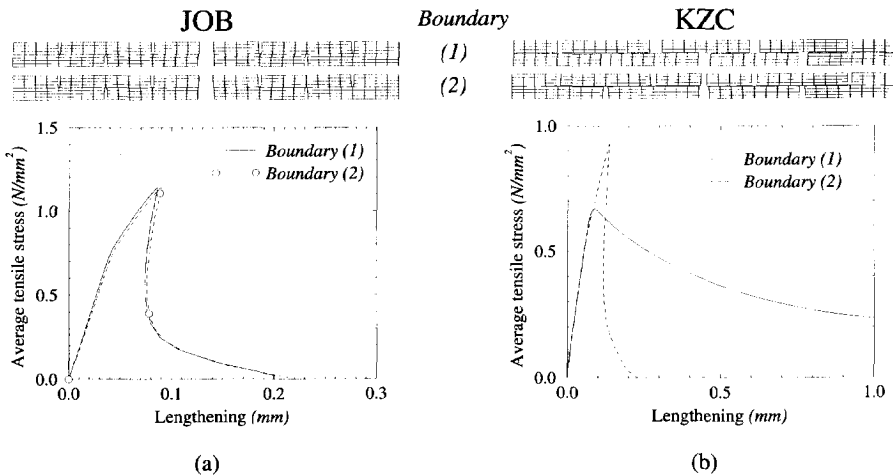


Figure 9.5: Influence of boundary conditions on (a) JOB and (b) KZC wall part response.

9.3 Verification of modelling approach

The modelling strategy is verified numerically. This is done by comparing the responses of single leaf base-restrained shrinking masonry walls, which are calculated with the equivalent vertical crack modelling strategy, with the responses obtained from the discrete analysis modelling strategy, section 5.1. From the latter the reference behaviour is analysed. For the simplified analyses, the constitutive behaviors, which are obtained from the periodic wall part analyses of the previous section, are employed for the equivalent vertical cracks.

9.3.1 REFERENCE RESPONSE: DISCRETE ANALYSES OF BASE-RESTRAINED WALLS

To restrict the model size, the masonry wall is only partially discretised. Only the central four units and their joints are discretised, which enables the capturing of the primary crack, Figure 9.6. The remaining part of the wall is modelled as a orthotropic, linear elastic continuum, with homogenised masonry elasticity parameters.

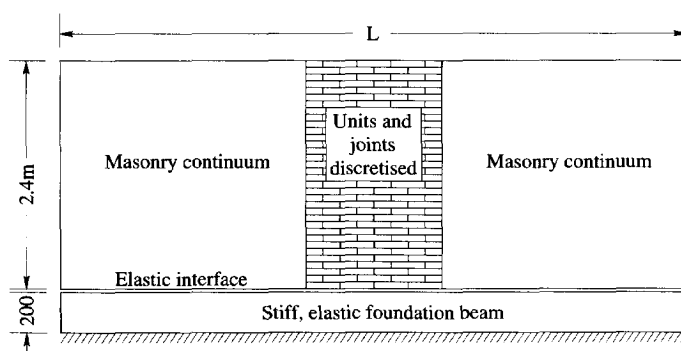


Figure 9.6: Schematic representation of model for (partially) discrete analyses.

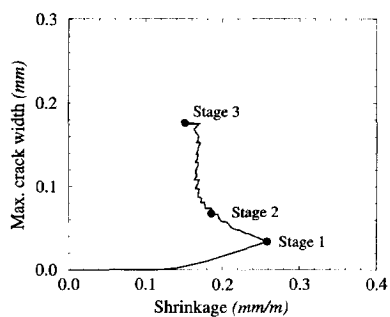
An imperfection is simulated in the same manner as has been done in the wall part analyses, section 9.2.2. For the KZC specimens a non-symmetric crack pattern is chosen and triggered by prescribing the lower strength and fracture energy also for the column of bricks just to the left of the centre.

Two walls of each masonry type of respectively 6 m and 12 m long are analysed. In Figures 9.7 and 9.8 the crack propagation is shown at different stages of shrinkage in 6 m JOB and KZC walls respectively. The responses for the 12 m JOB and KZC walls are portrayed in Figures 9.9 and 9.10. In each of the figures the primary crack width evolution

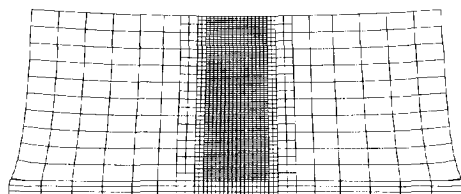
with shrinkage is shown. Four stages of wall deformation can be identified. At stage 1 micro-cracks have opened in the head joints. For all four cases this stage marks the initial peak shrinkage capacity, Figures 9.7-9.10a. Stage 2 marks the localisation of the micro-cracks into a macro-crack. This occurrence coincides with a reduced shrinkage capacity, a so-called snap-back in the global behaviour, during which the bulk of the walls does not shrink, but expands, while the crack grows and widens. In the short walls, the crack initiates near the wall base, Figures 9.7, 9.8. In contrast, the macro-crack originates at mid-height in the long JOB wall, Figure 9.9 and at the top in the long KZC wall, Figure 9.10. Subsequently the macro-cracks grow, stage 3, until the walls separate, stage 4.

Note that the reduction in shrinkage with the increasing crack width means that the environment should enable the wall to adhere to this particular shrinking history for the shrinkage-crack width responses shown to realise. In reality, the crack will open dynamically for increased shrinkage to a configuration of sufficient shrinkage resistance, as indicated for the 6 m KZC wall, Figure 9.8d. To trace this "snap-back" in shrinkage, and thus in time for the assumed continuously increasing shrinkage, the adaptive time-stepping procedure of section 4.2.6 has been employed.

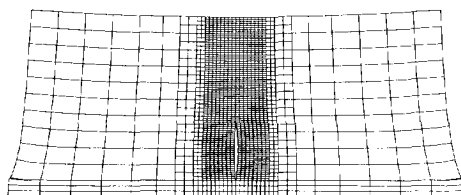
Note further that the "wiggles" in the response are due to the mesh roughness. Each post-peak local minimum corresponds with the crack propagation through an element. However, the snap-back in the 6 m KZC wall response between stages 2 and 3, Figures 9.8a,c,d, occurs when the propagation of the step-wise crack is prohibited by the limited discretisation and forced vertically.



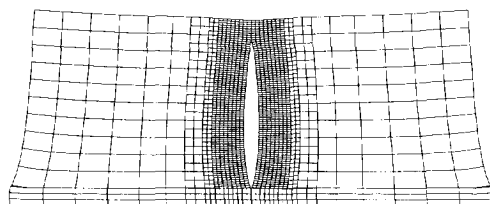
(a) Crack width evolution with shrinkage



(b) Stage 1: Various small cracks at base

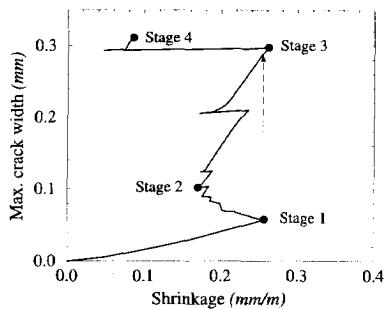


(c) Stage 2: Initiation of primary crack at base

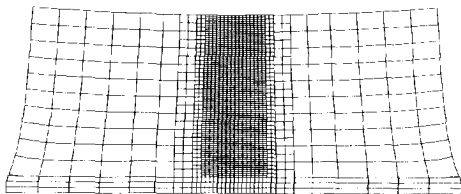


(d) Stage 3: Primary crack growth upward

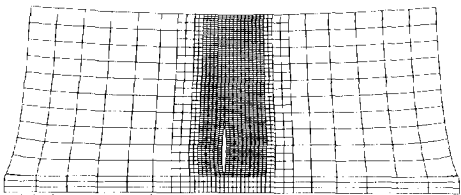
Figure 9.7: 6 m JOB wall base-restrained shrinkage deformation.



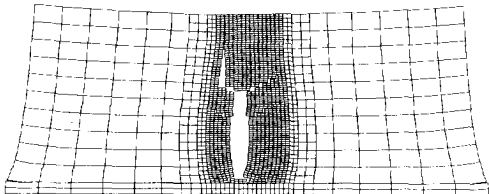
(a) Crack width evolution with shrinkage



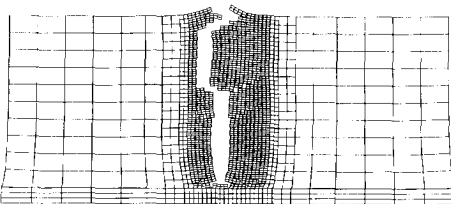
(b) Stage 1: Various small cracks at base



(c) Stage 2: Initiation of primary crack at base

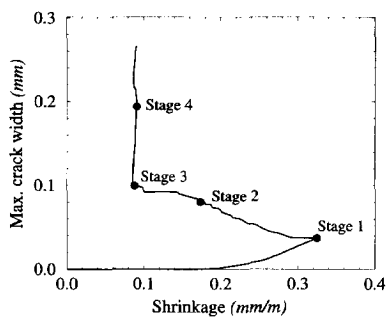


(d) Stage 3: Primary crack growth upward

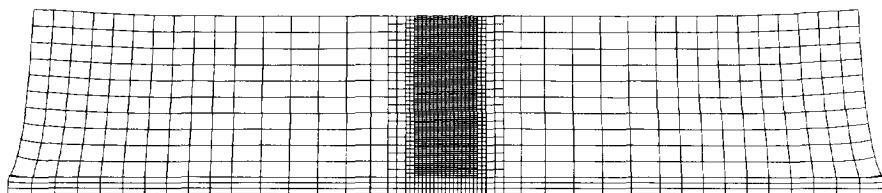


(e) Stage 4: Wall separation

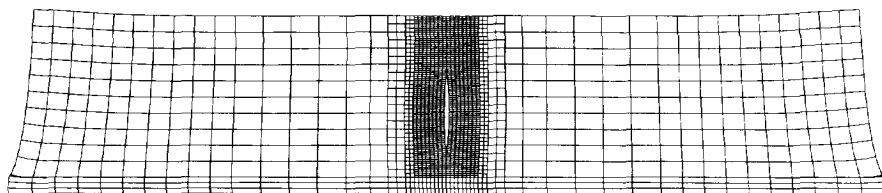
Figure 9.8: 6 m KZC wall base-restrained shrinkage deformation.



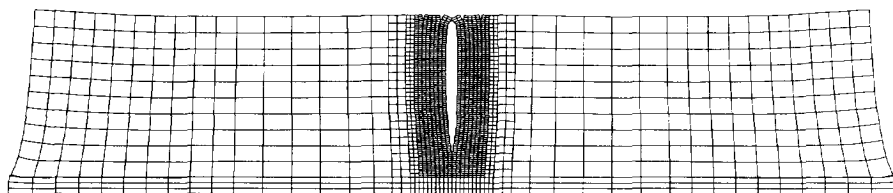
(a) Crack width evolution with shrinkage



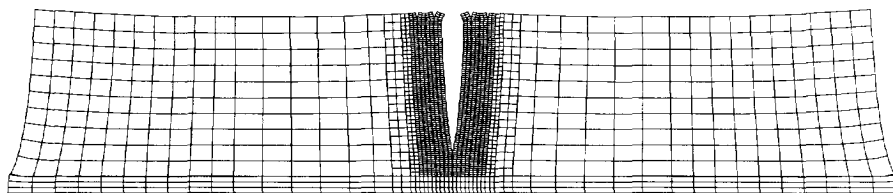
(b) Stage 1: Various small cracks



(c) Stage 2: Initiation of primary crack at mid-height

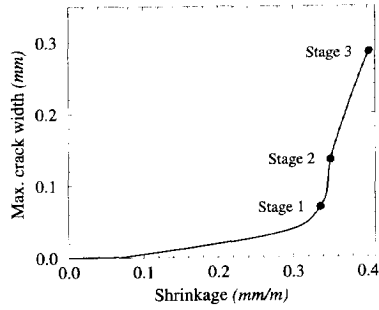


(d) Stage 3: Primary crack growth upward and downward

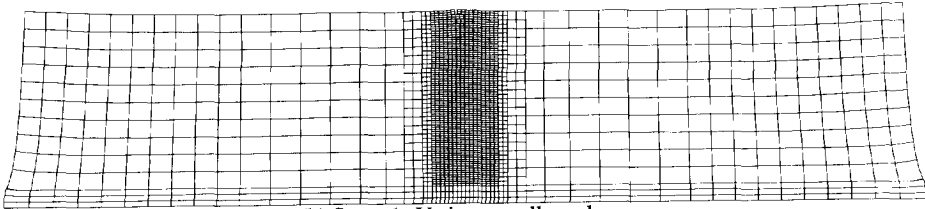


(e) Stage 4: Wall separation

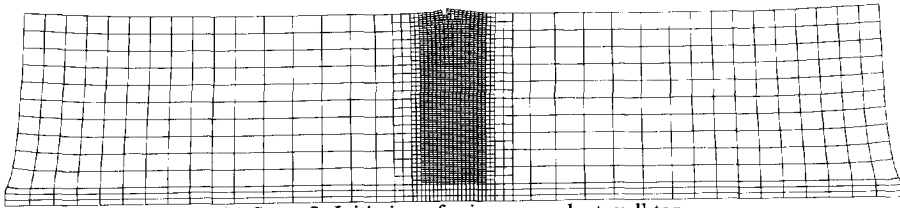
Figure 9.9: 12 m JOB wall base-restrained shrinkage deformation.



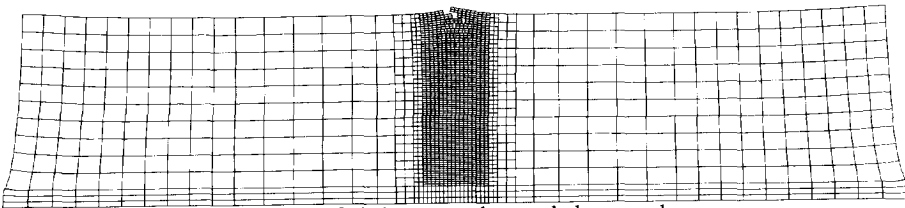
(a) Crack width evolution with shrinkage



(b) Stage 1: Various small cracks



(c) Stage 2: Initiation of primary crack at wall top



(d) Stage 3: Primary crack growth downward

Figure 9.10: 12 m KZC wall base-restrained shrinkage deformation.

The clay brick walls (JOB) exhibit a vertical failure mode, in agreement with the wall part study of the previous section. This is due to the relatively strong bed joints in the JOB masonry, Tables 9.1, 9.2. The bricks fail in tension before the Coulomb-friction strength of the bed joints is reached. Vertical cracking also occurs in the lower part of the 6 m KZC wall, but then step-wise cracks along head and bed joints grow. The latter are then inhibited by the limited discretisation and forced into vertical cracks until the upper, unbounded part again fails in stepwise fashion. This behaviour confirms the sensitivity of the KZC material to the level of confinement, as has been revealed by the wall part study, Figure 9.5b. It has a low adhesion strength, Table 9.2, but due to the confinement of the dilational normal uplift upon shearing near the base, the Coulomb-frictional strength increase of the bed joints prevents further shear-slipping, enforcing brick cracking. Closer to the free upper surface there is less confinement, so that the brick tensile strength is not reached. In the nearly homogeneous stress state in the centre of a long wall the crack initiates at the weakest spot. Due to the low confinement at the upper surface in the 12 m KZC wall, the crack starts at the top and subsequently propagates downward in a step-wise fashion along the weak, unconfined joints.

9.3.2 EQUIVALENT MODELLING RESPONSE

Now the walls analysed in the previous section are re-analysed with the simplified equivalent vertical crack modelling strategy, Figure 9.3. The vertical crack constitutive behaviour is taken as the nonlinear response of the wall part Figure 9.5, section 9.2.2.

Figures 9.11 and 9.12 reveal that there is reasonable agreement between the responses obtained from the simplified and the discrete models in the case of the 6 m and the 12 m JOB walls. This is not surprising, because the JOB walls indeed fail in a mode I fashion, Figures 9.7, 9.9. Also, the crack initiation location and subsequent growth are captured accurately for both the 6 m and 12 m wall.

A much poorer agreement is obtained in the case of the KZC walls, Figures 9.13 and 9.14. A homogeneous vertical crack cannot capture the reference response. It has been revealed already in the wall part analyses, Figure 9.5b, that the KZC response is sensitive to the surrounding confinement, which has been simulated by employing two different sets of boundary conditions. This fact has been confirmed by the reference failure pattern in the KZC wall, Figure 9.8, where successive vertical cracking and step-wise, zig-zag cracking occur. These two failure modes are associated with a quite different constitutive behaviour, Figure 9.5b, which calls for an inhomogeneous vertical crack to be employed in the simplified modelling strategy. Also, the confinement level may vary in time, which

may lead to re-strengthening locally. These matters will be illuminated in the next section.

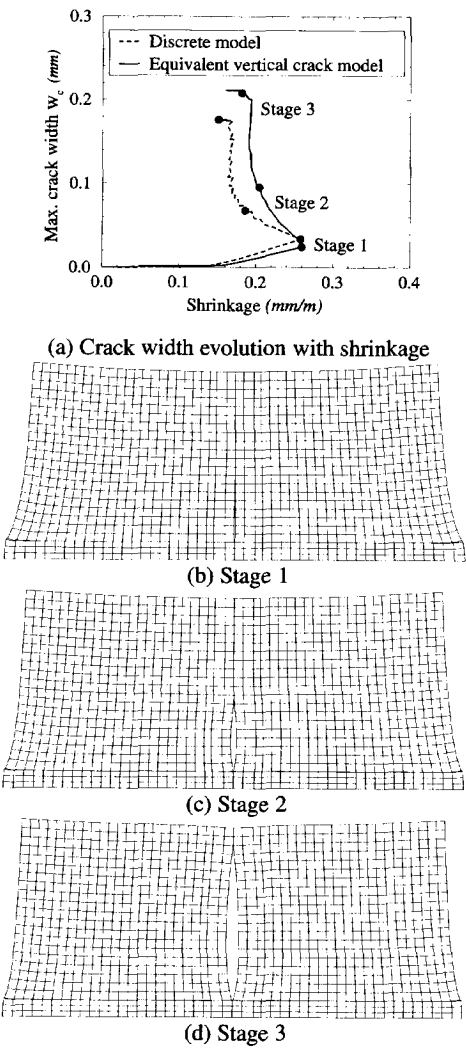
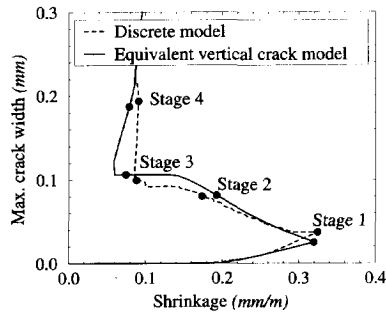
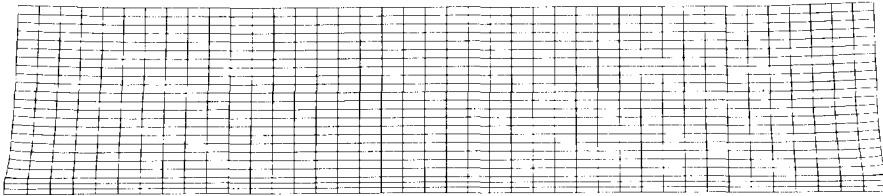


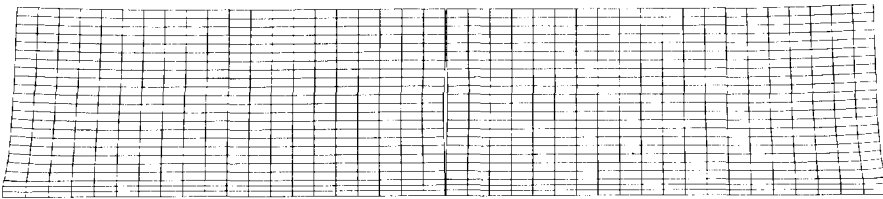
Figure 9.11: 6 m JOB wall base-restrained shrinkage deformation, from simplified analyses.



(a) Crack width evolution with shrinkage



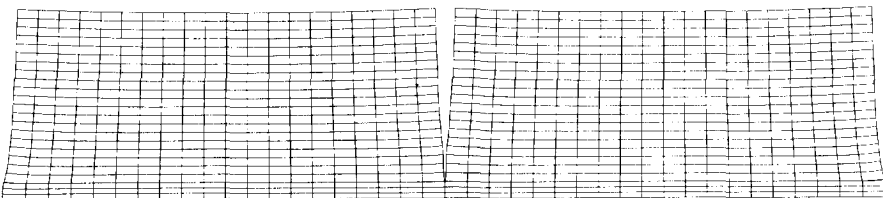
(b) Stage 1



(c) Stage 2

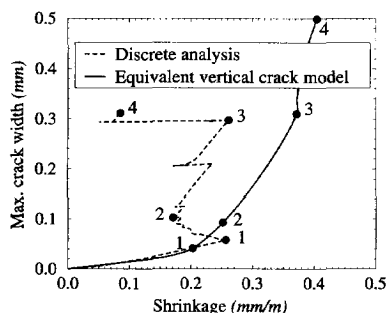


(d) Stage 3

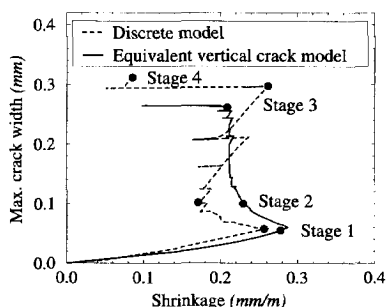


(e) Stage 4

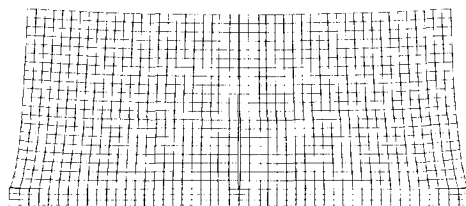
Figure 9.12: 12 m JOB wall base-restrained shrinkage deformation, from simplified analyses.



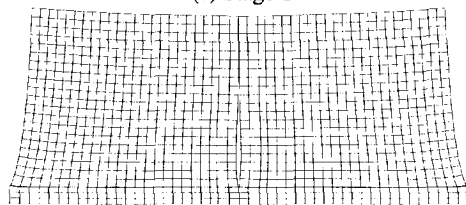
(a) Boundary (1) response



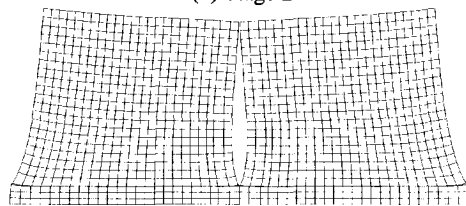
(b) Boundary (2) response



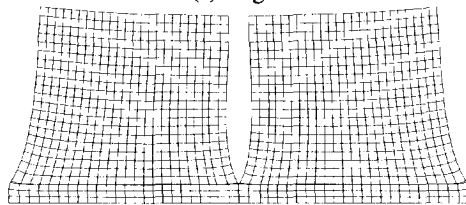
(c) Stage 1



(d) Stage 2

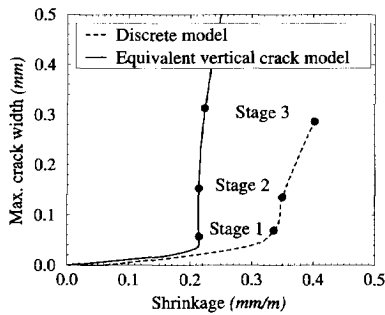


(e) Stage 3

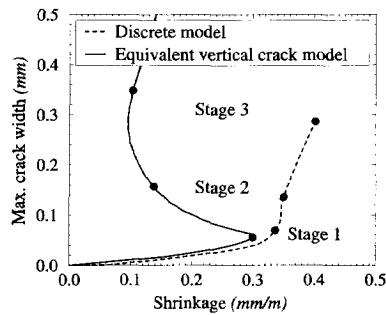


(f) Stage 4

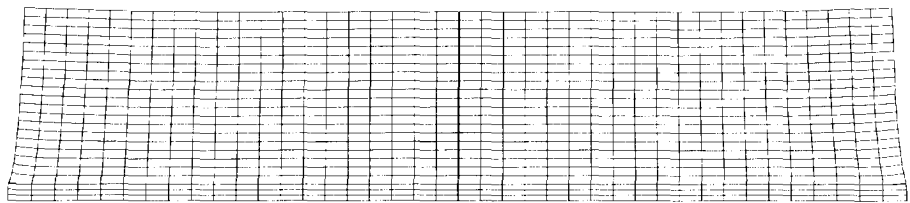
Figure 9.13: 6 m KZC wall base-restrained shrinkage deformation, from simplified analyses with (a) boundary (1) and (b) boundary (2) constitutive behaviour of the central crack respectively.



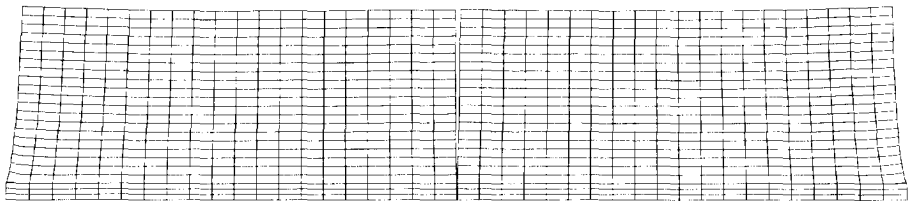
(a) Boundary (1) response



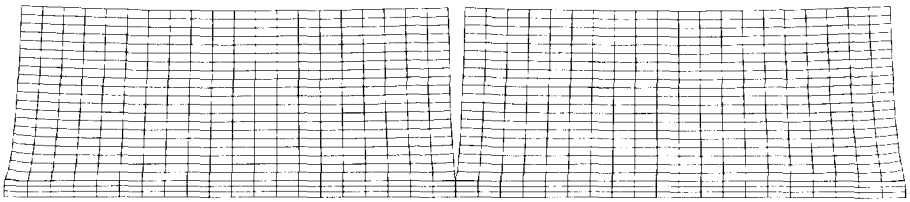
(b) Boundary (2) response



(c) Stage 1



(d) Stage 2



(e) Stage 3

Figure 9.14: 12 m KZC wall base-restrained shrinkage deformation, from simplified analyses with (a) boundary (1) and (b) boundary (2) constitutive behaviour of central crack respectively.

9.3.3 DEFICIENCIES OF SIMPLE MODELLING STRATEGY

It has been shown in the previous section that the equivalent mode I crack strategy reproduces the shrinking wall behaviour with reasonable accuracy for masonry which invariably fails in a mode I fashion. However, this is not the case for masonry which exhibits a preference for a step-wise failure pattern along head and bed joints. The cause is the dilational behaviour of the shearing bed joints and the associated Coulomb-frictional strength increase if this volume increase is prevented by the surrounding, confining masonry. This phenomenon complicates the determination of the equivalent mode I constitutive behaviour, because the level of confinement must be included in the characterisation process. For example, a considerable improvement can be made in the response obtained from the simplified modelling strategy, by assuming the high level of confinement of the *boundary (1)* in the lower part (say one third of the height) of the 6 m KZC wall and the *boundary (2)* level of confinement in the upper part (two third). Figure 9.15 shows the wall response if such an inhomogeneous vertical crack is employed.

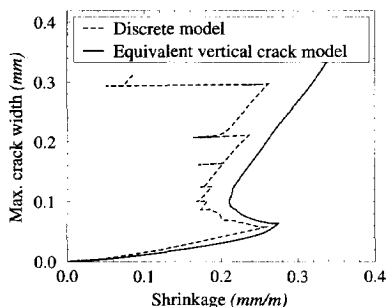


Figure 9.15: 6 m KZC wall response with inhomogeneous vertical crack.

The trend in the reference response is now captured much better. For the 12 m KZC wall, however, the underestimation by the simplified modelling strategy, Figures 9.14a,b, cannot be corrected by employing an inhomogeneous vertical crack. The reason is that the two boundary conditions do not characterise the limits in behaviour in terms of shrinkage resistance of masonry susceptible to mixed mode failure. If the confinement level varies in time, a significantly increased strength and toughness may be instigated. This is illustrated by Figure 9.16, where the KZC wall part response is shown for the hypothetical time-dependent confinement of initially free translation of the upper and lower edges according to *boundary (1)*, and subsequent fixed edges, *boundary (2)*. The instant of fixing the normal displacement of the upper and lower edges marks the onset of re-strengthening of

such a wall part. The second peak strength depends on the level of degradation before the edges are fixed vertically. This is because the remaining potential dilation upon shearing along the bed joints, the restraint of which is the underlying mechanism of the strength increase, decreases with the degradation, eq. (5.16). The re-strengthening response varies from a marked strength increase due to the restraint of significant remaining dilation, which leads to unit failure (Figure 9.5b(2)), through significant strengthening, but not to a sufficient level to change the step-wise head and bed joint failure mode (Figure 9.5b(1)), to no strengthening if the boundaries are fixed only after the bed joints have been smoothed by the shear-slipping.

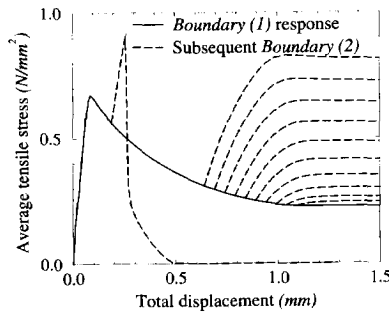


Figure 9.16: KZC wall part behaviour for initially free vertical translation of the upper and lower edges, *boundary (1)*, but subsequent suppression, *boundary (2)*, of further dilation.

If such a double hardening constitutive law is employed for the equivalent crack, much better agreement with the tough 12 m KZC reference behaviour will be obtained. Such an exercise is, however, futile, as no objective way of determining the true evolution of the confinement in the wall exists.

These shortcomings do not outweigh the major achievement of obtaining *conservative* estimates of the base-restrained shrinking walls response relatively cheaply via the simplified strategy. In each case the critical shrinkage, i.e. the shrinkage at which the snap-back starts, is lower than the value in the reference analysis. When repetitive analyses are required from which design rules are to be derived, such savings in modelling and computation time render the underestimation of shrinkage resistance acceptable.

9.4 Design rules

Through the analyses of wall parts, as have been discussed in section 9.2.2, the equivalent vertical crack behaviour is obtained. At this stage the sensitivity to the level of confinement can be assessed and a pragmatic choice be made of the constitutive behaviour which renders the most conservative wall restrained shrinkage resistance.

For the derivation of design rules for movement joint spacing in masonry walls, the simplified modelling strategy should be employed in repetitive analyses to quantify the effects of the various influencing factors, such as the wall length to height ratio, the axial and bending rigidity of the base restraint, the bearing load on the wall and slip along the wall-base interface (Rots 1994). The numerical simulation of these factors presents no problem. As an illustration of the derivation of design rules, the influence of the wall length on the behaviour of the same walls analysed in the previous section is now investigated, Figure 9.17. The same procedure should be repeated to study the effect of each of the above mentioned influencing factors.

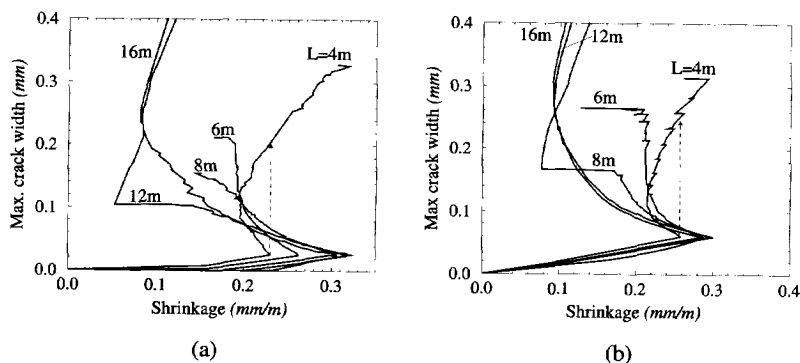


Figure 9.17: (a) JOB and (b) KZC wall response to base-restrained shrinkage, obtained by the equivalent vertical crack modelling strategy. The wall lengths vary from 4 to 16 m.

By plotting the shrinkage values that will cause a particular crack width just not to be exceeded, say 0.5 mm, against the various wall lengths, the connection with practical design rules is made. These values of wall lengths can be considered as crack-free, or rather *unacceptable crack width-free* wall lengths for the applied shrinkage level. Therefore, these wall lengths also serve as minimum spacing of movement joints, which will ensure that cracks wider than 0.5 mm will not occur. In Figure 9.18 the latter, numerical values are compared with strength-based analytical rules (Copeland 1957, Hageman 1968, Schubert 1988).

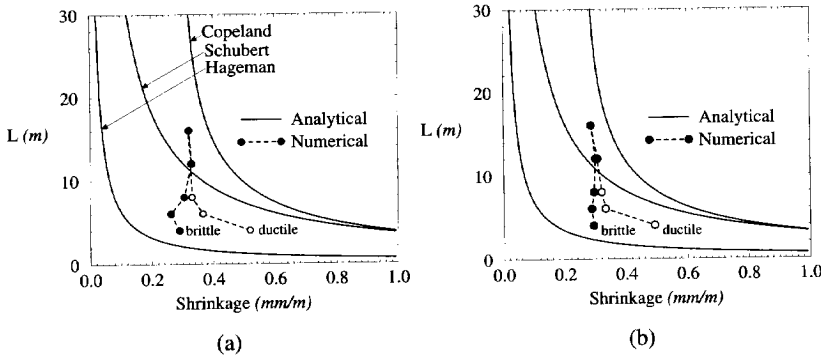


Figure 9.18: Comparison of numerically and analytically determined “uncracked” (a) JOB and (b) KZC wall length under base-restrained shrinkage.

Note that the *brittle* numerical curves have been derived from the responses shown in Figure 9.17, which were computed with the wall part constitutive relations shown in Figure 9.5 (2). For these brittle masonry types it appears that more than one movement joint spacing applies for a particular design shrinkage, which obviously allows the designer to choose the larger spacing. However, if masonry walls with tougher constitutive relations are analysed, the intuitive smaller spacings are computed for higher shrinkage levels - see the *brittle* curves in Figure 9.18. A more detailed discussion of this issue is given in the next section. This underlines the supremacy of the numerical tool, as fracture energy/toughness does not enter the analytical relations.

Furthermore, the consequence of the exceedence of the design shrinkage level is not reflected in Figure 9.18. It will be illustrated in the next section that the larger spacings should be penalised to apply for lower shrinkage levels, because, if the design shrinkage is marginally exceeded, the crack widths will increase dynamically to large values, as opposed to a gradual increase in walls with smaller movement joint spacings.

9.5 Discussion

In this chapter a step has been taken towards applying the numerical model to derive rational design rules. It has been applied to establish and verify a simplified modelling strategy to make large scale computations viable, while predicting the structural behaviour with sufficient accuracy for deriving design rules. Such a simplification is necessary, because the analyses need to be repeated several times to investigate the influence of the various interacting phenomena. The error introduced by the simplification is acceptable

in bridging the gap between fundamental research and practical design rules.

Two further issues deserve a brief discussion. The first is of practical interest and regards the surprising greater resistance of longer walls to restrained shrinkage damage. Secondly, the error introduced by the elastic unloading stiffness employed in the plasticity formulation is studied.

When the influence of the wall length on the restrained shrinkage response is evaluated, the conclusion is that, in contradiction with the analytical models, as well as intuitive reasoning, the numerical analyses indicate a greater resistance to restrained shrinkage for longer walls than shorter walls; see for example Figures 9.17 and 9.18 (the *brittle* case). The underlying cause is the central, vertical tensile stress gradient variation with wall length. For the longer walls a smaller tensile stress gradient exists across the wall height (Copeland 1957, Schubert 1988). In the 12 m JOB wall this causes the central crack to initiate over nearly the total wall height simultaneously, instead of initiating low down and subsequently gradually growing upwards, as in the 6 m wall. The masonry types which have been studied exhibit a low toughness, or fracture energy, which causes the cracked wall part to lose strength relatively quickly, a fact not considered by the analytical models. If a tougher vertical crack is employed, the cracked part can keep its strength longer and contribute to shrinkage resistance. To illustrate this, the JOB walls have been re-analysed with the tougher constitutive behaviour for the central crack shown in Figure 9.19a. As expected, only the shorter walls exhibit significantly different base-restrained shrinkage responses, compare Figure 9.17a with Figure 9.19b. This is also reflected by the movement joint spacing, Figure 9.19c.

Furthermore, in the derivation of design rules the consequences of exceeding the design shrinkage levels must be considered. The danger of exploiting the greater shrinkage resistance of brittle long walls is highlighted in Figure 9.20, where the responses of a 4 m and a 8 m KZC wall are compared. For a 0.2 mm crack width restriction, the shrinkage level may be higher for the longer wall, due to its larger shrinkage resistance before the snap. However, in the event of a shrinkage increase beyond the respective limits, a gradual crack width increase will occur in the short wall, as opposed to an instant crack growth in the long wall to a fully developed, wide primary crack of more than 0.8 mm. If this danger is quantified in the design rules, the large movement joint spacings are penalised to apply for lower expected shrinkage levels. This causes the numerically derived design curve to follow the trend of the semi-analytical curves, namely a reduced movement joint spacing requirement for a higher expected shrinkage level.

These demonstrations highlight the superiority of the numerical model in gaining insight and producing data from which design rules can be derived.

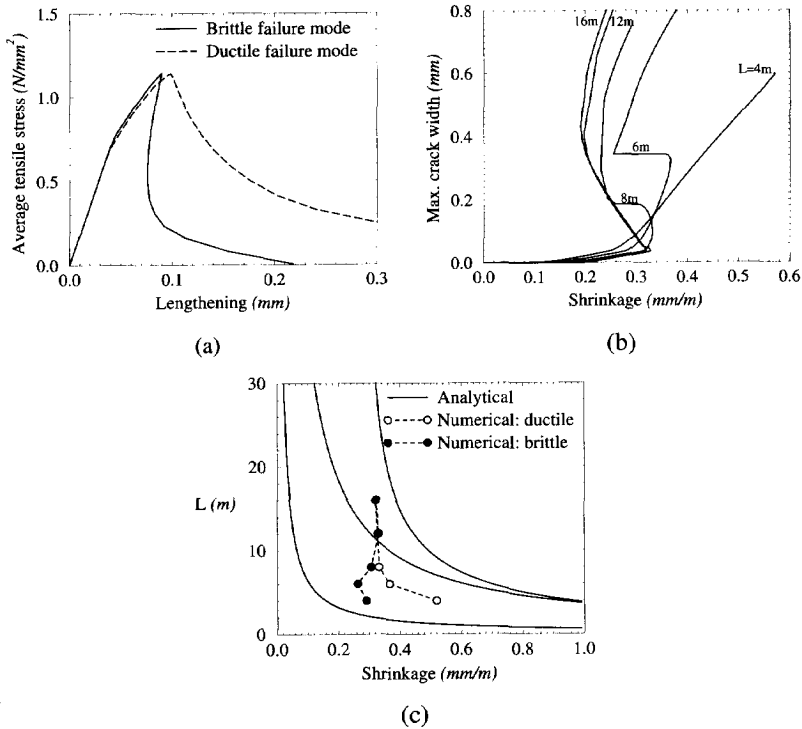


Figure 9.19: (a) Brittle and ductile tensile constitutive behaviour of JOB equivalent vertical crack. (b) Ductile JOB walls base-restrained shrinkage response. (c) Comparison of movement joint spacing rules for brittle and ductile JOB walls.

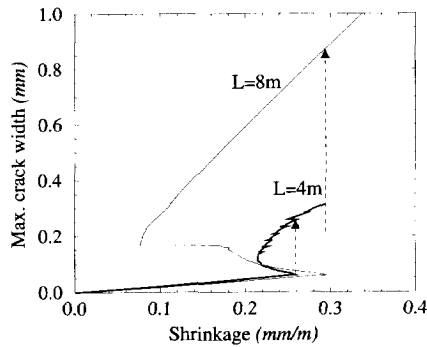


Figure 9.20: Danger of large crack if long wall shrinkage capacity is exceeded illustrated.

The second aspect regards the inability of the numerical model to capture crack closure upon unloading and has been referred to briefly in section 3.2.3. The plasticity formulation employs the elastic modulus for unloading. However, for the simple mode I fracture of the equivalent vertical crack, the tensile mode of the interface material model can be modified to employ an unloading modulus which allows a user-prescribed percentage of crack closure. This is done by writing the one-dimensional stress-update equation for unloading as follows:

$$\begin{aligned} {}^{t+\Delta t}\sigma &= {}^t\sigma + (1-d)k_n \Delta u \\ d_s &= 1 - \frac{{}^{t0}\sigma}{k_n u} \\ d &= \frac{a d_s}{1 - d_s(1-a)} \end{aligned} \quad (9.1)$$

where $0 \leq a \leq 1$ is the crack closure factor, d and d_s represent the reduction in the virgin stiffness and ${}^{t0}\sigma$ is the stress corresponding with the largest strain reached before, as illustrated in Figure 9.21a. Upon re-loading it is necessary to first find the yield surface, after which the usual plasticity predictor-corrector iterations follow to obtain the updated stress. This is formulated as follows:

$${}^{t+\Delta t}\sigma = {}^t\sigma + (1-d)k_n \Delta u_A + E(\Delta u - \Delta u_A - \Delta u^p) \quad (9.2)$$

where Δu_A is the fraction of the crack opening displacement increment required to reach the yield surface, obtained by a simple elastic calculation from

$$u_A = \frac{{}^{t0}\sigma - {}^t\sigma}{(1-d)k_n} \quad (9.3)$$

Now this modified material model is employed to study the influence of the unloading stiffness on the base-restrained shrinking wall behaviour. Figure 9.21b compares the extreme responses of elastic unloading ($a = 0$) and secant unloading ($a = 1$). The only difference occurs during the snap-back, which accompanies wall separation. The negligence of inertia already renders this part of the response, which is in fact explosive, doubtful. Therefore, it can be concluded that the unloading stiffness has an insignificant influence on the numerical response.

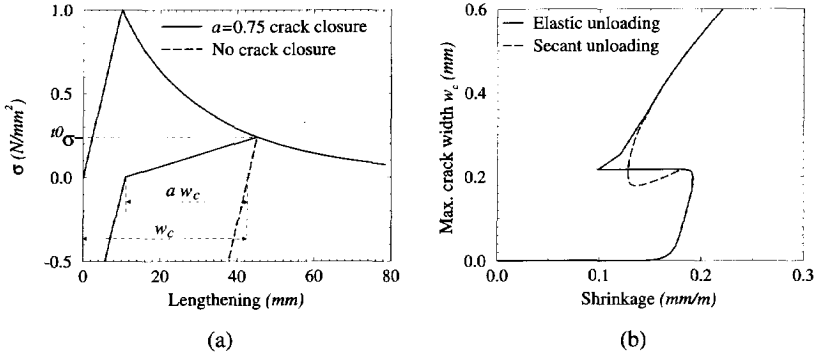


Figure 9.21: (a) Interface elements constitutive behaviour with no (elastic unloading), or partial crack closure upon unloading. (b) Influence of crack closure constitutive behaviour on base-restrained wall shrinkage.

Chapter 10

SUMMARY AND CONCLUSIONS

The main objective of this study, namely to develop an integrated model for the analysis of creep, shrinkage and cracking of masonry, has been addressed by the integration of reasonably accurate constitutive descriptions of these phenomena and formulating robust strategies to solve the resulting governing equations. Although the numerical tool is not intended for design analyses on the platform of consulting engineering, its pragmatic relation between simulation accuracy and computational effort may be exploited by the specialist involved in the derivation of rational design rules.

The moisture migration dominates the time-dependent behaviour of cementitious materials. In this study it is considered at the macroscopic level and is, for computational convenience, expressed in terms of the pore humidity. Thereby, interfaces between materials of different diffusivities can be treated in a natural way. Also, the convective process at the interface with the environment is expressed in terms of the humidity. The drying shrinkage is derived from the pore humidity and in this way forms the one-way coupling between the hygral and mechanical response. Any mechanically enhanced drying is ignored, based on experimental observations in specimens which exhibit no large cracks. This assumption avoids a set of fully coupled hygral and mechanical equations, which usually requires special solution techniques due to the ill-posedness caused by large differences in the "stiffness" coefficients.

The mechanical model is formulated by the serial combination of constitutive descriptions for the shrinkage, creep and cracking, based on the decomposition of the total deformation into these three contributions. In this way the characterisation process is simplified, because each phenomenon can be studied and characterised separately.

Due to the complexity of the microstructure of cementitious materials and the limited knowledge of the micromechanical processes that drive creep, an alternative way to mathematically relating these processes to macroscopically observed creep is chosen. The

short memory visco-elastic behaviour of cementitious materials is exploited for the description of the bulk creep, by employing an aging Maxwell chain formulation. Furthermore, in recognition of the interaction of the shrinkage and creep, which is exhibited most clearly by the increased time-dependent deformation when these processes occur simultaneously, a stress-induced shrinkage is incorporated in the model. Together with cracking, this feature accounts for the Pickett effect.

The limited range of applicability of the proportionality and superposition (up to 50% or 60% of the peak load) inherent to the visco-elastic formulation is compensated for by accounting for the cracking separately. The cracking can be captured with reasonable accuracy by a discrete approach, because the joints are the obvious locations for placing interfaces which, in combination with a multisurface interface material law, have been shown to accurately describe joint debonding and shearing. The addition of a potential vertical crack in the centre of each brick by modelling interfaces there, provides for a limited brick strength and in so doing, supplements the strategy to include the most important crack modes/patterns in masonry. In previous studies a constant dilatancy angle was adopted for the uplift upon shearing along an interface. Here, it has been shown that such a technique may fail. Instead, a new dilatancy softening formulation has been developed, which accounts for the smoothing effect of shear-slipping and confining pressure. It has been verified and validated via micro-shear tests. By this formulation the arbitrary choice of a constant dilatancy angle is circumvented.

Alternatively, the cracking can be modelled in a smeared, continuous way. In this approach, which is a compromise between accuracy and computational effort, the heterogeneity of the masonry is usually ignored. An anisotropic Rankine cracking criterion is suggested by the envelopes formed by the failure loads in biaxial masonry tests at various biaxial force ratios, as well as at various orientations of the orthogonal loads relative to the bed joints. This continuous approach must be regularised to avoid the dependence of the calculated crack pattern on the finite element size and edge orientations. The crack mouth opening viscosity employed in this study introduces a rate term, which regularises the cracking process even for low rates of the shrinkage and creep processes. In addition, the rate term accounts for the observed strength increase with an increased loading rate in this range.

The mechanical part of the model has been verified and validated for notched concrete beams under three-point bending sustained/creep loads. The slow, time-dependent crack growth until and beyond failure is simulated correctly. Although the experiments relate to concrete, it can be seen also as validation for masonry, due to the shared dominating influence in both materials, namely their cementitious nature. To proceed to a next, higher

level of complexity, the hygral model has been activated as well, to validate the model for the case of simultaneous drying. The temptation to analyse masonry experiments of this nature has been overwhelming, despite the fact that they were not designed to distinguish between the various phenomena in a way that enables the objective characterisation of the model parameters. Nevertheless, the numerical results with the preliminary estimated parameters are promising. Furthermore the error in the estimation of the basic creep if the traditional experimental procedures are followed, has been illustrated. The error arises due to the ignorance of the drying creep effect. A proposal for a complete experimental program to characterise masonry creep and shrinkage parameters, as well as to provide validation data, was presented recently (van Zijl 1999b).

Although the current (mechanical) formulation provides for both the drying and thermal shrinkage contributions, the temperature evolution at each material point, from which the thermal shrinkage is derived, is not solved. To enhance the practical relevance of the model, the numerical solution of the thermal conduction process, which is coupled with the moisture diffusion, should be added.

The analyses reported in this study were performed with fixed, prescribed finite element meshes. In pursuing a reduced computational effort without compromising the accuracy of the simulation, an elegant and general method lies in an adaptive remeshing strategy. Such a strategy for masonry may entail an initially coarse, continuous mesh which considers the general brick arrangement. Upon an error/remeshing indication the elements in the indicated areas of potential localisation may be progressively subdivided. Ultimately, the discrete approach may be regained in the critical areas by the placing of interface elements at the joints and in the bricks there. In this way the accuracy of the discrete approach may be exploited, while the computational effort required by a discrete approach on the whole structure is avoided.

REFERENCES

- Alvaredo, A.M. (1994), *Drying Shrinkage and Crack Formation*. Building materials report No 5, ETH Laboratory for building materials, Zürich, Switzerland.
- Alvaredo, A.M., Hebling, A. and Wittmann, F.H. (1995), *Shrinkage data of drying concrete*, Building materials report No 4, ETH Laboratory for building materials, Zürich, Switzerland.
- Backes, H-P (1985), *On the behaviour of masonry under tension in the direction of the bed joints* (in German). Dissertation, Aachen Univ. of Techn., Aachen, Germany.
- Bathe, K-J. (1982), *Finite element procedures in engineering analysis*. Prentice-Hall, Englewood Cliffs, New Jersey, USA.
- Bažant, Z.P. (1988), Material models for structural creep analysis, *Mathematical Modeling of Creep and Shrinkage of Concrete* (ed. Z.P. Bažant), John Wiley and Sons, Ch. 2, 99-215.
- Bažant, Z.P. (1993), Current status and advances in the theory of creep and interaction with fracture, in *Creep and Shrinkage of Concrete* (eds. Z.P. Bažant and I. Carol), E.&F.N.Spon, London, 291-307.
- Bažant, Z.P. and Carol, I. (1993), Eds. of the Proc. of the 5th Int. RILEM Symp. *Creep and Shrinkage of Concrete*. E.&F.N.Spon, London.
- Bažant, Z.P. and Chern, J.C. (1985), Concrete creep at variable humidity, *Mat. and Struct.*, **18**(103), 1-20.
- Bažant, Z.P. and Gettu, R. (1992), Rate effects and load relaxation in static fracture of concrete, *ACI Materials J.*, **89**(5), 456-68.
- Bažant, Z.P. and Kaplan, M.F. (1996), *Concrete at high temperatures. Material properties and mathematical models*, Concrete design and Construction series, Longman, Essex, England.
- Bažant, Z.P. and Najjar, L.J. (1971), Drying of concrete as a nonlinear diffusion problem, *Cement and Concrete Research*, **1**(5), 461-73.

- Bažant, Z.P. and Oh, B.H. (1983), Crack band theory for fracture of concrete, *Mat. and Struct.*, **16**(93), 155-77.
- Bažant, Z.P., Sener, S. and Kim, J-K. (1987), Effect of Cracking on Drying Permeability and Diffusivity of concrete, *ACI Materials Journal*, 351-7.
- Bažant, Z.P. and Xi, Y. (1993), New test method to separate microcracking from drying creep: Curvature creep at equal bending moments and various axial forces, in *Creep and Shrinkage of Concrete* (eds. Z.P. Bažant and I. Carol), E.&F.N.Spon, London, 77-82.
- Bear, J. and Bachmat, Y. (1990), *Introduction to modeling of transport phenomena in porous media*. Volume 4, Kluwer, Dordrecht, The Netherlands.
- Becker, E.B., Carey, G.F. and Oden, J.T. (1981), *Finite Elements: An introduction*. Prentice-Hall, Englewood Cliffs, New Jersey, USA.
- Berkers, W.G.J. and Rademaker, P.D. (1992), *Cracking in long walls* (in Dutch). Report CK015.1, Research Centre for Calcium Silicate Industry, Barneveld, The Netherlands.
- Boltzmann, Z. (1876), Zur Theorie der Elastischen Nachwirkung, *Sitzber Akad. Wiss., Wiener Bericht 70, Wiss. Abh.*, **1**, 279-306.
- Brocken, H.J.P. and Pel, L. (1997), Moisture transport over the brick-mortar interface: water absorption and drying, in *Int. Brick/Block Masonry Conf.* (eds. Mingshun Wu, Yiliang Qian, Xiaozu Su and Xianglin Gu), Shanghai, 826-35.
- Brocken, H.J.P., Pel, L., Smolders, H.R. and Kopinga, K. (1997), Moisture transport in brick masonry: water absorption. Submitted to *Bldg. and Envir.*
- Brooks, J.J. and Hynes, J.P. (1993), Creep and shrinkage of ultra high-strength silica fume concrete, in *Creep and Shrinkage of Concrete* (eds. Z.P. Bažant and I. Carol), E.&F.N.Spon, London, 493-8.
- CEN (1995), *Eurocode 6: Design of masonry structures*. ENV 1996-1-1:1995, CEN, Brussels, Belgium.
- Copeland, R.E. (1957), Shrinkage and temperature stresses in masonry, *ACI Journal*, **53**, 769-80.
- Cornelissen, H.A.W. and Siemes, A.J.M. (1984), *Plain concrete under sustained tensile or tensile and compressive fatigue loadings*. Research on structural concrete 1982-1986, Report 25-87-66, Stevin Laboratory, Delft University of Technology, 1, 68-79.

- Crisfield, M.A. (1981), A fast incremental/iterative procedure that handles snap-through, in *Int. J. Numer. Meth. Eng.*, **7**, 1581-99.
- Crisfield, M.A. (1984), Difficulties with current numerical models for reinforced concrete and some tentative solutions, in *Computer Aided Analysis and Design of Concrete Structures* (eds. F.Damjanić et al.), Pineridge Press, Swansea, U.K., 331-57.
- Dhanasekar, M. Page, A.W. and Kleeman, P.W. (1985), The failure of brick masonry under biaxial stresses, in *Proc. Instn. Civ. Engrs.*, **2**(79), 295-313.
- De Borst, R. and Van den Berg, A.H. (1986), Analysis of creep and cracking in concrete members, in *Creep and Shrinkage of Concrete: Mathematical Modelling* (ed. Z.P. Bažant), 527-38.
- De Borst, R. and Van den Boogaard, A.H. (1993), Finite Element modeling of deformation and cracking in early-age concrete, *J. of Eng. Mech.*, **120**(12), 2519-34.
- De Borst, R., Feenstra, P.H., Pamin, J. and Sluys, L.J. (1994), Some current issues in computational mechanics of concrete, in *Computational Modelling of Concrete Structures* (eds. H.Mang et al.), Pineridge Press, Sansea, UK, 283-302.
- De Borst, R., Sluys, L.J., Van den Boogaard, A.H. and Van den Bogert, P.A.J. (1993), Computational issues in time-dependent deformation and fracture of concrete, in *Creep and Shrinkage of Concrete* (eds. Z.P. Bažant and I. Carol), E.&F.N.Spon, London, 309-26.
- De Jong, P. (1992), Lessons from damage events in the building industry I (in Dutch), *Cement*, **2**, 26-28.
- Domone, P.L.J. (1994), Deformation of concrete, *Construction Materials: Their nature and behaviour* (ed. J.M.Illston), E.&F.N.Spon, London, Ch. 15, 129-54.
- Drysdale, R.G., Hamid, A.A. and Baker, L.R. (1994), *Masonry Structures: Behaviour and Design*. Prentice Hall, Englewood Cliffs, New Jersey.
- Feenstra, P.H. (1993), *Computational aspects of biaxial stress in plain and reinforced concrete*. Dissertation, Delft Univ. of Techn., Delft, The Netherlands.
- Feldman, R.F. and Sereda, P.J. (1970), A new model for hydrated Portland cement paste and its practical implications, *Eng. J.*, **53**(8,9), 53-9.
- Forth, J.P. and Brooks, J.J. (1997), Moisture transfer between mortar and clay brick unit and its effect on long-term deformations of masonry, in *Int. Brick/Block Masonry Conf.* (eds. Mingshun Wu, Yiliang Qian, Xiaozu Su and Xianglin Gu), Shanghai, 672-84.

- Ganz, H.R. and Thürlimann, B. (1982), *Tests on biaxial strength of masonry* (in German). Report 7502-3, Institute of Structural Engineering, ETH Zurich, Zurich, Switzerland.
- Guggisberg, R. and Thürlimann, B. (1987), *Experimental determination of masonry strength parameters* (in German). Report 7502-5, Institute of Structural Engineering, ETH Zurich, Zurich, Switzerland.
- Hageman, J.G. (1968), *Study of shrinkage cracks* (in Dutch). Research Center for Calcium Silicate Industry, Reports no. 189-1-0/189-2-0, The Netherlands.
- Hannant, D.J. (1967), Strain behaviour of concrete up to 95° C under compressive stress, in *Proc. Conf. on Prestressed Concrete Pressure Vessels*, Inst. of Civil Engineers, London, 177-191.
- Houst, Y.F. (1993), Influence of moisture on carbonation shrinkage kinetics of hydrated cement paste, in *Creep and Shrinkage of Concrete* (eds. Z.P. Bažant and I. Carol), E.&F.N.Spon, London, 121-6.
- Ishai, O. (1965), The time-dependent deformation behaviour of cement paste, mortar and concrete, in *Proc. Conf. on Struct. of Concr. and its Behaviour under Load*, Cement and Concrete Association, London, 345-64.
- Koiter, W.T. (1953), Stress-strain relations, uniqueness and variational theorems for elastic-plastic materials with a singular yield surface, *Q. Appl. Math.*, **11**(3), 350-4.
- Kupfer, H.B. and Gerstle, K.H. (1973), Behaviour of concrete under biaxial stresses, *J. Engrg. Mech.*, ASCE, **99**(4), 853-66.
- Lenczner, D. (1981), *Movements in buildings*. Pergamon Press, Oxford, England.
- Le Roy, R. and De Larrard, F. (1993), Creep and shrinkage of high-performance concrete: The LCPC experience, in *Creep and Shrinkage of Concrete* (eds. Z.P. Bažant and I. Carol), E.&F.N.Spon, London, 499-504.
- L'Hermite, R., Chefdeville, J. and Grieu, J.J. (1949), Nouvelle contribution à l'étude du retrait des ciments (in French), *Annales ITBTP*, 309-310, 30-4.
- L'Hermite, R. and Mamillan, M. (1968), Retrait et fluage des bétons (in French), *Annales ATBTP*, **21**(249), 1319-37.
- L'Hermite, R. and Mamillan, M. (1973), Repartition de la teneur en eau dans le béton durci (in French), *Annales ITBTP*, 309-10, 30-4.
- Lourenço, P.B. (1996), *Computational strategies for masonry structures*. Dissertation, Delft Univ. of Techn., Delft, The Netherlands.

- Lurati, F., Graf, H. and Thürlimann, B. (1990), *Experimental determination of the strength parameters of concrete masonry* (in German). Report 8401-2, Institute of Structural Engineering, ETH Zurich, Zurich, Switzerland.
- Neville, A.M. (1959), Tests on the influence of the properties of cement on the creep of mortar, *Rilem Bul.*, 4, 5-17.
- Neville, A.M. (1991), *Properties of concrete*. Longman Scientific & Technical, New York, USA.
- Page, A.W. (1978), Finite element model for masonry, *J. Struct. Div.*, ASCE, **104**(8), 1267-85.
- Page, A.W. (1981), The biaxial compressive strength of brick masonry, in *Proc. Intsn. Civ. Eng.*, **2**(71), 893-906.
- Page, A.W. (1983), The strength of brick masonry under biaxial compression-tension, *Int. J. Masonry Constr.*, **3**(1), 26-31.
- Parrot, L.J. and Young, J.F. (1982), Shrinkage and swelling of two hydrated alite pastes, in *Fundamental Research on Creep and Shrinkage of Concrete* (ed F.H. Wittmann), Marthinus Nijhoff Publishers, The Hague, The Netherlands, 35-48.
- Pel, L. (1995), *Moisture transport in porous building materials*. Dissertation, Eindhoven Univ. of Techn., Eindhoven, The Netherlands.
- Philip, J.R. and De Vries, D.A. (1957), Moisture movement in porous materials under temperature gradients, *Trans. Am. Geophys. Un.*, **38**(2), 222-32.
- Pickett, G. (1942), The effect of change in moisture content on the creep of concrete under a sustained load, *J. of the ACI*, **38**, 333-55.
- Pickett, G. (1946), Shrinkage stresses in concrete, *J. of the ACI*, **42**, 165-195.
- Powers, T.C. (1959), Causes and control of volume change, *J. PCA Res. and Development Lab.*, **1**, 29-39.
- Ramm, E. (1981), Strategies for tracing the nonlinear response near limit points, in *Non-linear finite element analysis in structural mechanics* (eds. W. Wunderlich, E. Stein and K.-J. Bathe), Springer-Verlag, Berlin, 63-89.
- Riks, E. (1972), The application of Newton's method to the problem of elastic stability, *J. Appl. Mech.*, **39**, 1060-5.
- Rots, J.G. (1988), *Computational modelling of concrete fracture*. Dissertation, Delft Univ. of Techn., Delft, The Netherlands.

- Rots, J.G. (1994), *Structural masonry: an experimental/numerical basis for practical design rules* (in Dutch, see Rots 1997 for English translation), CUR report 171, Ch. 6, 139-66.
- Rots, J.G. (1996), *Inventory of research aspects for structural masonry: Cracking and stability* (in Dutch). Report 96-NM-R1513, TNO Building and Construction, Delft, The Netherlands.
- Rots, J.G. (1997), *Structural masonry; an experimental/numerical basis for practical design rules*. Balkema, Rotterdam, The Netherlands.
- Rüsch, H. (1960), Researches toward a general flexural theory for structural concrete, *ACI J.*, **57**(1), 1-28.
- Sabri, S. and Illston, J.M. (1982), Isothermal drying shrinkage and wetting swelling of hardened cement paste, in *Fundamental Research on Creep and Shrinkage of Concrete* (ed F.H. Wittmann), Marthinus Nijhoff Publishers, The Hague, The Netherlands, 63-72.
- Sayed-Ahmed, E.Y., Shrive, N.G. and Tilleman, D. (1998), Creep deformation of clay masonry structures: a parametric study. *Canadian J. Civil Eng.*, **25**(1), 67-80.
- Schubert, P. (1982), *Hygral movements of masonry walls* (in German). Dissertation, Techn. Univ. of Aachen, Aachen, Germany.
- Schubert, P. (1988), About the crack-free length of non-loadbearing masonry walls (in German), *Mauerwerk-Kalendar*, 473-88.
- Shrive, N.G., Sayed-Ahmed, E.Y. and Tilleman, D. (1997), Creep analysis of clay masonry assemblages, *Canadian J. of Civil Eng.*, **24**(3), 367-79.
- Simo, J.C. and Taylor, R.L. (1985), Consistent tangent operators for rate-independent elastoplasticity, *Comp. Meth. Appl. Mech. Eng.*, **48**, 101-18.
- Sluys, L.J. (1992), *Wave propagation, localisation and dispersion in softening solids*. Dissertation, Delft Univ. of Techn., Delft, The Netherlands.
- Soroka, I. (1979), *Portland Cement Paste and Concrete*. Macmillan, London.
- Tammes, E. and Vos, B.H. (1984), *Heat and moisture transport in building structures* (in Dutch). Kluwer, Deventer-Antwerpen.
- Tazawa, E. and Miyazawa, S. (1993), Autogeneous shrinkage of concrete and its importance in concrete technology, in *Creep and Shrinkage of Concrete* (eds. Z.P. Bažant and I. Carol), E.&F.N.Spon, London, 159-68.
- Troxell, G.E., Raphael, J.M. and Davis, R.E. (1958), Long-time creep and shrinkage tests of plain and reinforced concrete, in *Proc. ASTM.*, **58**, 1101-20.

- Van den Boogaard, A.H., De Borst, R. and Van den Bogert, P.A.J. (1994), An adaptive time-stepping algorithm for quasistatic processes, *Comm. in Num. Meth. in Eng.*, **10**, 837-44.
- Van der Pluijm, R. (1992), *Deformation controlled shear tests on masonry* (in Dutch). Report BI-92-104, TNO Building and Construction, Delft, The Netherlands.
- Van der Pluijm, R. (1998), *Overview of deformation controlled combined tensile and shear tests*. Report TUE/CCO/98.20, Eindhoven Univ. of Techn., Eindhoven, The Netherlands.
- Van der Pluijm, R. and Vermeltoort, A.Th. (1991), *Deformation controlled tension and compression tests on units, mortar and masonry* (in Dutch). Report B-91-0561, TNO Building and Construction, Delft, The Netherlands.
- Van der Pluijm, R. and Wubs, A.J. (1996), *The time dependent deformational behaviour of masonry* (in Dutch). Report 96-CON-R0901-02, TNO Building and Construction, Delft, The Netherlands.
- Van der Veen, H. (1998), *The significance and use of eigenvalues and eigenvectors in the numerical analysis of elasto-plastic soils*. Dissertation, Delft Univ. of Techn., Delft, The Netherlands.
- Van Zijl, G.P.A.G. (1996), *Masonry micro-shear behaviour along bed joints*. Report 03-21-22-0-01, Delft Univ. of Techn., Delft, The Netherlands.
- Van Zijl, G.P.A.G. (1999a), *A numerical formulation for masonry creep, shrinkage and cracking*. Series 11 Eng. Mech. 01, Delft Univ. Press, Delft, The Netherlands.
- Van Zijl, G.P.A.G. (1999b), *A numerical formulation for moisture migration in masonry*. Series 11 Eng. Mech. 02, Delft Univ. Press, Delft, The Netherlands.
- Van Zijl, G.P.A.G., Lourenço, P.B. and Rots, J.G. (1997), Non-associated plasticity formulation for masonry interface behaviour, in *Computational Plasticity: Fundamentals and Applications* (eds. D.R.J. Owen, E. Oñate and E. Hinton), Barcelona, 1586-93.
- Verbeek, G.J. and Helmuth, R.A. (1968), Structures and physical properties of cement past, in *Proc. 5th Int. Symp. Chemistry of Cem.*, **3**, 1-36.
- Vermeltoort, A.Th. and Raijmakers, T.M.J. (1993), *Deformation controlled tests of masonry shear walls* (in Dutch). Report TUEBKO93.08, Eindhoven Univ. of Techn., Eindhoven, The Netherlands.
- Wang, Weimin (1997), *Stationary and propagative instabilities in metals - a computational point of view*. Dissertation, Delft Univ. of Techn., Delft, The Netherlands.

- Warren, D. and Lenczner, D. (1981), A creep-time function for single-leaf brickwork walls, *Int. J. of Masonry Constr.*, **2**(1), 13-19.
- Whitaker, S. (1977), Simultaneous heat, mass and momentum transfer in porous media. *Adv. Heat Transfer*, **13**, 119-200.
- Wittmann, F.H. (1968), Surface tension, shrinkage and strength of cement paste, *Mater. Struct.*, **1**(6), 547-552.
- Wittmann, F.H. (1977), Grundlagen eines Modells zur Beschreibung charakteristischer Eigenschaften des Betons (in German), *Schriftenreihe Deutscher Ausschuss für Stahlbeton*, Heft 290, Berlin, 43-101.
- Wittmann, F.H. (1980), Trends in research on creep and shrinkage of concrete, *Cement Production and Use* (ed. J. Skalny), Engineering Foundation, New York, USA, 143-61.
- Wittmann, F.H. (1982), Ed. of the Proc. of the Conf. *Fundamental research on creep and shrinkage of concrete*. Marthinus Nijhoff Publ., The Hague, The Netherlands.
- Wu, Z.S. and Bažant, Z.P. (1993), Finite element modelling of rate effect in concrete fracture with influence of creep, in *Creep and Shrinkage of Concrete* (eds. Z.P. Bažant and I. Carol), E.&F.N.Spon, London, 427-32.
- Young, J.F. (1988), Physical mechanisms and their mathematical descriptions, *Mathematical Modeling of Creep and Shrinkage of Concrete* (ed. Z.P. Bažant), John Wiley and Sons, Ch. 1, 63-98.
- Zhou, F.P. (1992), *Time-dependent Crack Growth and Fracture in Concrete*. Dissertation, Lund Univ., Lund, Sweden.
- Zienkiewicz, O.C. (1986), *The Finite Element Method*. McGraw-Hill, Berkshire, England.

SUMMARY

COMPUTATIONAL MODELLING OF MASONRY CREEP AND SHRINKAGE
G.P.A.G. van Zijl

To fully exploit the fundamental descriptions of the mechanisms of moisture transport, shrinkage, creep and cracking of cementitious materials, their formulation into integrated computational models for application in practical structural engineering problems is imperative. This is the main focus of this dissertation.

Masonry is the cementitious material of particular interest in this study. The main features, trends and dependencies of masonry creep and shrinkage are presented in Chapter 2. Because the level of characterisation of masonry lags behind concrete, borrowing from the concrete world is inevitable, but justified to a large extent by the cementitious nature these materials have in common.

The mathematical modelling of these phenomena follows in Chapter 3. For practical relevance it is considered at the macroscopic level. The moisture migration dominates the creep and shrinkage behaviour and its description forms the starting point. It is modelled as a diffusive process in terms of the pore humidity. Subsequently, the mechanical behaviour is formulated in terms of time-dependent stresses and strains. The shrinkage is derived from the pore humidity, while the creep is formulated as aging visco-elasticity. In recognition of the interaction of the shrinkage and creep, which is exhibited most clearly by the increased time-dependent deformation when these processes occur simultaneously, a stress-induced shrinkage is incorporated in the model. The cracking is formulated in the framework of plasticity, including a cracking rate contribution, which regularises the continuum description of localisation and captures the rate-dependent strength enhancement.

For the analysis of practical problems a numerical solution of the mathematical formulation is necessary. A finite element solution to the governing set of differential equations is elaborated in Chapter 4.

Chapter 5 describes the particular cracking criteria, which depend on the crack modelling strategy. The predictability of the crack locations in masonry is exploited in a discrete

approach to model the cracks. For this case interface elements discretise the masonry joints. An interface material model is employed, which combines a tension cut-off and a non-associative Coulomb-friction criterion. The same material law may be used to capture brick cracking in a simple way. Alternatively, the cracks are described in a continuous way, in which case an anisotropic Rankine criterion is employed.

Chapters 6 and 7 are devoted to the verification and validation of the model. First the mechanical model alone is activated and its ability illustrated to simulate the interaction between the creep and fracture in three-point-bending experiments. An important conclusion of this chapter is the significant role of the cracking rate dependence even at the normal, quasi-static loading rates employed in these experiments. Subsequently, in Chapter 7, masonry drying and creep experiments are analysed to validate the combined hygral and mechanical model. Due to the lack of measurement data for the characterisation of all the model parameters, a full validation has not been possible, but the preliminary results are promising. An experimental program has been proposed to produce the required characterisation and validation data.

In Chapter 8 the model is employed in the structural analysis of masonry walls to illustrate its robustness in capturing the crack initiation and growth to a fully developed crack pattern. Particular attention is given to the objectivity of the pattern of primary and secondary cracks. The role of the cracking rate dependence is shown in this regard. In Chapter 9 a step is made towards deriving practical design rules from numerical results calculated with the model. The particularly lean design aspect of the spacing of movement joints in masonry walls, which control cracking due to differential thermal and hygral movement, is taken as an illustrative example. A simplified modelling strategy is described and verified numerically with reference analyses, to make the repetitive analysis of such large masonry walls viable.

The major conclusion of this thesis is that it is possible to bridge the gap between the fundamental research front of the creep, shrinkage and cracking of cementitious materials and the application of the knowledge to overcome practical problems in structures. With the benefit of the numerical tool presented, an analyst can both qualitatively and quantitatively study structural behaviour, which is otherwise too complex or of too a large scale. Alternatively, particular aspects of structural behaviour can be analysed in an intermediate step in the formulation of rational design rules.

SAMENVATTING

NUMERIEKE MODELLERING VAN KRUIP EN KRIMP VAN METSELWERK
G.P.A.G. van Zijl

Om de fundamentele beschrijvingen van de mechanismen van vochttransport, krimp, kruip en scheurvorming van cement-gebonden materialen volledig te kunnen exploiteren, dienen ze geformuleerd te worden in geïntegreerde numerieke modellen ten behoeve van toepassing op problemen uit de constructieve ingenieurspraktijk. Dit is het hoofdonderwerp van deze dissertatie.

Metselwerk is het cement-gebonden materiaal waarop deze studie zich richt. De belangrijkste fenomenen, trends en relaties van kruip en krimp in metselwerk worden gepresenteerd in hoofdstuk 2. Aangezien het niveau van karakterisering van metselwerk achterloopt bij dat van beton, is het onvermijdelijk dat geleend wordt van de betonwereld. Dit is echter gerechtvaardigd gezien de grote mate van overeenkomst in het cement-gebonden karakter van deze materialen.

De wiskundige formulering van deze fenomenen volgt in hoofdstuk 3. Deze wordt beschouwd op macro-niveau wegens relevantie voor problemen uit de praktijk. De vochttransport domineert het kruip- en krimpgedrag en de beschrijving ervan vormt het startpunt. Zij wordt gemodelleerd als een diffusief proces in termen van de porievochtigheid. Vervolgens wordt het mechanisch gedrag geformuleerd in termen van tijdsafhankelijke spanningen en rekken. De krimp wordt afgeleid van de porievochtigheid, terwijl de kruip wordt geformuleerd als verouderingsviscoelasticiteit. De interactie tussen krimp en kruip, welke het meest duidelijk naar voren komt in de toegenomen tijdsafhankelijke vervorming bij gelijktijdig optreden van deze processen, is verdisconteerd in het model middels spanningsgestuurde krimp. Scheurvorming is geformuleerd in het raamwerk van plasticiteit, inclusief een bijdrage van de scheursnelheid, welke de continuumbeschrijving van localisatie regulariseert en de snelheidsafhankelijke toename van sterkte ondervangt.

Voor de analyse van problemen uit de praktijk is de numerieke oplossing van de wiskundige formulering noodzakelijk. Een eindige-elementenoplossing van de geldende set differentiaalvergelijkingen wordt uitgewerkt in hoofdstuk 4. Hoofdstuk 5 beschrijft de specifieke scheurcriteria, die afhangen van de wijze waarop de scheur gemodelleerd is.

De voorspelbaarheid van de scheurlocaties in metselwerk wordt gebruikt in een discrete scheurmodellering. Voor dit geval zijn de voegen gediscretiseerd door interface-elementen. Een interface-materiaalmodel is gebruikt dat een 'tension cut-off' combineert met een niet-associatief Coulombs wrijvingscriterium. Dezelfde materiaalwet zou gebruikt kunnen worden om scheurvorming in de baksteen op eenvoudige wijze te kunnen beschrijven. Anderzijds kunnen de scheuren als continue worden beschreven, waarbij een anisotroop Rankine-criterium is gebruikt.

Hoofdstuk 6 en 7 zijn gewijd aan de verificatie en de validatie van het model. In de eerste plaats is alleen het mechanische model gebruikt, waarvan het vermogen is geïllustreerd om de interactie tussen kruip en breuk te simuleren in driepuntsbuigproeven. Een belangrijke conclusie van dit hoofdstuk vormt de significante rol van de scheursnelheidsafhankelijkheid, zelfs bij de normale, quasi-statische belastingsnelheden die bij deze experimenten toegepast worden. Vervolgens worden in hoofdstuk 7 het uitdrogen van metselwerk en kruipproeven geanalyseerd om het gecombineerde hygrisch-mechanische model te valideren. Wegens een gebrek aan meetgegevens voor de karakterisering van alle modelparameters was een volledige validatie niet mogelijk. De voorlopige resultaten zijn echter veelbelovend. Een experimentenprogramma is voorgesteld om de data voor de gewenste karakterisering and validatie te genereren.

In hoofdstuk 8 is het model gebruikt in de constructie-analyse van metselwerkmuren om zijn robuustheid te illustreren in het beschrijven van scheurinitiatie en -groei tot een volledig ontwikkeld scheurpatroon. Speciale aandacht gaat uit naar de objectiviteit van het patroon van primaire en secundaire scheuren. De rol van de scheursnelheidsafhankelijkheid wordt in deze context aangetoond. In hoofdstuk 9 wordt een aanzet gegeven tot het afleiden van rekenregels voor praktijkontwerpen. In het bijzonder worden de ontwerpaspecten van de plaatsing van dilatatievoegen in metselwerkmuren beschouwd, welke scheurvorming sturen als gevolg van verschillen in thermische en hygrische uitzetting. Een versimpelde modelleringsstrategie wordt beschreven en numeriek geverifieerd aan de hand van referentieanalyses, zodat de herhaaldelijke analyse van dergelijke grote metselwerkmuren haalbaar wordt.

De hoofdconclusie van deze dissertatie is dat het mogelijk is de kloof te overbruggen die bestaat tussen enerzijds fundamenteel frontonderzoek op het gebied van kruip, krimp en scheurvorming van cement-gebonden materialen en anderzijds toepassing van deze kennis om praktijkproblemen met constructies te voorkomen. Met de beschikking over het voorgestelde model kan de analyst zowel kwalitatief als kwantitatief constructiegedrag bestuderen dat anders te complex of te grootschalig zou zijn. Verder kunnen specifieke aspecten van het constructiegedrag geanalyseerd worden om rationele ontwerpregels te formuleren.

CURRICULUM VITAE

- 10 September 1961: Born in Port Elizabeth, South Africa.
- July 1980-June 1982: National service, Special Guard Unit, Grote Schuur, Cape Town, South Africa.
- Jan. 1983-Dec. 1986: Bachelors degree in Civil Engineering, University of Stellenbosch, South Africa.
- Jan. 1987-Jul. 1989: Researcher, Institute for Structural Engineering, University of Stellenbosch, South Africa.
- Aug. 1989-Sept. 1992: Engineer and Project leader, Bureau for Mechanical Engineering, Stellenbosch University, South Africa.
- March 1987-Dec. 1990: Masters degree in Civil Engineering, University of Stellenbosch, South Africa.
- Oct. 1992-Sept. 1995: Lecturer, Department of Civil Engineering, University of Stellenbosch, South Africa.
- Oct. 1995-Dec. 1998: Research Assistant, Faculty of Civil Engineering, Delft University of Technology.
- Jan. 1999-Sept. 1999: Research Assistant, Faculty of Aerospace Engineering, Delft University of Technology.
- Since Oct. 1999: Researcher, Faculty of Architecture, Delft University of Technology.

